Doctoral Dissertation

Processing and Strengthening Mechanisms of Aluminum Metal Matrix Composites Reinforced with Carbon Nanotubes

BIAO CHEN

January 2016

Graduate School of Engineering,
Osaka University

Table of Contents

Chapter 1
Introduction

1.1 Properties and applications of aluminum and its alloys

Aluminum (Al) is a silvery-white colored metal. It is the third most abundant element (after oxygen and silicon), and the most abundant metal in the Earth's crust (~8%). Compared with other metal materials, Al has unique physical properties [1, 2], some of which are typically shown in **Table 1-1**. Al has a relatively low density of 2.7 g cm^{-3} compared to other metals, only about one third of copper or steel. It makes Al one of the best candidates for components used in light weight applications. The melting point (T_m) of Al is 660 ℃, similar to magnesium (Mg, 650 ℃) and comparably low compared with other metals, such as titanium (Ti, 1668 ℃). Low melting point and good ductility contribute to outstanding formability and machinability of Al materials [3]. When exposed to air, Al directly forms an oxide layer with a thickness of ~1 to ~10 nm on the surface which acts as a protective shield from further oxidation. This dense passivation layer also contributes to the excellent anti-corrosive properties of Al and its alloys [4]. Moreover, Al possesses sound conductive properties (rank fourth highest among metals), nonmagnetic property, nearly nontoxicity and high reflectivity to waves and so on [2].

Table 1-1. Typical physical properties of Al at room temperature [1].

Physical property	Value or type
Atomic number	13
Phase structure	Face centered cubic (FCC)
Density (g cm^{-3})	2.70
Melting/boiling point (℃)	660/2470
Thermal conductivity (W m^{-1} K^{-1})	237
Electrical resistivity (nΩ·m)	28.2
Young's/shear modulus (GPa)	70/26

Since the Hall–Héroult electrolysis process [5] was discovered to produce commercial pure Al in 1886, the production and consumption of Al grow rapidly. Today, Al has been the most widely used metal in the world after iron. Considering the advantages of

Al, structural components made from Al and its alloys are vital to the aerospace [6, 7] and automobile industry [8] and are important in other areas of transportation, construction, power, metallurgy engineering and so on [1]. However, using Al in its pure form is not applicable due to many factors of which the most important is its relatively low stiffness and low strength. That's why different strengthening approaches have been developed to enhance mechanical properties while keeping most of the desired properties of the base Al presented in the new materials.

1.2 Strengthening approaches of pure Al

Similar to other metal materials, the improvement of mechanical properties of pure Al can be achieved by various effective approaches, viz., adding alloying elements, using grain refining, work hardening and dispersing second phases into Al matrix.

1.2.1 Alloying elements

The addition of some substitutional solid solution elements to Al matrix forms Al alloys [1]. The typical alloying elements in Al are copper (Cu), manganese (Mn), silicon (Si), Mg, and zinc (Zr), producing 2xxx, 3xxx, 4xxx, 5xxx, and 7xxx series alloys with corresponding specific element content, respectively. In these categories, there is only one dominant alloy element and the content of other elements are below specific values. Exceptionally, 1xxx series Al alloys refer to commercial pure Al with Al content larger than 99 wt.% and 6xxx series have two dominant alloy elements of Mg and Si. 8xxx series are alloyed with other elements which are not covered in the aforementioned seven kinds. Al-lithium (Li) alloy is a typical 8xxx series alloy which is widely used [9].

There are two categories of Al alloys, non-heat-treatable and heat-treatable alloys. With non-heat-treatable alloys, the additive alloying elements only solute in Al matrix. The tensile strength and hardness are improved with sacrificed ductility compared with Al matrix. However, Young's modulus is hard to be noticeably improved, showing similar values to pure Al. With heat-treatable alloys, such as 2024 alloy, precipitation is able to be achieved after aging and thus secondary phases are produced in Al matrix [10]. Therefore, there are two modes by which alloying elements strengthen aluminum: solid solution strengthening

and precipitation strengthening. In solid solution strengthening, the added alloying elements mix with the aluminum at the atomic level. The extent of strengthening depends on the type and amount of added elements. With precipitation strengthening the added alloying elements can be controlled to react with Al to form fine particles in size of micrometers or nanometers in the matrix. These particles are referred to as precipitates. The process where the precipitates are formed, called aging, is normally carried out at elevated temperatures, typically 160-190℃ [1]. In some cases, aging can occur at ambient temperature in which case it is called natural aging [11]. Examples of products that are precipitation strengthened are aircraft components like fuselage and wings, automotive products like transmission cases and engine hoods, furniture, hardware, pipe, and wheels [6, 8].

The above alloys are based on displacement solid solution mechanism, due to the small atom radius of Al and resultant small size of inter-atom space. Interstitial solid solubility, even for the smallest hydrogen atoms, are extremely small in solid Al matrix [12].

1.2.2 Work hardening

Work hardening (also called strain-hardening or cold-working) is the process of making a metal harder and stronger through plastic deformation. When a metal is plastically deformed, dislocations move and additional dislocations are generated. The more dislocations within a material, the more they will interact and become pinned or tangled. This will result in a decrease in the mobility of the dislocations and a strengthening of the material. This type of strengthening is the commonly called cold-working. When a metal is worked at higher temperatures (hot-working) the dislocations can rearrange and little strengthening is achieved. It should be understood, however, that increasing the strength by cold-working will also result in a reduction in ductility. Usually a small amount of cold-working results in a significant reduction in ductility.

Considering whether plastic deformation is applied during processing, with the eight series alloys, there is another principal of classification, namely cast alloys and wrought alloys. Cast alloys are directly cast into their final form by one of various methods such as sand-casting, die or pressure die casting. Casting is used for complex product shapes. These alloys usually contain high levels of silicon to improve their castability. Wrought alloys, which are initially consolidated as ingots or billets and subsequently hot and/or cold worked

mechanically into the desired form. About 85% of Al and Al alloys are used for wrought products, for example rolled or forged plate, foils and extrusions. Wrought Al alloys generally have higher melting point and higher tensile strength, although they are usually more expensive than cast alloys. Combination of work-hardening and aging is a creative method to obtain some novel Al materials having both high strength and ductility [10, 13].

1.2.3 Grain refinement

Grain refinement is another significant method to improve the strength of polycrystalline metals. For example, heat treatment after plastic deformation and changing the rate of solidification are typical ways to alter the grain size. The increases of grain boundary are important factors as obstacles to the slip of metals. The finer grains, which have more grain boundaries, are stronger than the coarser grains because a higher applied stress is required for slipping. Moreover, the accumulation of dislocations in the finer grains is much higher than coarser grains, so that the required stress to move these dislocations across the grain boundary thus increases with increasing the grain boundaries [14]. As a typical face centered cubic (FCC) metal, Al has diverse slip systems (exactly 12 series), so it is ductile and easily plastically deformed for generating grain refinement. In the past decades, Al materials with nano-sized grains have been investigated intensively [15-18].

1.2.4 Composite strengthening

Al matrix materials reinforced with one or more reinforcements are called Al matrix composites (AMCs), which are young promising materials. Considering the formation place of reinforcements, composites are divided to *ex-situ* and *in-situ*. In *ex-situ* composites, reinforcements are synthesized externally and then added into the matrix during composite fabrication. While, *in-situ* reinforcements are not directly added but synthesized internally in the matrix during processing. Actually, the aforementioned precipitation-strengthened Al alloy is a kind of *in-situ* AMCs.

The dispersed secondary phases in ductile Al behave as obstacles to dislocation motion. The dislocation can bow out or cut through the reinforcements which is related to their strength and coherency between the lattices of reinforcement and matrix [19]. Hard ceramic reinforcements may also bear load during composite failure. It lead to load transfer

from matrix to reinforcements and mechanical improvement of composites [19]. More importantly, as a mixture of different phases, AMCs now not only present the nature of matrix Al but also acquire some properties from the reinforcements. This characteristic bring wide design scope of material structure for achieving superior properties than pure Al.

Various types of reinforcement phases are added with the aim of achieving specific improved properties, for example strength, stiffness, toughness, thermal conductivity, electrical conductivity, coefficient of thermal expansion, electromagnetic shielding, damping and wear resistance. The reinforcing effect is greatly dependent on the characteristics of reinforcements, such as strength, content, size, and morphology. Considering the morphology, particulate and fibrous reinforcements are two most significant categories in AMCs.

1.2.4.1 Particulate reinforcements

Conventional AMCs reinforced with hard particulates exhibit high strength and high elastic modulus, near-isotropic as well as excellent high-temperature creep resistant properties [16, 20-22]. These materials are of special interest because of their ease of fabrication at relatively low cost. Particulate-reinforced AMCs have been used as structural materials in the aerospace, automotive and railway sectors. SiC particulate-reinforced AMCs are attractive materials for the ventral fins and fuel access door covers in the US F-16 aircraft [23]. However, the size range of ceramic particulates of Al-based metal matrix composites (MMCs) is very large, typically from nanometers to several hundreds of micrometers.

Large ceramic particulates are prone to cracking during mechanical loading, leading to premature failure and low composite ductility [24]. Particulate size has a strong effect on the failure mode, strength, and ductility of the Al-based composites [24, 25]. With development of nanotechnology, growing attentions are paid on nano-sized particle reinforcements such as oxides [20], carbides [26, 27], nitrides [28], borides [29], metal glass [30] and carbon [31, 32] in Al matrix. Usually, the nanoparticles are mixed with Al powder and consolidated by the powder metallurgy process for fabricating advanced AMCs. Some review articles [16, 21, 22, 33-36] can be found in this area.

1.2.4.2 Fibrous reinforcements

Compared with particulate reinforcements, the most significant advantage of fibrous reinforcements is their large aspect ratios (length to diameter ratio), which are critical to achieve high load-bearing ability and resultant high composite strength. According to the shear-lag theories set up by Cox [37], Kelly and Tyson [38] et al., load transfer happens from matrix to reinforcements through an interfacial stress in composites. Stress distribution on reinforcement is dependent on its length or aspect ratio. If the length is large enough to a critical value, the maximum stress on fiber can reach its breaking strength. The strength of fiber reinforced composites are related to the aspect ratio, volume content, strength of reinforcement. Therefore, long and strong fibrous reinforcements are most promising in strengthening Al matrix.

Up to date, various fibrous reinforcements [39], such as boron fiber [40], SiC whisker [41], glass fiber [42], carbon fiber [43], boron nitride (BN) nanotube [44], and carbon nanotube [45], have been applied in AMCs. Their structural and mechanical properties and synthesis methods are summarized in **Table 1-2** [19]. Among them, carbon nanotubes having super-high strength (up to ~100 GPa), super-high modulus (~1 TPa) and large aspect ratios (50-1000) are most promising reinforcements in AMCs.

Table 1-2. Tensile properties and density of various fibrous reinforcements [19].

Fibers	Tensile modulus (GPa)	Tensile strength (GPa)	Density (g cm^{-3})
Boron	415	3.5	2.5-2.6
SiC	300-400	2.8	2.8
E-Glass	71	1.8-3.0	2.5
Carbon (P100)	725	2.2	2.15
Aramid	125	3.5	1.45
BN [46]	926	30	2.2
CNT [47]	~900	150	~2

1.2.5 Strengthening effect of various approaches

The strengthening effect of the aforementioned approaches on strength, ductility, modulus and obeyed theory are summarized in **Table 1-3**. Although high strength AMCs can be achieved through each strengthening methods, the ease and cost of the corresponding processes are different. Moreover, it is seen that one unique advantage of composite strengthening is that the modulus can be enhanced at the same time. With the fast development of nanotechnology, composites strengthening in AMCs was spurred by the

novel reinforcements, such as CNT and graphene, to fabricate high-performance AMCs with superior properties.

Table 1-3. Effect of various strengthening approaches on mechanical properties.

Strengthening method		Strength	Ductility	Modulus	Strengthening model	Example
Alloys elements		Significant	Significant	Small	Eshelby [48]	5083 alloy
Grain refinement		Medium	Medium	No	Hall-Petch [49]	UFG Al
Work hardening		Medium	Significant	No	Taylor [50]	6262-T9
Composite	Particles	Significant	Significant	Significant	Orowan-Ashby [51]	SiC_p/Al
	Fibers	Significant	Significant	Significant	Kelly-Tyson [38]	C_f/Al

1.3 Carbon nanotube reinforced composites

In 1991, Iijima reported landmark findings on the 'helical microtubules of graphitic carbon' which was later named as CNTs [52]. Now it is known that CNTs can exist as single tube which is called single-walled nanotube (SWCNT) [53] or in the form of concentric tubes called multi-walled nanotube (MWCNT) [52], as shown in **Figure 1-1**. CNTs have many amazing properties compared with traditional materials and they caught great attention in materials science and technology [54-60].

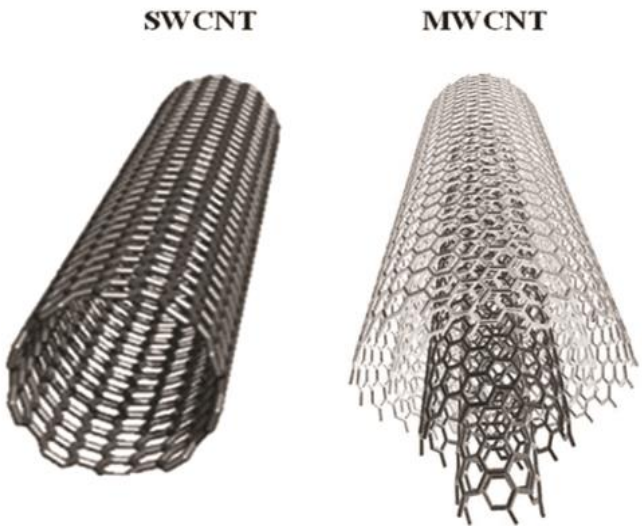

Figure 1-1. Structure schematic of SWCNT and MWCNT [62].

Table 1-4 shows the physical properties of SWCNT, MWCNT as well as traditional steel [57-59, 61-64]. It is seen that CNTs have about 100 times tensile strength of steel.

Moreover, they have high Young's modulus of approximately 1 TPa and a low density of 1-2 g cm^{-3}, which make them preferable reinforcements for strong and light composites materials.

Table 1-4. Typical physical properties of SWCNT and MWCNT at room temperature, compared with traditional steel.

Physical property	SWCNT	MWCNT	Steel
Density (g cm^{-3})	~1	1.4-2.1	7.8
Melting point (℃)	3550	3550	1538
Thermal conductivity (W $m^{-1}K^{-1}$)	~3500	~3000	80
Electrical resistivity (nΩ·m)	10	10	100
Tensile strength (GPa)	13-53	11-150	0.4-1.5
Elongation to break (%)	16	~10	15-50
Young's modulus (TPa)	~1	~1	0.2

The beginning of widespread CNT research was in the early 1990s. However, CNT-related commercial activity has grown most substantially during the past decade. Since 2006, worldwide CNT production capacity has increased at least 10-fold in 2013, and the annual number of CNT-related journal publications and issued patents continues to grow [59]. Today most CNT production is used in bulk composite materials and thin films. Initially, CNTs were widely used for reinforcing polymers due to the relative ease of processing [65-70]. CNTs found success in polymers because of their exceptional reinforcing effects [70], although there still seem large room to fulfil the potential of CNTs by overcoming some key problems such as dispersion of CNTs in polymers [68].

1.4 Processing of carbon nanotube/Al composites

The interest in using CNTs as a reinforcing phase in MMCs is spurred by the successful incorporation of nanotubes into polymers to form high performance composites. MMCs reinforced with CNTs offer several distinct advantages over polymeric counterparts such as inherent stability at elevated temperature, high strength and stiffness, superior electrical and thermal conductivity deriving from the metal matrix [58]. However, it is rather difficult to introduce CNTs into metals because they tend to agglomerate into clusters within the matrix. Another issue arises from the poor wetting of CNTs by molten metals owing to a large difference in the surface tensions of carbon nanotubes and metals [71, 72]. It results in

poor bonding conditions at the interface between CNTs and Al, which is unfavorable to obtain high load transfer efficiency from matrix to CNTs.

Kuzumaki et al. were the first researchers to fabricate CNT/Al composites using conventional powder mixing, followed by hot pressing and hot extrusion processes [45]. They found that the tensile strength of 5 and 10 vol.% CNT/Al composites is almost identical to that of unreinforced Al owing to the poor dispersion of nanotubes. The only benefit is that the tensile properties of CNT/Al are much more stable than pure Al during the post annealing treatment to 100 h. From 1998 to now, some approaches [56, 58, 73] were developed to deal with the dispersion problem in Al matrix. Moreover, many consolidation processes, such as casting [74, 75], spraying [76, 77], rolling [78-80], forging [81-83], sintering [84], extrusion [85-87] and their combinations [88-92], were also applied to fabricate CNT/Al composites with improved composite structures and resultant mechanical properties. However, suitable processing methods endowing good CNT dispersion without small CNT structure damage are still under exploration.

1.4.1 Powder metallurgy

Powder metallurgy (PM) is a term covering a wide range of ways in which materials are made from metal powders. PM processes can avoid, or greatly reduce, the need to use processes of removing metals, thereby drastically reducing yield losses in fabrication and often resulting in a lower cost. The properties of the final product processed by PM greatly depends on the accuracy of the processing technique which is common in all PM produced components and on the secondary operations employed to the product depending on the specific application. The basic PM production stages are as follows: (1) powder preparation, (2) powder blending, (3) powder compaction, and (4) sintering of the compact. These steps are then followed by secondary operations like forging, extrusion, rolling, etc., depending on the structure requirement of the final product. Some of these operations are just employed to enhance the finishing or readjust the final dimensions. Most reported CNT/Al composites are fabricated by using the PM route [56, 58, 73], partially because the dispersion state of CNTs in powders can be largely maintained to composites.

1.4.2 Challenges in processing carbon nanotube/Al composites

1.4.2.1 Carbon nanotube dispersion

In order to achieve high strengthening effect in AMCs, CNTs were required to carry high load via a suitable CNT–Al contact interface in service. Accordingly, a homogeneous dispersion of un-bundled CNTs was basically essential for achieving the full strengthening potential of CNTs. Although many attempts [81, 84, 87, 90, 93-101] have been made to deal with CNT dispersion in composites, it is still a great challenge to uniformly disperse CNTs into AMCs with small structure damages. It is due to the multiple problems in CNT–Al system, as summarized in **Figure 1-2**.

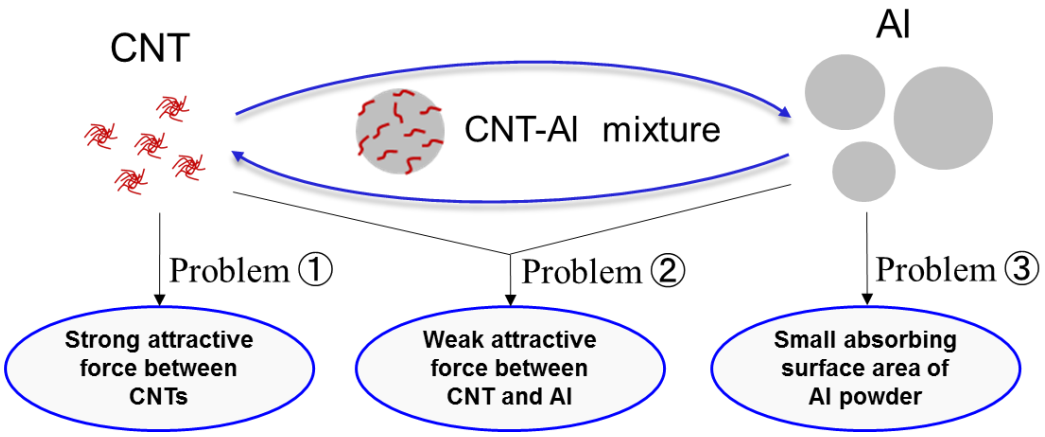

Figure 1-2. Scheme of CNT dispersion problems in CNT-Al system.

The first problem is the strong attractive force between CNTs owing to a high van der Waals (vdW) attraction energy of tube–tube interaction. The high flexibility and large aspect ratio also increase the segregation difficulty of CNTs. Another problem is that dispersed CNTs are difficult to be absorbed on Al powder surface because of the weak attractive force between CNTs and Al, resulted from their incompatibility of zeta potential [102]. Moreover, weak CNT–Al bonding might result in re-aggregation of CNTs during dispersing, post drying or consolidating processes [97]. The final problem is that the size of commonly used Al powder particles (1–200 μm) is about 3 magnitude larger than CNTs (2–100 nm), resulting in a small specific surface area for absorbing CNTs. Accordingly, homogeneous CNT dispersion with high CNT content and small structure change in composites is difficult

to obtain from previous strategies. It is noted that the three problems also exist in other CNT-metal system. Therefore, the difficulty of CNT dispersion was a wide challenge in MMCs.

1.4.2.2 Interface bonding and structural stability

A strong interface between the CNT and the matrix is necessary for the effective load transfer. The high tensile strength and the elastic modulus of the CNT are futile, if the applied load cannot be transferred to them. In CNT reinforced MMCs, some studies [10, 25] suggested that a clean interface was good for CNT-matrix bonding, because it not only prevented the structure damages of high-strength CNTs, but also led to an intimate bonding between the matrix and carbon phase. For example, in a CNT/Al composite with high tensile strength of 435 MPa [91], no Al_4C_3 phase was observed. Some other studies [94, 103, 104] argued that slight interfacial reaction can enhance the CNT-metal bonding. It was because *in situ* formed thin carbide layer not only improved the wetting conditions between CNTs and metal matrices [71] but also might lock the CNTs in place during mechanical response. Interfacial carbide phases of Ni_3C [105] and Al_2MgC_2 [103] were observed in CNT/Ni and CNT/Mg-Al composites with improved strength, respectively. It is still an open topic on the effect of interfacial carbide on the load transfer strengthening.

The solid-state reaction between Al and C, $4Al + 3C = Al_4C_3$, is related to the standard free Gibbs energy (G) which has a temperature dependence given by $\Delta G=-289512+60T$ till the T_m [73]. It indicates negative free energy for carbide formation from RT to T_m. Thus, there is always a tendency of formation of Al_4C_3 at the interface during sintering. However, the amount of Al_4C_3 is determined by the kinetics which is related to processing conditions. Although formation of a favorable thin carbide layer was theoretically applicable, it was observed rarely in CNT-MMCs. Al_4C_3 phase has been reported by many studies in sintered or hot extruded samples [18, 83, 86, 90, 94, 106]. Even Al_4C_3 has been detected in XRD patterns [16, 81, 86, 90], indicating a high volume fraction. Complete crystals of Al_4C_3 nanoparticles [94] or nano-rods [86] were often detected by TEM. For example, Kwon et al. [94] reported formation of nano-sized Al_4C_3 in spark plasma sintered samples at 600 ℃ followed by hot extrusion at 400 ℃ [15]. Interestingly, they reported a 128% improvement of tensile strength (from 85 to 194 MPa) by 5 vol.% CNT addition. These studies show that formation of Al_4C_3 does not have an adverse effect on the composite strengthening. However,

the effect of interfacial Al_4C_3 phase and complete Al_4C_3 reinforcement on mechanical properties of AMCs has not been clearly clarified.

1.4.2.3 Strengthening mechanisms

The understanding of strengthening effect of CNTs is basically essential to design composite structures for processing high-strength AMCs. There are several possible strengthening mechanisms for CNT in MMCs: (a) load transfer from matrix to CNT [107], (b) grain refining and texture strengthening by pinning effect of CNT [100], (c) dispersion strengthening of CNT [80], (d) solution strengthening by carbon atoms [108], (e) strengthening of *in situ* formed or precipitant carbide [86], and (f) thermal mismatch between CNT and matrix [107]. Among them, load transfer is most desirable because in this mechanism high load can be bear by CNTs during composite failure and thus the excellent mechanical properties of CNT are efficiently inherited to composites. However, this assumption has not been clearly verified in MMCs.

Some studies [73, 85, 91, 109] correlated mechanical properties of AMCs and structure parameters of CNTs and showed agreement with the load transfer models. However, this deduction was probably misleading because the composite strength might be contributed by other aforementioned strengthening factors or a synergy effect of several strengthening mechanisms [107]. Another means of verification was to examine the failure behaviors of CNTs during the mechanical failure of MMCs. Direct observation of CNT failure via an *in-situ* tensile test is the most convincing approach, through which the failure process of CNT in composites could be possibly witnessed and examined. *In-situ* SEM/TEM/AFM experiments have been intensively applied to investigate CNT failure in polymer matrix composites (PMCs) [110, 111] and ceramic matrix composites (CMCs) [112, 113]. However, there are limited *in-situ* studies on CNT failure mode in CNT-reinforced MMCs [109] and no clear evidence of CNT fracture was obtained.

1.5 Objectives and scopes of this research

The objective of this research is to develop high-performance CNT/Al composites and investigate the strengthening mechanisms. Attempts are made to deal with the present

challenges in processing CNT/Al composites. The main tasks are to (i) develop effective approach for homogeneous CNT dispersion in MMCs with small structure damage, (ii) investigate the relation between interfacial structure and consolidating conditions, and (iii) clarify the reinforcing mechanisms in CNT/Al composites.

The present research is composed of 7 chapters. The research flow chart is shown in **Figure 1-3**. Firstly, general introduction has been present in this Chapter 1. Then Chapter 2 provides the detailed description of the experimental procedures employed in this research. In Chapter 3, a novel method called solution ball milling is applied to homogeneously disperse CNTs in AMCs. The characteristics of this method are detailed described and compared with traditional methods. In Chapter 4, the attempt is made to control the interfacial metallic reaction in CNT/Al composites by the processing temperature. Two strategies of post heat-treatment and temperature-governed sintering are presented. In Chapter 5, the load transfer strengthening mechanism is further investigated by theoretical analysis and *in-situ* tensile tests. The mechanisms leading to the observed phenomena of CNT fracture and CNT peeling are demonstrated. Finally, the entire research works are summarized in chapter 6. Based on the present study, limitations of the present study and the future work prospects are discussed in Chapter 7.

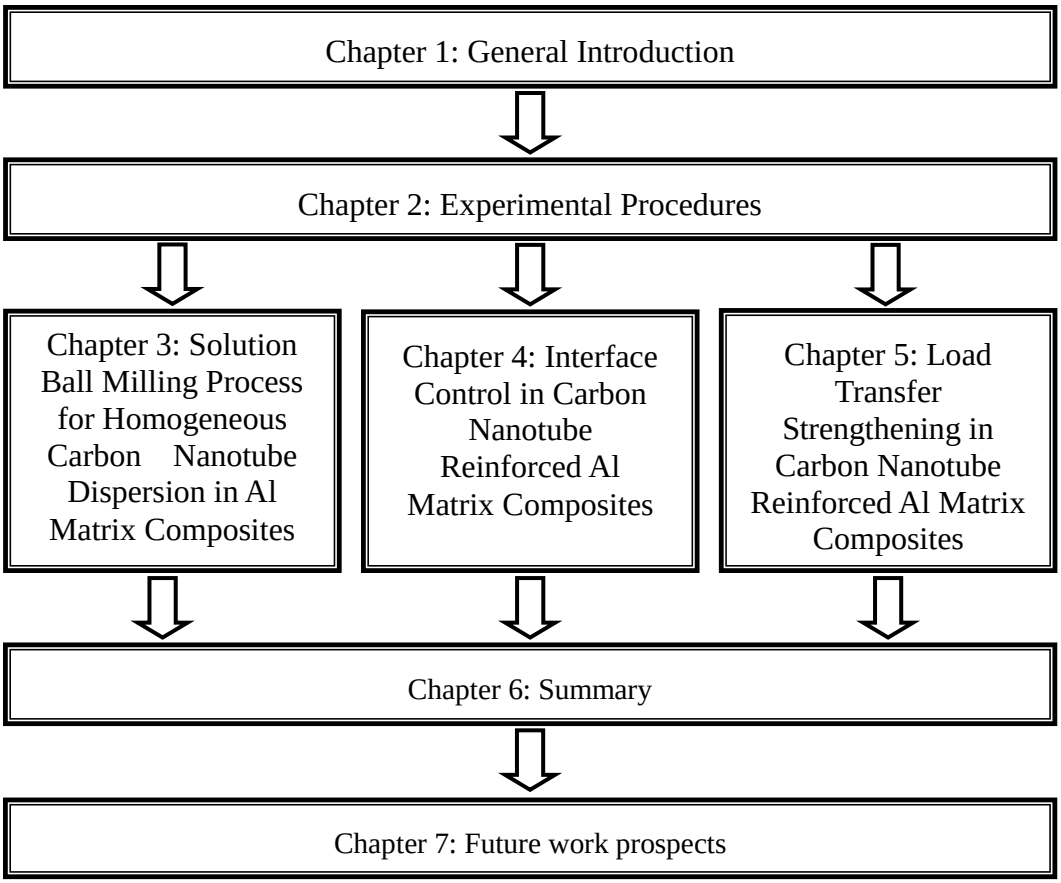

Figure 1-3. Flow chat of this study on processing and strengthening mechanism of CNT reinforced AMCs by powder metallurgy (PM) route.

References

[1] Davis JR, Davis JR. Aluminum and aluminum alloys: ASM international; 1993.
[2] Mondolfo LF. Aluminum alloys: structure and properties: Elsevier; 2013.
[3] Totten GE, MacKenzie DS. Handbook of Aluminum: Vol. 1: Physical Metallurgy and Processes: CRC Press; 2003.
[4] Davis JR. Corrosion of aluminum and aluminum alloys: Asm International; 1999.
[5] Grjotheim K, Kvande H, Zhuxian Q. Key improvements to Hall-H ¨ţoult since the end of world war II. JOM 1995;47:32-5.
[6] Starke E, Staley J. Application of modern aluminum alloys to aircraft. Progress in Aerospace Sciences 1996;32:131-72.
[7] Williams JC, Starke EA. Progress in structural materials for aerospace systems. Acta Materialia 2003;51:5775-99.
[8] Cole G, Sherman A. Light weight materials for automotive applications. Materials characterization 1995;35:3-9.

[9] Starke Jr E, Sanders Jr T, Palmer I. New approaches to alloy development in the Al-Li system. JOM 1981;33:24-33.
[10] Cheng S, Zhao Y, Zhu Y, Ma E. Optimizing the strength and ductility of fine structured 2024 Al alloy by nano-precipitation. Acta Materialia 2007;55:5822-32.
[11] Banhart J, Chang CST, Liang Z, Wanderka N, Lay MD, Hill AJ. Natural Aging in Al‐Mg‐Si Alloys‐A Process of Unexpected Complexity. Advanced engineering materials 2010;12:559-71.
[12] San-Martin A, Manchester F. The al-h (aluminum-hydrogen) system. Journal of phase equilibria 1992;13:17-21.
[13] Zhao YH, Liao XZ, Cheng S, Ma E, Zhu YT. Simultaneously Increasing the Ductility and Strength of Nanostructured Alloys. Advanced Materials 2006;18:2280-3.
[14] Sun PL, Yu CY, Kao PW, Chang CP. Influence of boundary characters on the tensile behavior of sub-micron-grained aluminum. Scripta Materialia 2005;52:265-9.
[15] Khan AS, Farrokh B, Takacs L. Effect of grain refinement on mechanical properties of ball-milled bulk aluminum. Materials Science and Engineering: A 2008;489:77-84.
[16] Witkin D, Lavernia EJ. Synthesis and mechanical behavior of nanostructured materials via cryomilling. Progress in Materials Science 2006;51:1-60.
[17] Han BQ, Lavernia EJ, Mohamed FA. Mechanical properties of nanostructured materials. Rev Adv Mater Sci 2005;9:1-16.
[18] Witkin D, Lee Z, Rodriguez R, Nutt S, Lavernia E. Al–Mg alloy engineered with bimodal grain size for high strength and increased ductility. Scripta Materialia 2003;49:297-302.
[19] Meyers MA, Chawla KK. Mechanical behavior of materials: Cambridge University Press Cambridge; 2009.
[20] Kang Y-C, Chan SL-I. Tensile properties of nanometric Al2O3 particulate-reinforced aluminum matrix composites. Materials Chemistry and Physics 2004;85:438-43.
[21] Casati R, Vedani M. Metal Matrix Composites Reinforced by Nano-Particles—A Review. Metals 2014;4:65-83.
[22] Tjong SC. Novel Nanoparticle-Reinforced Metal Matrix Composites with Enhanced Mechanical Properties. Advanced Engineering Materials 2007;9:639-52.
[23] Hamdy AS, Alfosail F, Gasem Z. Eco-friendly, cost-effective silica-based protective coating for an A6092/SiC/17.5 p aluminum metal matrix composite. Electrochimica Acta 2013;89:749-55.
[24] Shang JK, Ritchie R. On the particle-size dependence of fatigue-crack propagation thresholds in SiC-particulate-reinforced aluminum-alloy composites: role of crack closure and crack trapping. Acta Metallurgica 1989;37:2267-78.
[25] Kamat S, Hirth J, Mehrabian R. Mechanical properties of particulate-reinforced aluminum-matrix composites. Acta Metallurgica 1989;37:2395-402.
[26] Arik H. Production and characterization of in situ Al4C3 reinforced aluminum-based composite produced by mechanical alloying technique. Materials & Design 2004;25:31-40.
[27] Besterci M. Preparation, microstructure and properties of Al–Al4C3 system produced by mechanical alloying. Materials & Design 2006;27:416-21.
[28] Fogagnolo JB, Robert MH, Torralba JM. Mechanically alloyed AlN particle-reinforced Al-6061 matrix composites: Powder processing, consolidation and mechanical strength and hardness of the as-extruded materials. Materials Science and Engineering: A 2006;426:85-94.

[29] Jiang L, Wen H, Yang H, Hu T, Topping T, Zhang D, et al. Influence of length-scales on spatial distribution and interfacial characteristics of B4C in a nanostructured Al matrix. Acta Materialia 2015;89:327-43.
[30] Zheng R, Yang H, Liu T, Ameyama K, Ma C. Microstructure and mechanical properties of aluminum alloy matrix composites reinforced with Fe-based metallic glass particles. Materials & Design 2014;53:512-8.
[31] Goussous S, Xu W, Wu X, Xia K. Al–C nanocomposites consolidated by back pressure equal channel angular pressing. Composites Science and Technology 2009;69:1997-2001.
[32] Choi HJ, Shin JH, Bae DH. Self-assembled network structures in Al/C60 composites. Carbon 2010;48:3700-7.
[33] Prasad S, Asthana R. Aluminum metal-matrix composites for automotive applications: tribological considerations. Tribology Letters 2004;17:445-53.
[34] Deuis R, Subramanian C, Yellup J. Dry sliding wear of aluminium composites ¡ª review. Composites Science and Technology 1997;57:415-35.
[35] Lloyd D. Particle reinforced aluminium and magnesium matrix composites. International Materials Reviews 1994;39:1-23.
[36] Chawla N, Shen Y-L. Mechanical behavior of particle reinforced metal matrix composites. Advanced engineering materials 2001;3:357-70.
[37] Cox H. The elasticity and strength of paper and other fibrous materials. British journal of applied physics 1952;3:72.
[38] Kelley A, Tyson W. Tensile Properties of Fiber-Reinforced Metals. Journal of Mechanical and Physical Solids 1965;13:329-50.
[39] Mallick PK. Fiber-reinforced composites: materials, manufacturing, and design: CRC press; 2007.
[40] Qin Y, He S, Yang D. Effect of thermal ¨Cmechanical cycling on thermal expansion behavior of boron fiber-reinforced aluminum matrix composite. Materials chemistry and physics 2004;86:204-9.
[41] Nair S, Tien J, Bates R. SiC-reinforced aluminium metal matrix composites. International Metals Reviews 1985;30:275-90.
[42] Woo S-C, Choi N-S, Cho N. Characterization of the fracture process of notched glass fiber/aluminum hybrid laminates by acoustic emission. Composites Science and Technology 2008;68:1521-30.
[43] Xu W, Chenchong W, Zhichao Z, Ping L, Yanhua S, Guofu Z. Interfacial microstructure and growth mechanism of Al4C3 in Grf/Al composites fabricated by liquid pressure method. Micron 2014;65:10-4.
[44] Yamaguchi M, Meng F, Firestein K, Tsuchiya K, Golberg D. Powder metallurgy routes toward aluminum boron nitride nanotube composites, their morphologies, structures and mechanical properties. Materials Science and Engineering: A 2014;604:9-17.
[45] Kuzumaki T, Miyazawa K, Ichinose H, Ito K. Processing of carbon nanotube reinforced aluminum composite. Journal of Materials Research 1998;13:2445-9.
[46] Wei X, Wang MS, Bando Y, Golberg D. Tensile Tests on Individual Multi©\Walled Boron Nitride Nanotubes. Advanced Materials 2010;22:4895-9.
[47] Demczyk B, Wang Y, Cumings J, Hetman M, Han W, Zettl A, et al. Direct mechanical measurement of the tensile strength and elastic modulus of multiwalled carbon nanotubes. Materials Science and Engineering: A 2002;334:173-8.

[48] Eshelby J. Dislocations as a cause of mechanical damping in metals. Proceedings of the Royal Society of London A: Mathematical, Physical and Engineering Sciences: The Royal Society; 1949. p. 396-416.
[49] Hansen N. Hall–Petch relation and boundary strengthening. Scripta Materialia 2004;51:801-6.
[50] Taylor GI. The mechanism of plastic deformation of crystals. Part I. Theoretical. Proceedings of the Royal Society of London Series A, Containing Papers of a Mathematical and Physical Character 1934:362-87.
[51] Ashby M. The theory of the critical shear stress and work hardening in dispersion-hardened crystals. DTIC Document; 1966.
[52] Iijima S. Helical microtubules of graphitic carbon. Nature 1991;354:56-8.
[53] Iijima S, Ichihashi T. Single-shell carbon nanotubes of 1-nm diameter. 1993.
[54] Popov VN. Carbon nanotubes: properties and application. Materials Science and Engineering: R: Reports 2004;43:61-102.
[55] Esawi AMK, Farag MM. Carbon nanotube reinforced composites: Potential and current challenges. Materials & Design 2007;28:2394-401.
[56] Bakshi SR, Lahiri D, Agarwal A. Carbon nanotube reinforced metal matrix composites - a review. International Materials Reviews 2010;55:41-64.
[57] Shulaker MM, Hills G, Patil N, Wei H, Chen HY, Wong HS, et al. Carbon nanotube computer. Nature 2013;501:526-30.
[58] Tjong SC. Recent progress in the development and properties of novel metal matrix nanocomposites reinforced with carbon nanotubes and graphene nanosheets. Materials Science and Engineering: R: Reports 2013;74:281-350.
[59] De Volder MF, Tawfick SH, Baughman RH, Hart AJ. Carbon nanotubes: present and future commercial applications. Science 2013;339:535-9.
[60] Choudhary V, Gupta A. Polymer/carbon nanotube nanocomposites. Carbon Nanotubes-Polymer Nanocomposites 2011:65-90.
[61] Barber AH, Andrews R, Schadler LS, Wagner HD. On the tensile strength distribution of multiwalled carbon nanotubes. Applied Physics Letters 2005;87:203106.
[62] Munir KS, Kingshott P, Wen C. Carbon Nanotube Reinforced Titanium Metal Matrix Composites Prepared by Powder Metallurgy—A Review. Critical Reviews in Solid State and Materials Sciences 2014;40:38-55.
[63] Duan WH, Wang Q, Liew KM, He XQ. Molecular mechanics modeling of carbon nanotube fracture. Carbon 2007;45:1769-76.
[64] Peckner D, Bernstein IM. Handbook of stainless steels: McGraw-Hill New York, NY; 1977.
[65] Schadler LS, Giannaris SC, Ajayan PM. Load transfer in carbon nanotube epoxy composites. Applied Physics Letters 1998;73:3842.
[66] Coleman JN, Khan U, Blau WJ, Gun'ko YK. Small but strong: A review of the mechanical properties of carbon nanotube–polymer composites. Carbon 2006;44:1624-52.
[67] Hussain F. Review article: Polymer-matrix Nanocomposites, Processing, Manufacturing, and Application: An Overview. Journal of Composite Materials 2006;40:1511-75.
[68] Du JH. The present status and key problems of carbon nanotube based polymer composites. eXPRESS Polymer Letters 2007;1:253-73.

[69] Ma P-C, Siddiqui NA, Marom G, Kim J-K. Dispersion and functionalization of carbon nanotubes for polymer-based nanocomposites: A review. Composites Part A: Applied Science and Manufacturing 2010;41:1345-67.
[70] Rahmat M, Hubert P. Carbon nanotube–polymer interactions in nanocomposites: A review. Composites Science and Technology 2011;72:72-84.
[71] Dujardin E, Ebbesen T, Hiura H, Tanigaki K. Capillarity and wetting of carbon nanotubes. Science 1994;265:1850-2.
[72] Nuriel S, Liu L, Barber A, Wagner H. Direct measurement of multiwall nanotube surface tension. Chemical Physics Letters 2005;404:263-6.
[73] Bakshi SR, Agarwal A. An analysis of the factors affecting strengthening in carbon nanotube reinforced aluminum composites. Carbon 2011;49:533-44.
[74] Uozumi H, Kobayashi K, Nakanishi K, Matsunaga T, Shinozaki K, Sakamoto H, et al. Fabrication process of carbon nanotube/light metal matrix composites by squeeze casting. Materials Science and Engineering: A 2008;495:282-7.
[75] Zhou S-m, Zhang X-b, Ding Z-p, Min C-y, Xu G-l, Zhu W-m. Fabrication and tribological properties of carbon nanotubes reinforced Al composites prepared by pressureless infiltration technique. Composites Part A: Applied Science and Manufacturing 2007;38:301-6.
[76] Kang K, Bae G, Won J, Lee C. Mechanical property enhancement of kinetic sprayed Al coatings reinforced by multi-walled carbon nanotubes. Acta Materialia 2012;60:5031-9.
[77] Bakshi SR, Singh V, Seal S, Agarwal A. Aluminum composite reinforced with multiwalled carbon nanotubes from plasma spraying of spray dried powders. Surface and Coatings Technology 2009;203:1544-54.
[78] Choi H, Shin J, Min B, Park J, Bae D. Reinforcing effects of carbon nanotubes in structural aluminum matrix nanocomposites. Journal of Materials Research 2011;24:2610-6.
[79] Choi HJ, Shin JH, Bae DH. Grain size effect on the strengthening behavior of aluminum-based composites containing multi-walled carbon nanotubes. Composites Science and Technology 2011;71:1699-705.
[80] Yoo SJ, Han SH, Kim WJ. Strength and strain hardening of aluminum matrix composites with randomly dispersed nanometer-length fragmented carbon nanotubes. Scripta Materialia 2013;68:711-4.
[81] Liu ZY, Xiao BL, Wang WG, Ma ZY. Singly dispersed carbon nanotube/aluminum composites fabricated by powder metallurgy combined with friction stir processing. Carbon 2012;50:1843-52.
[82] Liu ZY, Xiao BL, Wang WG, Ma ZY. Elevated temperature tensile properties and thermal expansion of CNT/2009Al composites. Composites Science and Technology 2012;72:1826-33.
[83] Liu ZY, Xu SJ, Xiao BL, Xue P, Wang WG, Ma ZY. Effect of ball-milling time on mechanical properties of carbon nanotubes reinforced aluminum matrix composites. Composites Part A: Applied Science and Manufacturing 2012;43:2161-8.
[84] He C, Zhao N, Shi C, Du X, Li J, Li H, et al. An Approach to Obtaining Homogeneously Dispersed Carbon Nanotubes in Al Powders for Preparing Reinforced Al-Matrix Composites. Advanced Materials 2007;19:1128-32.
[85] Esawi AMK, Morsi K, Sayed A, Taher M, Lanka S. Effect of carbon nanotube (CNT) content on the mechanical properties of CNT-reinforced aluminium composites. Composites Science and Technology 2010;70:2237-41.

[86] Esawi AMK, Morsi K, Sayed A, Taher M, Lanka S. The influence of carbon nanotube (CNT) morphology and diameter on the processing and properties of CNT-reinforced aluminium composites. Composites Part A: Applied Science and Manufacturing 2011;42:234-43.
[87] Deng C, Zhang X, Wang D, Lin Q, Li A. Preparation and characterization of carbon nanotubes/aluminum matrix composites. Materials Letters 2007;61:1725-8.
[88] Chunfeng D, Xuexi Z, Dezun W. Chemical stability of carbon nanotubes in the 2024Al matrix. Materials Letters 2007;61:904-7.
[89] Liao J, Tan M-J. Mixing of carbon nanotubes (CNTs) and aluminum powder for powder metallurgy use. Powder Technology 2011;208:42-8.
[90] Yang X, Shi C, He C, Liu E, Li J, Zhao N. Synthesis of uniformly dispersed carbon nanotube reinforcement in Al powder for preparing reinforced Al composites. Composites Part A: Applied Science and Manufacturing 2011;42:1833-9.
[91] Jiang L, Li Z, Fan G, Cao L, Zhang D. The use of flake powder metallurgy to produce carbon nanotube (CNT)/aluminum composites with a homogenous CNT distribution. Carbon 2012;50:1993-8.
[92] Jiang L, Li Z, Fan G, Cao L, Zhang D. Strong and ductile carbon nanotube/aluminum bulk nanolaminated composites with two-dimensional alignment of carbon nanotubes. Scripta Materialia 2012;66:331-4.
[93] Esawi A, Morsi K. Dispersion of carbon nanotubes (CNTs) in aluminum powder. Composites Part A: Applied Science and Manufacturing 2007;38:646-50.
[94] Kwon H, Estili M, Takagi K, Miyazaki T, Kawasaki A. Combination of hot extrusion and spark plasma sintering for producing carbon nanotube reinforced aluminum matrix composites. Carbon 2009;47:570-7.
[95] Lim DK, Shibayanagi T, Gerlich AP. Synthesis of multi-walled CNT reinforced aluminium alloy composite via friction stir processing. Materials Science and Engineering: A 2009;507:194-9.
[96] Pérez-Bustamante R, Gómez-Esparza CD, Estrada-Guel I, Miki-Yoshida M, Licea-Jiménez L, Pérez-García SA, et al. Microstructural and mechanical characterization of Al–MWCNT composites produced by mechanical milling. Materials Science and Engineering: A 2009;502:159-63.
[97] Poirier D, Gauvin R, Drew RAL. Structural characterization of a mechanically milled carbon nanotube/aluminum mixture. Composites Part A: Applied Science and Manufacturing 2009;40:1482-9.
[98] Jiang L, Fan G, Li Z, Kai X, Zhang D, Chen Z, et al. An approach to the uniform dispersion of a high volume fraction of carbon nanotubes in aluminum powder. Carbon 2011;49:1965-71.
[99] Liao J, Tan M-J. A simple approach to prepare Al/CNT composite: Spread–Dispersion (SD) method. Materials Letters 2011;65:2742-4.
[100] Nam DH, Cha SI, Lim BK, Park HM, Han DS, Hong SH. Synergistic strengthening by load transfer mechanism and grain refinement of CNT/Al–Cu composites. Carbon 2012;50:2417-23.
[101] Simões S, Viana F, Reis MAL, Vieira MF. Improved dispersion of carbon nanotubes in aluminum nanocomposites. Composite Structures 2014;108:992-1000.

[102] Sun Z, Nicolosi V, Rickard D, Bergin SD, Aherne D, Coleman JN. Quantitative evaluation of surfactant-stabilized single-walled carbon nanotubes: dispersion quality and its correlation with zeta potential. The Journal of Physical Chemistry C 2008;112:10692-9.
[103] Fukuda H, Kondoh K, Umeda J, Fugetsu B. Interfacial analysis between Mg matrix and carbon nanotubes in Mg–6wt.% Al alloy matrix composites reinforced with carbon nanotubes. Composites Science and Technology 2011;71:705-9.
[104] Ci L, Ryu Z, Jin-Phillipp NY, Rühle M. Investigation of the interfacial reaction between multi-walled carbon nanotubes and aluminum. Acta Materialia 2006;54:5367-75.
[105] Hwang J, Lim B, Tiley J, Banerjee R, Hong S. Interface analysis of ultra-high strength carbon nanotube/nickel composites processed by molecular level mixing. Carbon 2013;57:282-7.
[106] He CN, Zhao NQ, Shi CS, Song SZ. Mechanical properties and microstructures of carbon nanotube-reinforced Al matrix composite fabricated by in situ chemical vapor deposition. Journal of Alloys and Compounds 2009;487:258-62.
[107] George R, Kashyap KT, Rahul R, Yamdagni S. Strengthening in carbon nanotube/aluminium (CNT/Al) composites. Scripta Materialia 2005;53:1159-63.
[108] Li S, Sun B, Imai H, Kondoh K. Powder metallurgy Ti–TiC metal matrix composites prepared by in situ reactive processing of Ti-VGCFs system. Carbon 2013;61:216-28.
[109] Boesl B, Lahiri D, Behdad S, Agarwal A. Direct observation of carbon nanotube induced strengthening in aluminum composite via in situ tensile tests. Carbon 2014;69:79-85.
[110] Qian D, Dickey EC, Andrews R, Rantell T. Load transfer and deformation mechanisms in carbon nanotube-polystyrene composites. Applied Physics Letters 2000;76:2868.
[111] Hwang GL, Shieh YT, Hwang KC. Efficient Load Transfer to Polymer©\Grafted Multiwalled Carbon Nanotubes in Polymer Composites. Advanced Functional Materials 2004;14:487-91.
[112] Xia Z, Riester L, Curtin W, Li H, Sheldon B, Liang J, et al. Direct observation of toughening mechanisms in carbon nanotube ceramic matrix composites. Acta Materialia 2004;52:931-44.
[113] Yamamoto G, Shirasu K, Hashida T, Takagi T, Suk JW, An J, et al. Nanotube fracture during the failure of carbon nanotube/alumina composites. Carbon 2011;49:3709-16.

Chapter 2
Experimental Procedures

2.1 Raw materials

2.1.1 Aluminum powders

Two kinds of commercially pure aluminum (Al) powders (99.9% in purity) with different particle sizes were used as the raw materials in this study. The coarse Al powder had a particle size range of 108-180 μm. The fine powder had a mean particle size of 20 μm. Both the two powders show tear-drop shapes and supplied by Kojundo Chemical Laboratory CO., Japan. The morphology and chemical compositions of those starting Al powders are shown in **Figure 2-1** and **Table 2-1**, respectively.

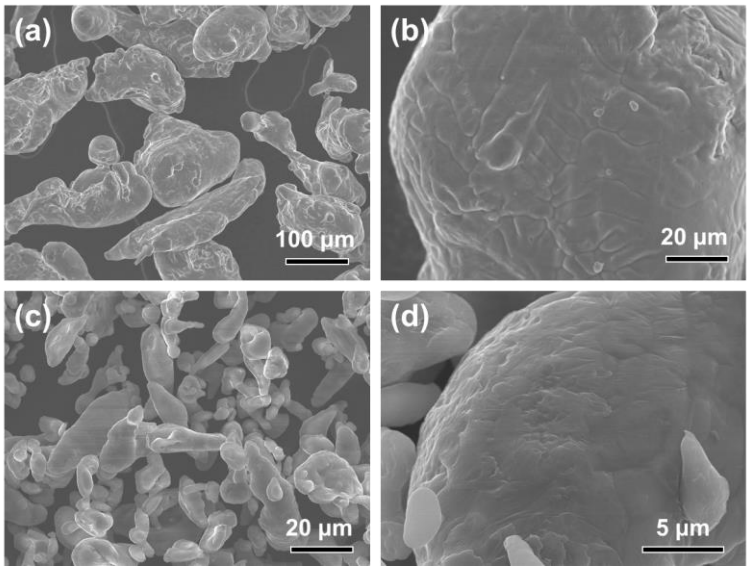

Figure 2-1. Commercial pure (a,b) coarse and (c,d) fine Al powders used in this study.

Table 2-1. Chemical compositions of raw Al powders used in this study (wt.%).

Materials	Purity	Cu	Fe	Si	Ti
Coarse Al	>99.9	0.002	0.02	0.01	Bal.
Fine Ti	>99.9	-	0.08	0.03	Bal.

2.1.2 Carbon reinforcing materials

The elemental carbon has many allotropes with various structures such as graphite, diamond and fullerene [1]. In this study, multi-walled carbon nanotubes (MWCNTs) were used as the reinforcing materials because of their high aspect ratios, ultra-high strength and ultra-high modulus [2-4]. Two kinds of MWCNTs with distinct sizes were used. The coarse MWCNTs with about 100 nm in diameter and ~15 μm in length are produced by Showa Denko Group, Japan. The fine CNTs have an average diameter of ~15 nm and an average length of ~1 μm were purchased from Bayer Material Science. The morphologies of coarse and fine CNTs observed at different magnifications are shown in **Figure 2-2** and **Figure 2-3**, respectively. The walls and the hollow channel of the two kinds of CNTs could be observed in Figure 2-2c and d and Figure 2-3d.

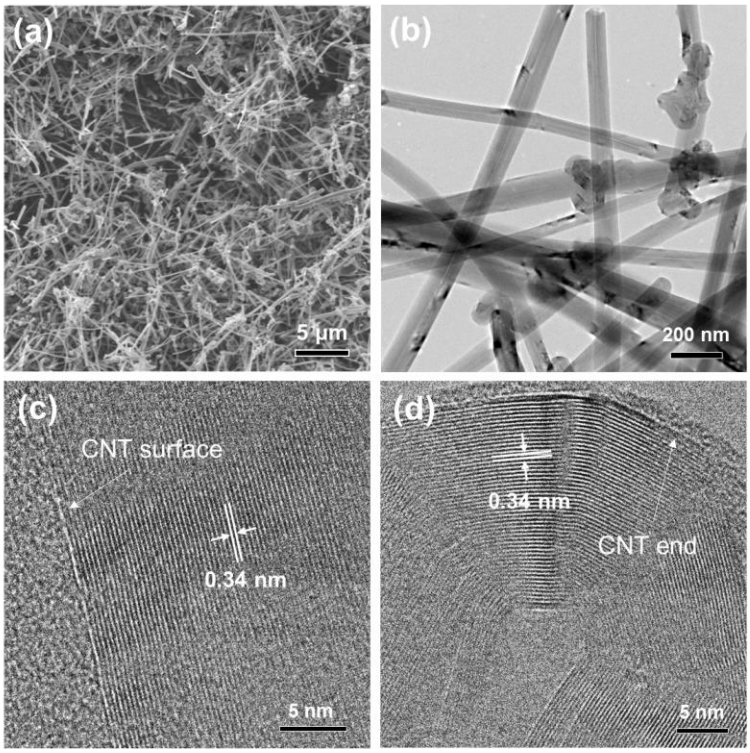

Figure 2-2. SEM (a) and TEM (b-d) observations on raw powders of coarse CNTs.

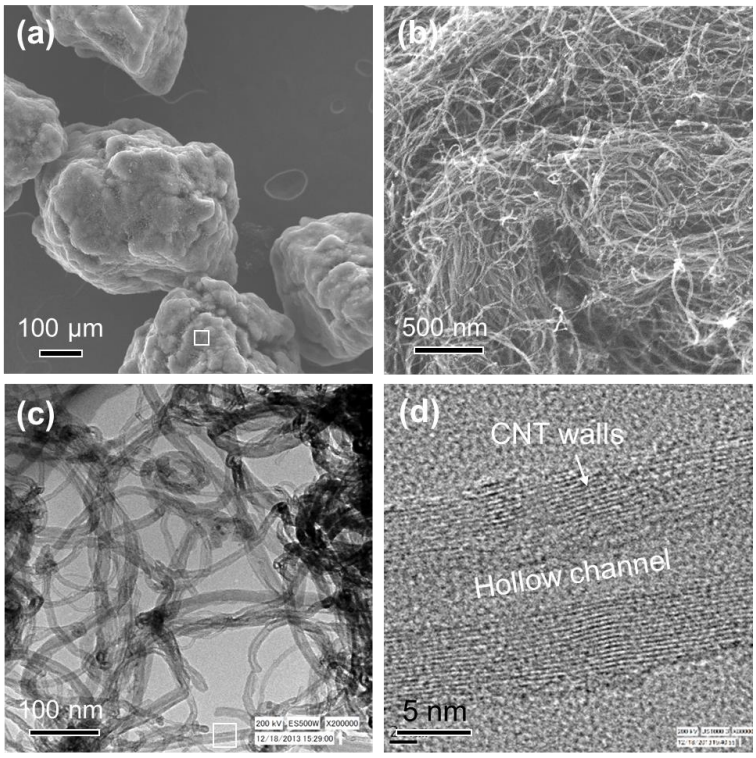

Figure 2-3. SEM (a,b) and TEM (c,d) observations on raw powders of fine CNTs. (b) and (d) show box areas in (a) and (c), respectively.

2.2 Dispersion techniques

2.2.1 Solution ball milling

A novel solution ball milling (SBM) process was developed in this study, as schematically illustrated in **Figure 2-4**. The process mainly includes two steps. First is to prepare CNT-dispersed solution. Various solutions [5, 6] have been reported to effectively disperse CNTs. In this study, isopropyl alcohol (IPA) based solution with ~1 wt.% zwitterionic surfactants [7-9] was used to obtain 1 wt.% CNT solution. The surfactants had both hydrophobic and hydrophilic groups to disperse individual CNTs in the IPA based solution. The fine MWCNT was used in this study. The detailed description of the working mechanism of surfactants for CNT debinding could be found elsewhere [7].

In the second step, the slurry of 160 g prepared CNT solution and 160 g Al powders (Kojundo Chemical Laboratory Co., Japan) were mixed using a planetary ball milling machine. Al slurry containing 1 wt.% CNTs was sealed in a zirconia (ZrO_2) jar together with

ZrO_2 milling balls (640 g in diameter of 10 mm and 160 g in diameter of 5 mm). The revolution speed was 200 rpm. The ball milling time was 60 min with an interim period of 600 s for every 600 s in order to prevent the over-heating behavior. During ball milling, flaky Al powder was gradually produced under the impact between the high-energy balls. Simultaneously, dispersed CNTs in the solution was impacted on the flaky powder surface, as shown in Figure 2-4. Owing to the mechanical impact, CNTs were strongly attached on the Al surface with a complete CNT-Al contact from the limited contact before impact. After milling, the slurry was transferred to a beaker and stand for ~900 s to settle CNT-Al powders down. The following procedure is to pour out the upper solution containing surfactants and free CNTs.

Finally, the powder was dried in an oven at 353 K for 1.8 ks in an argon (Ar) gas atmosphere. Al slurries containing 0.5 wt.% CNTs and containing no CNT were also processed under the same SBM conditions. Alcohol (99.5% purity) was used to make up IPA to the same solution volume with 1 wt.% CNTs. To share the advantages of SBM over the traditional techniques, commonly used solution coating and high energy ball milling process were also performed to the same Al and CNT powders.

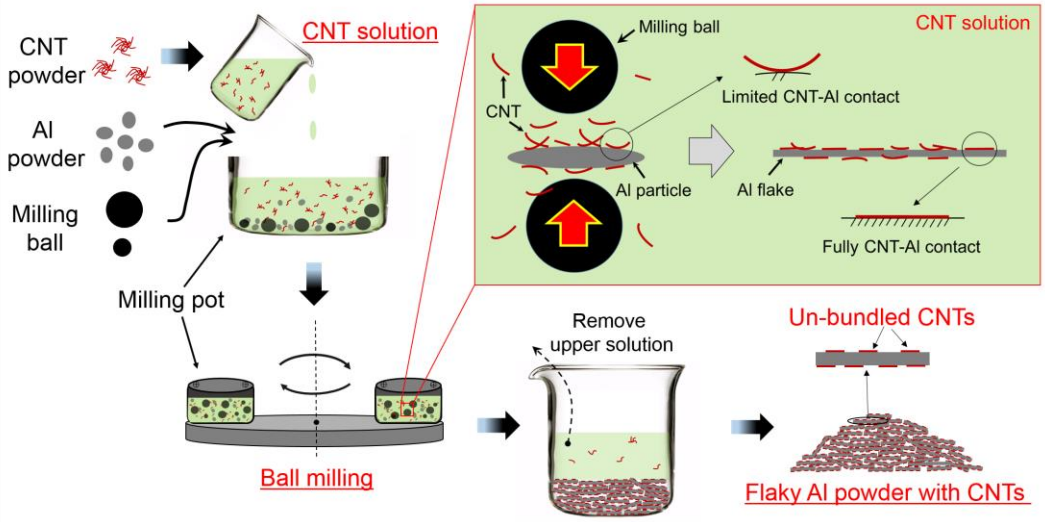

Figure 2-4. Scheme of solution ball milling (SBM) process for CNT dispersion.

2.2.2 Solution coating

The solution coating (SC) technique consists of two processing steps. First is to prepare the aforementioned CNT-dispersed solution in Section 2.2.1. In the second step, the prepared CNT solution (100 g) and Al powders (80 g) were put into a plastic bottle. The slurry was mixed on a table milling machine for 3.6 ks with a rotation speed of 120 rpm. After coating treatment, the CNT-Al powder slurry was transferred to a corundum crucible and dried in an oven at 353 K for 1.8 ks in an Ar gas atmosphere. Two kinds of Al powders, i.e. raw fine Al powder and flaky Al powder, were used in the solution coating process. The flaky Al powder was prepared by the high energy ball milling process, as described in the following section.

2.2.3 High energy ball milling

The fine CNT and fine Al powder were mixed through high energy ball milling (HEBM) using a planetary ball milling machine. The powder mixture, which consisted of Al powder, 1 wt.% (1.3 vol.%) CNTs and 2 wt.% stearic acid ($C_{18}H_{36}O_2$, process control agent, PCA) powder, were blended first using a rocking milling machine (RM-0.5, Seiwa Giken Co. Ltd., Japan) for 7.2 ks. Volume content of CNTs was estimated using CNT density of 1.8 g cm^{-3} and Al density of 2.7 g cm^{-3}. The blended powder mixture was sealed in a ZrO_2 jar (500 mL in volume) together with ZrO_2 milling balls (10 mm in diameter, ball to powder mass ratio: 5). The jar was aerated with argon (Ar) gas to protect Al powders from oxidation. The revolution speed was 200 rpm. The ball milling time was 3.6-43.2 ks with an interim break of 600 s for every 900 s to prevent the jar from over-heating. The PCA in the milled powder was burned in a vacuum furnace at 450 ℃ for 1.8 ks. Raw pure Al without adding CNTs were also processed by HEBM to prepare flaky Al powders for the coating processes.

2.2.4 Mechanical solution coating

In order to homogeneously disperse CNTs into Al matrix with minor structure damage, an improved coating process called mechanical solution coating (MSC) process was also developed. The fabrication of CNT/Al composites mainly includes three steps. First is to prepare the 1 wt.% CNT solution as described in the SBM process in Section 2.2.1. The second step is to prepare flaky Al particles for the mechanical coating process by HEBM process. 1000 g flaky Al powder was prepared using the HEBM process as described in

Section 2.2.3. The third step is to disperse CNTs on prepared flaky Al powder surface by mechanical coating process. Flaky Al powder (80 g) bathed in isopropyl alcohol (IPA) based solution with ~1 wt.% zwitterionic surfactants and 1 wt.% CNTs in a plastic bottle on a rocking ball milling machine for 7.2 ks. 40 g ZrO_2 media balls were added to assist the coating of CNTs on flaky powders.

2.2.5 Low energy blending

A facile low energy blending (LEB) process was used to mix two powder systems. One is the raw coarse Al powder and coarse CNT powder, and the other one is the fine Al powder and fine CNT powder. Al powder (120 g) with 0.6 wt.% course CNTs (or 1 wt.% fine CNTs) and 12 g Al_2O_3 media balls in diameter of 5 mm were put into a plastic bottle, and mixed on a rocking milling machine (Seiwa Giken, Japan) for 14.4 ks at 200 rpm.

2.3 Consolidation of powders

2.3.1 Spark plasma sintering

The spark plasma sintering (SPS, SPS-1030S, SPS Syntex), as schematically illustrated in **Figure 2-5**, was used to primarily consolidate the pure Al and CNT-Al composite powders for preparation of the sintered Al composite billets. Approximately 60 g powders were poured into a graphite die with an inner diameter of 42 mm. With the fine Al and fine CNT powder dispersed by the SBM process, the SPS is conducted at sintering temperature (T) of 600 ℃ with sintering time (t) of 1.8 ks. With the flaky Al and fine CNT composite powder by mechanical solution coating process, SPS was carried out at various temperatures in the range of 427-627 ℃ with sintering time of 3.6 ks. With the coarse Al-coarse CNT powder mixed by LEB, the SPS temperature was 550 ℃ and holding time is 1.8 ks. Following hot-extrusion was applied on sintered samples. During sintering, the vacuum atmosphere was kept at <5 Pa. The heating rate is 20 ℃/min and the applied pressure during the SPS process is 30 MPa.

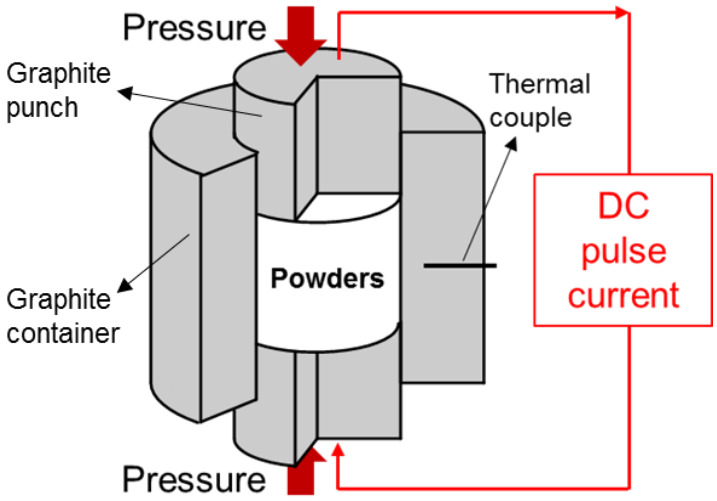

Figure 2-5. Schematic illustration of Spark Plasma Sintering (SPS) process.

2.3.2 Cold compaction

Cold compaction (CC) was applied on the flaky Al and fine CNT powder dispersed by solution coating using a 2000 kN hydraulic press machine (SHP-200-450, Shibayama). The powder was pressed under a pressure of ~600 MPa for ~10 s. The container used for compaction was with an inner diameter of 42 mm. Following hot-extrusion was also applied on compacted samples.

2.3.3 Hot extrusion

A final consolidation by hot-extrusion (HE) is necessary to make a full density and shaping of the sintered or compacted pure Al and AMC billets as rods. **Figure 2-6** shows a drawing of diagram of the extrusion die sets used in this experiment. The SPSed and compacted Al billet with 42 mm diameter and about 10 mm height was heated in a ULVAC infrared gold image furnace. The target heating temperature can be accelerated in a few minutes. The heating rate of 2 ℃/s was used to heat the SPSed billets at temperatures (T') of 400 ℃ and 500 ℃ with holding time of 180s under an Ar protective atmosphere. After the heating step, the heated billets were immediately extruded using a 2000 kN hydraulic press machine. To prevent heat loss of the heated billets during extrusion, the extrusion die sets, die, container and dummy plate, were heated at 400 ℃ in a muffle furnace for at least two hours before start of the extrusion process. Both the extrusion speeds (v) of 0.5 and 3 mm/s

were used in this experiment. The extrusion ratios (ER) of 37 and 13 were used to produce an extrusion rod of 12mm and 7 mm diameter, respectively. The consolidation parameters for the different powders used in this study are summarized in **Table 2-2**.

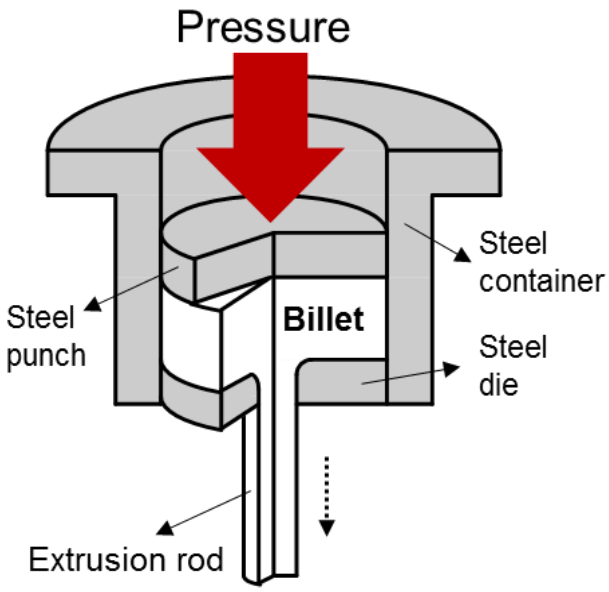

Figure 2-6. Drawing diagram of hot extrusion process.

Table 2-2. Consolidation routes for different powders in the study.

No.	Powder size		Dispersion method	SPS *T* (℃); *t* (ks)	CC	HE *T'* (℃); *v* (mm/s); ER	Chapter No.
	Al	CNT					
1	Fine	Fine	SBM	600; 1.8	-	500; 3; 37	3
2	Flaky	Fine	SC	-	Yes	500; 3; 37	4
3	Flaky	Fine	MSC	427-627; 3.6	-	400; 3; 37	4
4	Coarse	Coarse	LEB	550; 1.8		500; 0.5; 12	5

2.3.4 Annealing process

The annealing process was applied to consolidated samples processed under the route No. 2 in Table 2-2. The samples were heat-treated in a vacuum furnace at temperatures of 450-650^{o}C for 60 min with a heating-up speed of 20^{o}C/min. The vacuum was controlled at 20-50 Pa. The samples were then cooled down in the furnace after heat treatment.

2.4 Microstructural characterizations

2.4.1 Sample preparation and characterizations

2.4.1.1 OM, SEM and XRD

Microstructure and phase characterization of the processed materials were investigated by optical microscopy (OM), scanning electron microscopy (SEM) and X-ray diffraction (XRD) techniques. The extruded rod was cut in the extrusion direction and grinded with SiC abrasive paper from 400#, 800#, 1500# to 4000# grit, and then polished using 0.025 μm diamond suspension. OM and SEM were used to examine the microstructures at comparably low magnifications. XRD measurements were carried out using a Cu Kα radiation source with scanning speed of $2°\cdot min^{-1}$.

2.4.1.2 FIB and TEM

High magnification microstructures were examined by transmission electron microscopy (TEM, JEM-2010, JEOL, Japan) operated at 200 kV. TEM samples of extruded materials were prepared using a focused ion beam (FIB, HITACHI FB-2000S) system operated under voltage of 8 kV and current of 3 μA. Liquid gallium (Ga) metal was used as the ion source to mill the sample to a thickness of ~100 nm.

2.4.1.3 EBSD

Information on the crystal orientation, including grain size and the rotation angles of grain boundaries, was analyzed using the electron backscatter diffraction (EBSD) technique. EBSD was performed using a TSL (TSL DigiView IV; EDAX) instrument attached to the FESEM and operated at 20 kV. Before EBSD, the polished sample was mechanically vibrated in a silica solution on a vibratory polisher machine (VibroMet, BUEHLER) for 3.6 ks to remove the residual stress. During EBSD analysis, the sample was tilted with 70 ° to the receiving instrument. The average grain size was measured from ~200 grains from EBSD images.

2.4.1.4 Raman analysis

The carbon-related phase compositions in CNT/Al composites were examined by Raman spectroscopy (Microscopic Laser Raman Spectrometer, LabRAM ARAMIS, HORIBA, Japan). Raman spectra were acquired using the 532 nm line of a diode-pumped solid-state laser in the spectral range from 200 cm^{-1} to 1800 cm^{-1}.

2.4.2 Carbon element analysis

To measure the CNT content, weight concentration of carbon element in the processed powders was analyzed on an infrared absorption carbon analyzer (EMIA-221V20K, Horiba). The samples used for element analysis were cut from the specimens after tensile test with massive of 0.05-0.1 g.

2.4.3 In-situ observations at elevated temperatures

In-situ microstructure observation of the extruded CNT/Al composite was carried out by high-temperature laser-scanning confocal microscopy (LSCM) [10]. The sample was heated up to 650^{o}C with a heating-up speed of 1.5 $^{o}C \cdot min^{-1}$ in Ar gas atmosphere. The OM image was manually taken during the in-situ observation process.

2.5 Mechanical properties evaluation

2.5.1 Hardness test

Room temperature (RT) hardness of processed materials was measured on polished samples by a micro-Vickers hardness tester (Shimadzu: HMV-2T) with an applied load of 0.245 N and hold time of 15 s. The average value obtained from 20 indentations at different positions.

2.5.2 Tensile test

RT tensile test is performed using a universal testing machine (Autograph AG-X 50 KN, Shimadzu) under a strain rate of 5×10^{-4} s^{-1}. The extruded rods with 7 mm diameter were machined into tensile specimen bars of 3.0 mm in diameter and 15 mm in gauge length according to ASTM E8M standard [11], as shown in **Figure 2-7**. The average tested result of

three tensile specimens for each material and their processing conditions were reported. The fractured surfaces of tensile tested samples are also investigated using FE-SEM.

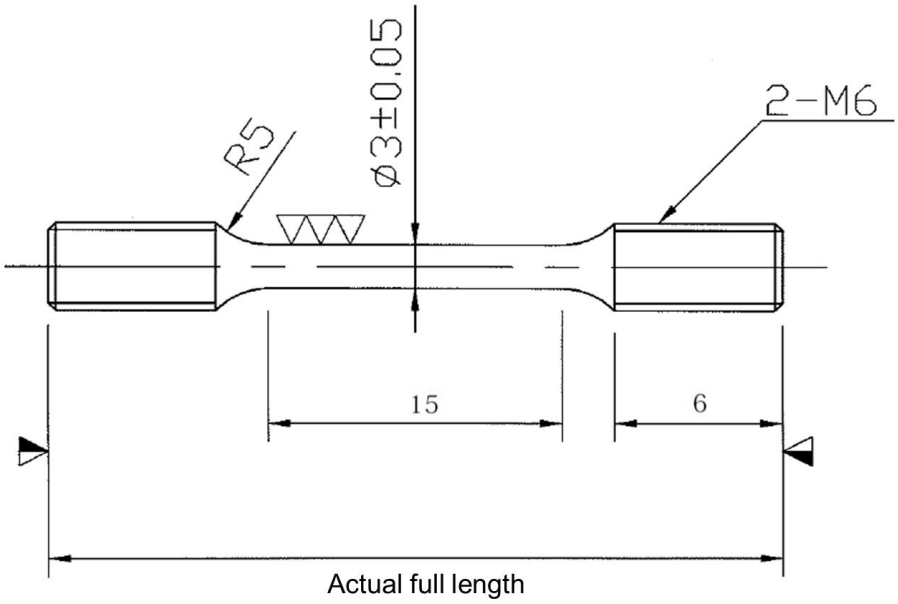

Figure 2-7. Manufacturing drawing of tensile specimen.

2.5.3 In-situ tensile test

The RT in-situ tensile test was performed by operating the tensile stage with a CNT/Al sample inside the FE-SEM chamber as shown in **Figure 2-8**. The tensile specimen was machined from the extruded rod into a flat dumbbell shape with gauge length of 10 mm, width of 2 mm and thickness of 1 mm (inset of Figure 2-8). The sample was placed into the two clamping heads of the tensile unit, and then loaded with a tensile speed of 5 μm/s. As the tensile test was manually paused during the tensile test, the displacement was sustained and high-quality SEM photos were captured. Tensile loading was then restarted to the next pause point until the sample fractured.

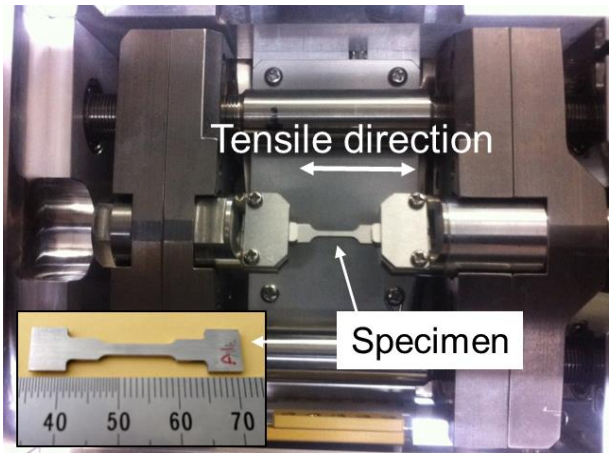

Figure 2-8. In-situ tensile stage with tensile specimen installed in FE-SEM equipment.

References

[1] Pierson HO. Handbook of carbon, graphite, diamonds and fullerenes: processing, properties and applications: William Andrew; 2012.
[2] Peng B, Locascio M, Zapol P, Li S, Mielke SL, Schatz GC, et al. Measurements of near-ultimate strength for multiwalled carbon nanotubes and irradiation-induced crosslinking improvements. Nature nanotechnology 2008;3:626-31.
[3] Byrne EM, McCarthy MA, Xia Z, Curtin WA. Multiwall Nanotubes Can Be Stronger than Single Wall Nanotubes and Implications for Nanocomposite Design. Physical Review Letters 2009;103.
[4] Pantano A, M. Parks D, Boyce MC. Mechanics of deformation of single- and multi-wall carbon nanotubes. Journal of the Mechanics and Physics of Solids 2004;52:789-821.
[5] Kim SW, Kim T, Kim YS, Choi HS, Lim HJ, Yang SJ, et al. Surface modifications for the effective dispersion of carbon nanotubes in solvents and polymers. Carbon 2012;50:3-33.
[6] Barman SN, Pan D, Vosgueritchian M, Zoombelt AP, Galli G, Bao Z. Dispersion of single walled carbon nanotubes in amidine solvents. Nanotechnology 2012;23:344011.
[7] Fugetsu B, Han W, Endo N, Kamiya Y, Okuhara T. Disassembling Single-walled Carbon Nanotube Bundles by Dipole/Dipole Electrostatic Interactions. Chemistry Letters 2005;34:1218-9.
[8] Kondoh K, Threrujirapapong T, Imai H, Umeda J, Fugetsu B. Characteristics of powder metallurgy pure titanium matrix composite reinforced with multi-wall carbon nanotubes. Composites Science and Technology 2009;69:1077-81.
[9] Kondoh K, Fukuda H, Umeda J, Imai H, Fugetsu B. Microstructural and mechanical behavior of multi-walled carbon nanotubes reinforced Al–Mg–Si alloy composites in aging treatment. Carbon 2014;72:15-21.
[10] Terasaki H, Komizo Y-i. Morphology and crystallography of bainite transformation in a single prior-austenite grain of low-carbon steel. Metallurgical and Materials Transactions A 2013;44:2683-9.
[11] Testing ASf, Materials. ASTM designation E 8-00 Standard Test Methods for Tension Testing of Metallic Materials. ASTM; 2000.

Chapter 3

Solution Ball Milling Process for Homogeneous Carbon Nanotube Dispersion in Al Matrix Composites

In this chapter, a novel process named solution ball milling (SBM) was developed for obtaining homogenous carbon nanotube (CNT) dispersion in Al matrix composites (AMCs). To understand the SBM process, the CNT dispersion quality was investigated, and compared with those of the conventional approaches in the CNT-Al composite system using the same starting materials and similar milling conditions. The dispersion quality of CNTs in CNT-Al powder mixtures was characterized by the morphology and content of CNTs. Possible remained surfactants after the coating processes were examined by combination of microscopic observations and energy dispersive spectrums. The change of crystal structures of CNTs induced by the dispersion processes was investigated by the Raman analysis. Based on the results, the status of the CNT-dispersion methods in the CNT-Al system, including the conventional approaches and some newly developed processes, were reviewed and compared with the present SBM process. The merits and demerits or limitations of the methods were further described and discussed.

Since the properties of CNT/Al composites were greatly dependent on the dispersion quality of CNTs, the composite bulks were fabricated by consolidating the powder mixtures dispersed by the SBM process. The appearance of the processed materials was described. The strength improvement in CNT/Al composites induced by the CNT dispersoid was characterized by hardness and tensile tests. To understand the strengthening mechanisms in composites, the effect of CNT additions on the microstructures of Al matrix was clarified. The grain information including grain size, misorientation angle of grain boundary and texture, phase compositions and fracture morphologies of pure Al and CNT/Al composite were characterized. Possible carbide phases in CNT/Al composites were also examined. Based on the observations, the strengthening effect induced by CNTs was discussed using the generalized shear-lag model. The relation between the strengthening efficiency and the dispersed CNT content was set up and compared with the experimental values.

3.1 Traditional methods to disperse carbon nanotubes

3.1.1 Solution coating processes

Figure 3-1 shows the dispersion quality of CNTs on the Al powder surface by the traditional solution coating (SC) processes. As raw Al powders with round shapes were used, individual CNTs were hardly observed on the raw Al powder surface. There existed large CNT clusters, as shown in Figure 3-1a, especially in the junction area between Al powder particles (inset of Figure 3-1a). During coating, CNTs were initially dispersed in the solution and then some might be attached to the powder surface [1]. However, if the CNT absorbing ability of Al powder was low and the chemical attractive force between CNT and Al was weak, CNT re-agglomeration phenomenon might happen during the vaporization of the liquid solution under the surface tension [2]. These results suggested the ineffective absorbing of CNTs by raw Al powder through the SC process.

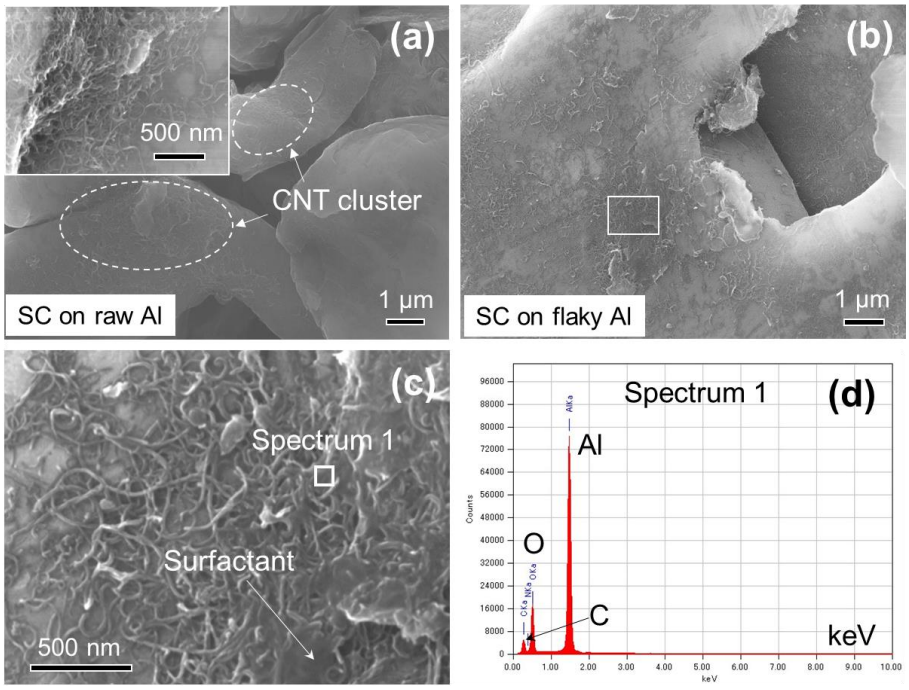

Figure 3-1. Morphologies of CNT distribution on raw Al surface (a) and flaky Al surface (b,c) by solution coating (SC). (c) is the local view in (b), and (d) shows EDS analysis of area in (c).

Figure 3-1b shows the CNT distribution on flaky Al surface by the same SC process. Compared with raw Al powder, CNT dispersion quality was much improved on flaky powders. One thin CNT layer covered the flattened Al surface. The improvement of CNT dispersion was attributed to the increased compatibilities of morphology and size between micro-sized Al powder and nano-sized CNTs by applying the flaky strategy [3, 4]. However, CNTs still overlapped and entangled together with the remained surfactant as shown in Figure 3-1c. The EDS analysis (Figure 3-1d) with a strong O K peak provided evidence of the remained surfactant. In Jiang's study [5], homogeneous CNT dispersion was achieved using the SC process on flaky Al. The difference in their coating process from this study was that surface-modifications of both CNTs and Al powders were applied. Therefore, the CNTs were dispersed from a thin layer to single individuals in Jiang's study.

3.1.2 Mechanical ball milling processes

Figure 3-2 shows the CNT dispersion quality on the raw Al powder surface by the low-energy blending (LEB) process. It was observed that little morphology change happened to the Al powders, resulted from the low energy applied onto the powders by milling balls. Small Al powders and CNT clusters were attached on the surface of large powders (Figure 3-2a). From the high-magnification view (Figure 3-2b), flattened CNT clusters were clearly observed. It suggested that the low-energy milling ball was able to break up the large CNT agglomerates (in diameter of ~500 μm, Figure 2-3a) to cluster layers. However, fine and long CNTs were still entangled together. It was unable to produce individually dispersed CNTs by the present LEB process.

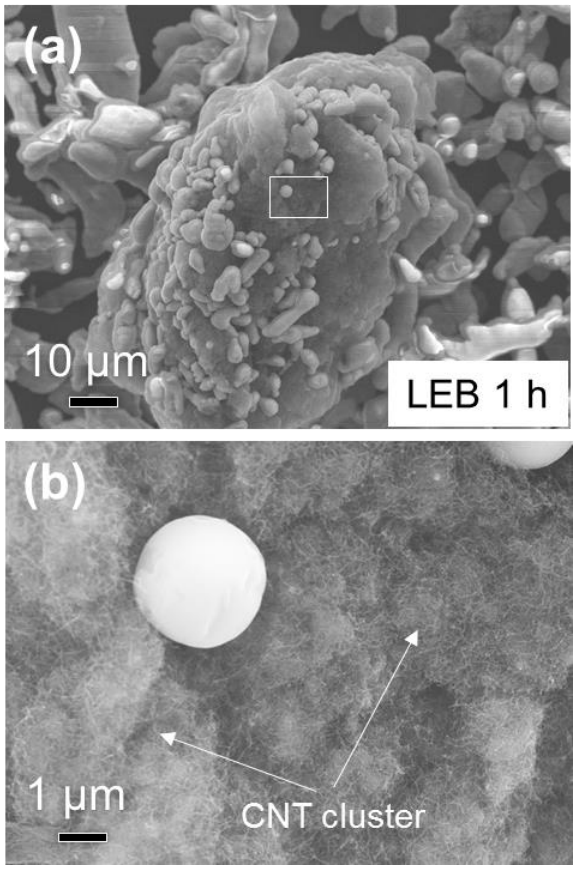

Figure 3-2. CNT dispersion in CNT-Al powder mixture processed by low-energy blending (LEB) process at different magnifications. CNT clusters are shown in (b).

The CNT dispersion effect on Al powder surface through the high energy ball milling (HEBM) process is shown in **Figure 3-3**. Compared with the LEB process, the energy level was greatly increased owing to several factors. One is the comparably large ball to powder massive ratio (5:1) in HEBM. Another factor is that the pot used for HEBM is made of hard ZrO_2 ceramic, while the LEB pot is plastic. Therefore, after HEBM for only 60 min, Al powders changed to a flaky morphology (Figure 3-3a) under the shear or compact force of high-energy milling balls. However, in the LEB process, there was no obvious shape change of Al powders (Figure 3-2). Flaky Al powders or Al flakes have been usually observed in other studies using HEBM process under the assistant effect of stearic acid [6-8].

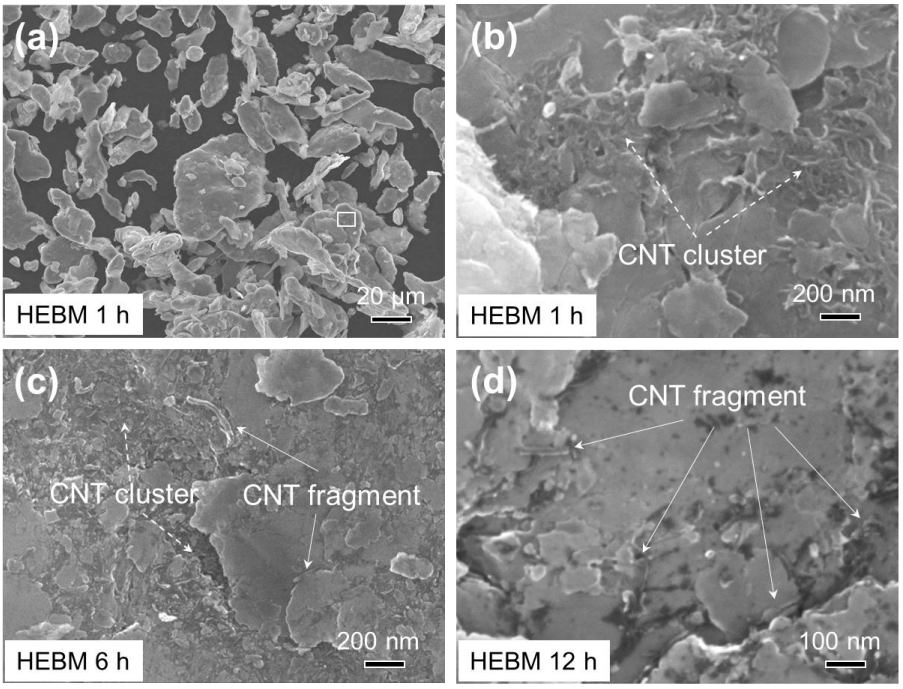

Figure 3-3. CNT dispersion in CNT-Al powder mixture processed by high-energy ball milling (HEBM) process with different milling times. (a,b) 1 h. (c) 6 h. (d) 12 h. (b) shows box area in (a).

From the high-magnification view (Figure 3-3b), CNT dispersion was greatly improved, compared with the starting state (Figure 3-3a) and that dispersed by LEB process (Figure 3-2b). CNTs still, however, existed as flattened clusters under the impact of milling balls. After 6 h milling, CNT clusters evolved to thin and small layers, as shown in Figure 3-3c. Individual CNT fragments were also occasionally observed. After further milling for 12 h (Figure 3-3d), CNT clusters were completely broken up and became individual CNT fragments distributing on the powder surface. However, it is clearly observed that CNTs became shortened and many exhibited a short length of ~100 nm, suggesting severe structure change of CNTs.

3.2 Carbon nanotube dispersion in solution ball milling process

3.2.1 Integration methodology

As demonstrated in Section 1.4.2.1, there are multiple challenges in the CNT dispersion in Al matrix composites. The improvement and difficulty in obtaining

homogeneous CNT dispersion has been described in Section 3.1 using various traditional methods. These methods were originated from the ideas to overcome each dispersion problems as shown in **Figure 3-4**.

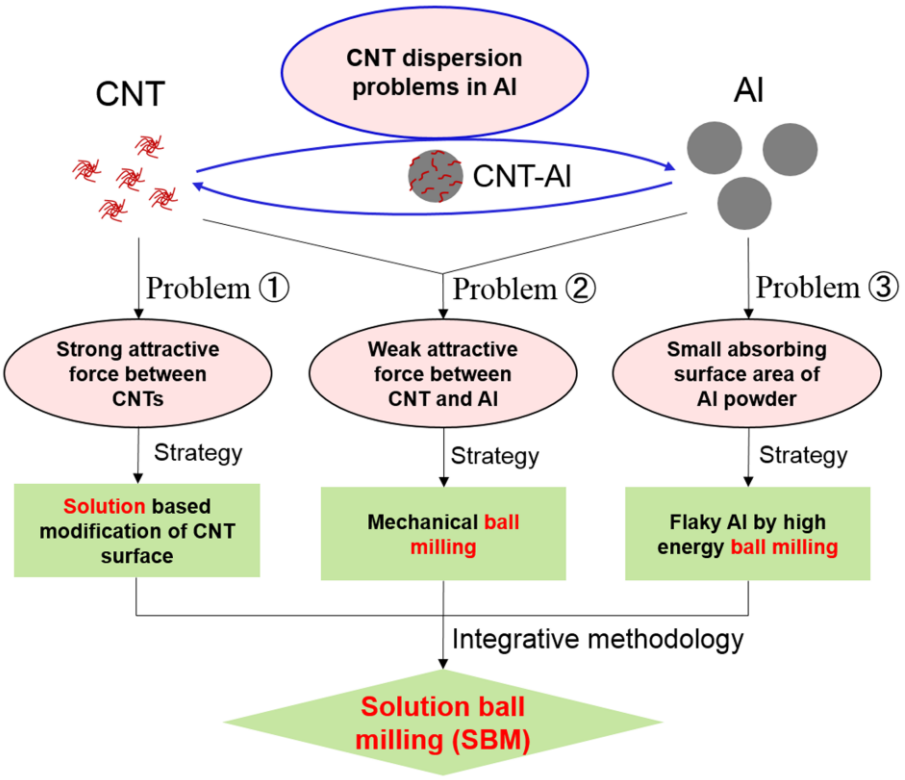

Figure 3-4. Solution ball milling (SBM) process is a key to resolve the problems in CNT dispersion in Al matrix composite from an integrative methodology of present studies.

To deal with the problem of low attractive force between Al and CNTs, chemical methods, or solution-based surface modification of CNTs, were used to enhance their chemical compatibility to medium aqueous [9], organic solutions [10] or polymers [10-12]. Homogeneously CNT-dispersed solution could be obtained without much difficulty. The popular solution coating processes [1, 2, 5, 13] was based on this strategy.

A following problem is the weak attractive force between CNTs and Al, resulted from their incompatibility of zeta potential [14]. Moreover, weak CNT-Al bonding might result in re-aggregation of CNTs during dispersing, post drying or consolidating processes [2]. Insufficient CNT dispersion in coating process was also observed in Section 3.1.1. This problem was resolved in the mechanical ball milling process by strongly attaching CNTs on

Al powders under the external mechanical force. However, the energy input was difficult to control for balancing the CNT dispersion and structure damage. Good CNT dispersion could be achieved in HEBM for a long time of 12 h, as shown in Figure 3-3d. However, severe CNT structure damages, such as CNT shortening and crystal-structure change, seemed evitable, as revealed in Section 3.1.2.

The final problem is that the specific surface area of micro-sized Al powders is small for absorbing CNTs. As revealed in Section 3.1.2, flaky Al particles with greatly improved surface areas could be prepared using HEBM processes by preventing cold-welding of Al powders, which agreed with some previous studies [4, 15]. However, owing to the ignorance of the strong attractive force between CNTs, HEBM process also confronted the severe CNT damage for dispersing CNTs [13, 16]. Accordingly, homogeneous CNT dispersion with minor or small structure change in composites is difficult to obtain from the conventional methods based on a single-aspect strategy. From the viewpoint of integrative methodology, a simple but effective solution ball milling (SBM) process integrating the present strategies into an organic unity is put forward to simultaneously resolve the three problems in CNT dispersion. The characteristics of this method will be shown in the following parts.

3.2.2 Morphology of powder mixtures

Figure 3-5 shows the morphologies of the Al-CNT powder mixture dispersed by the SBM process as starting CNT content is 0.5 wt.%. Similar to HEBM, the SBM process also produced flaky Al (Figure 3-5a and b), because the solution acted as a process control agent to prevent cold-welding of Al powders. From the local views, it is observed that CNTs are homogeneously dispersed on all the surface of Al flakes, including both small ones (Figure 3-5c) and large ones (Figure 3-5d). It was also observed that CNTs were strongly attached to the Al powder surface or underlying CNTs by the mechanical force of milling balls. Moreover, little surfactant was observed on the Al surface due to the observed weak O K peak in the EDS analysis (inset of Figure 3-5c). Therefore, the absorbed CNT weight content (ω_{CNT}) could be regarded equal to the measured carbon element concentration of 0.39 wt.%. The volume content of CNTs (V_{CNT}) could then be estimated as 0.51 vol.% based on the rule of mixture ($V_{CNT}=\sim 1.3\omega_{CNT}$) [17] using CNT density of 2.0 g cm^{-3} and Al of 2.7 g cm^{-3}.

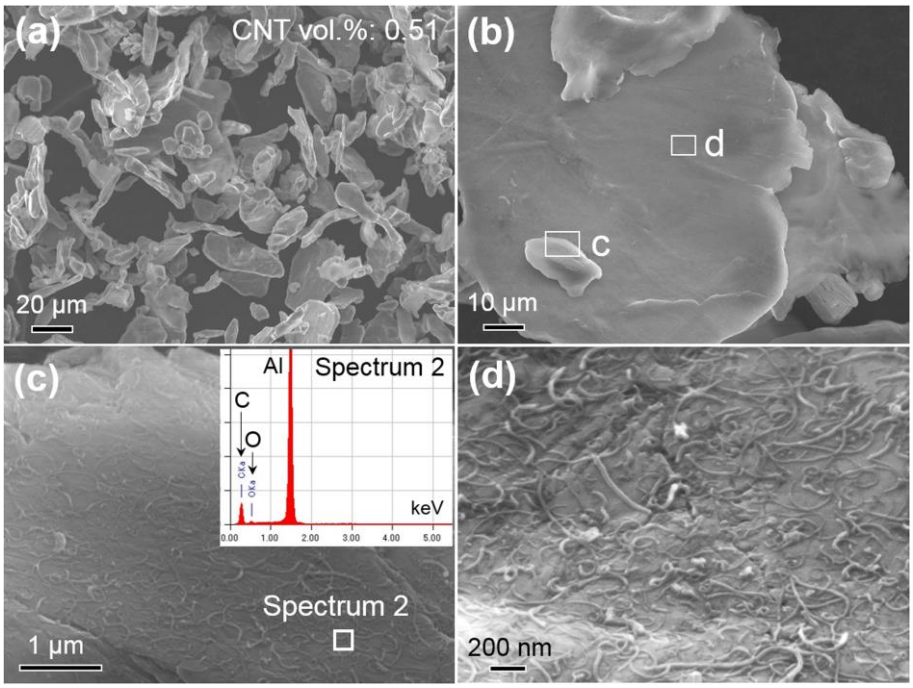

Figure 3-5. Morphologies of CNT-Al powder mixture containing 0.51 vol.% CNTs using SBM process at different positions and magnifications. Inset of (c) shows EDS analysis of selected area.

As the starting CNT content is increased to 1 wt.% (1.3 vol.%), the absorbed CNT content was measured as 0.88 vol.%. The morphology of the powder mixture is shown in **Figure 3-6**. On the surface of a typical Al flake (Figure 3-6a and b), most of the surface was well covered with un-bundled CNTs. Compared with 0.51CNT powder (Figure 3-5), the distribution density of CNTs was increased on this 0.88CNT powder, agreeing with the increased amount of absorbed CNTs. Some fine CNT clusters with size of ~200 nm were observed as arrows indicated in Figure 3-6a and b. It suggested that the Al flakes produced under present conditions might have reached the limit of CNT absorbing ability. Appling CNT with a high content, such as 2 wt.%, would result in serious CNT agglomerations in the present SBM conditions. Homogeneously dispersed CNTs with high contents could be achieved by decreasing the thickness of Al flakes via adjusting milling conditions, as suggested by the study of Jiang et al. [5].

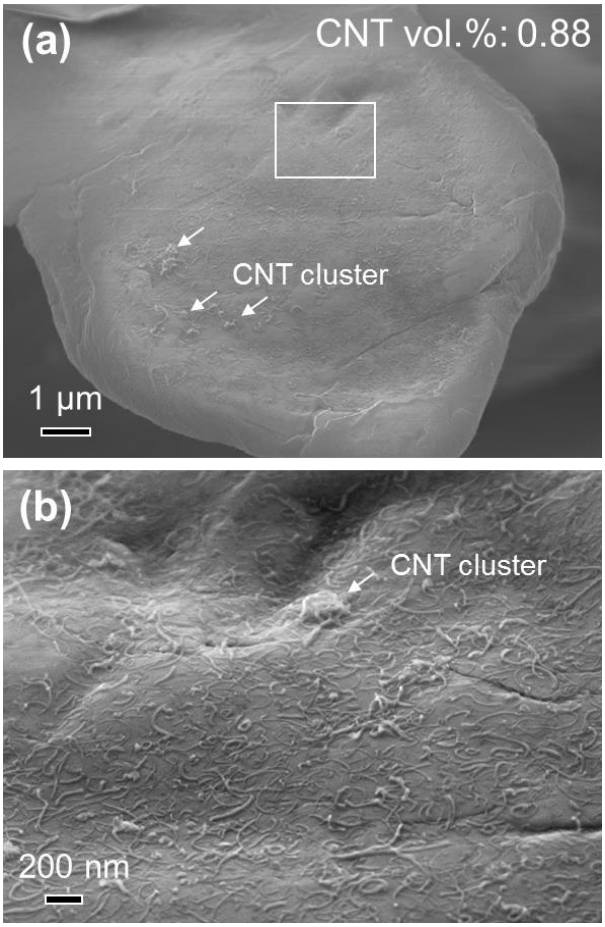

Figure 3-6. Morphology of CNT-Al powder mixture containing 0.88 vol.% CNTs using SBM process at different magnifications.

Moreover, similar to 0.51 vol.% CNT powder (Figure 3-5), CNTs were also strongly attached to the surface of Al flakes with little surfactant remains in 0.88 vol.% CNT powder. It was measured that the average diameter and length of CNTs dispersed by SBM was 12.1 nm and 652 nm, respectively, showing an aspect ratio of 54. The small reduction of aspect ratio (from 58 to 54) suggested that the SBM process had no obvious effect on the CNT size from the raw to dispersed state. A large aspect ratio was significant for achieving high load transfer strengthening in CNT/Al composites [18, 19].

The dispersion quality can be also reflected on the appearance of extruded materials because a weak bonding between reinforcement agglomerations and Al matrix resulted in cracks under shear force during extrusion [19]. The appearance of extruded rods is shown in **Figure 3-7**. With the pure Al, the surface condition was good because it showed a smooth

shining color without cracks (Figure 3-7a). As CNTs were added in the SC process, the extruded rod had ring-like scratches on the surface, suggesting that the surface condition was degraded. The phenomenon was probably due to the existence of large CNT clusters in the sample so that the CNT-Al bonding interface was cracked during extrusion. As the CNT dispersion quality was improved in the CNT/Al composite rod processed by SC on flaky Al, the scratching phenomenon was inhibited to some extent (Figure 3-7a). With the extruded samples processed by SBM, the two composites exhibited similar appearance to the pure Al processed by SBM (Figure 3-7b), indicating the homogeneous CNT dispersion in composites.

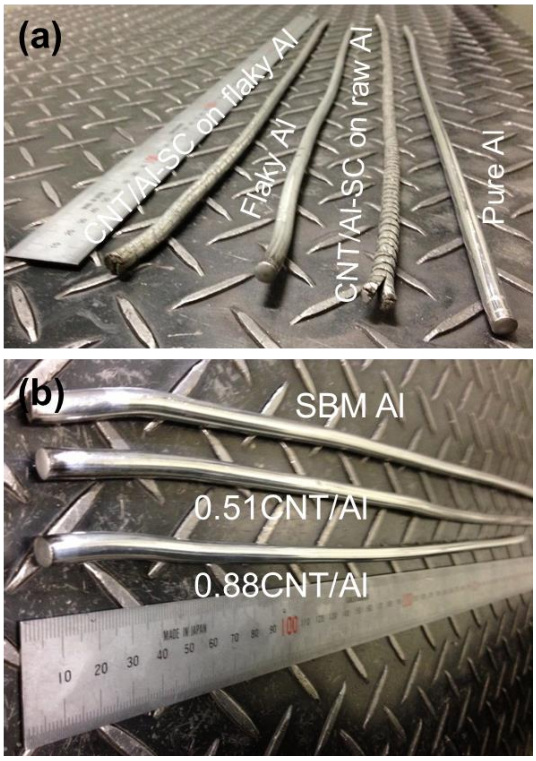

Figure 3-7. Appearance of extruded rods processed by solution coating (a) and solution ball milling (b).

3.3 Microstructural characteristics

3.3.1 Grain size and texture

Figure 3-8 shows the grain information, including grain orientation and rotation angles of grain boundaries (RAGBs), grain orientation and average grain size (GS) of pure Al and the 0.88CNT/Al processed by SBM. From the image quality (IQ) figures (Figure 3-8a,

c, and e), the high angle grain boundaries (HAGBs) with angles larger than 15° were dominant in the all materials. However, as CNTs were added, the fraction of low angle grain boundaries (LAGBs) (<15°) was noticeably increased (Figure 3-8e). It suggested that CNTs might show effect on the growth and rotation of matrix grains during p8rocessing. As seen from the inverse pole figures (IPFs) (Figure 3-8b, e, and f), <111> oriented grains were found to be dominant along the extrusion direction in all samples.

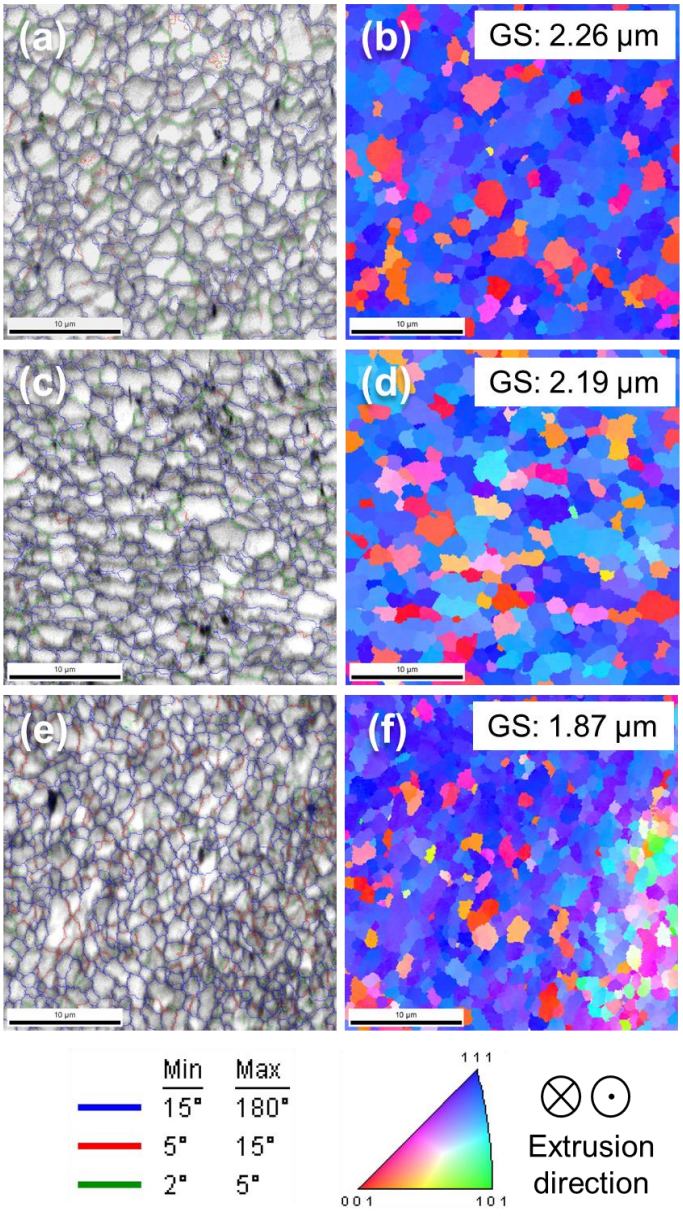

Figure 3-8. Grain information of pure Al (a,b), SBM Al (c,d) and 0.88CNT/Al (e,f). (a,c,e) Image quality figures with grain boundary information. (b,d,f) Inverse pole figures (IPFs).

Moreover, the pure Al and SBM showed similar average GS of ~2.2 μm, reasonably owing to the low-energy input on Al powder particles during the SBM process. With the composite containing 0.88 vol.% CNTs (Figure 3-8f), the average GS was decreased to 1.87 μm. It suggested that CNTs had pinning effects on Al grain growth during consolidation in AMCs. **Figure 3-9** typically shows a fine Al grain near a CNT in 0.88CNT/Al composite observed by TEM. The Al phase can be identified by SAD patterns as shown in the inset of Figure 3-9b.

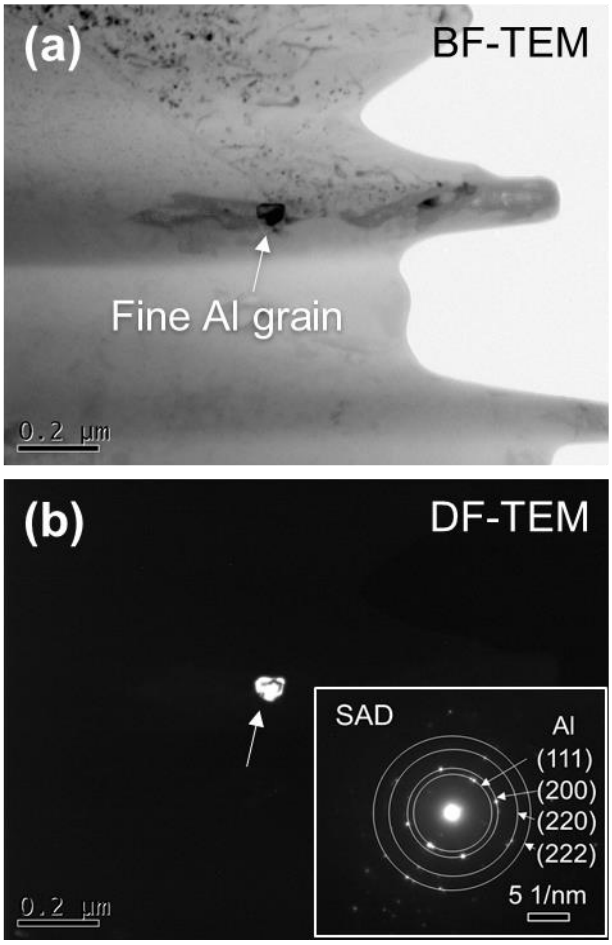

Figure 3-9. A typical fine Al grain in 0.88CNT/Al composite observed by TEM. (a) BF image. (b) DF image. Inset of (b) shows the SAD patterns.

3.3.2 Phase compositions

Figure 3-10 shows the X-ray diffraction (XRD) patterns of pure Al, SBM Al and CNT/Al composites. From the normalized patterns (Figure 3-10a), the <111> planes were

found to be dominant along the extrusion direction. Both the dispersion process and CNT addition had little effect on the grain orientations. It agreed well with EBSD results as shown in Figure 3-8. To determine the possibly formed Al_4C_3 phase, the patterns of 0.88CNT/Al were magnified as shown in Figure 3-10b. It is seen that there is no possible Al_4C_3 peak at 36.0 °, 43.6 ° and 55.2 ° (ICDD Card No. 35-0799).

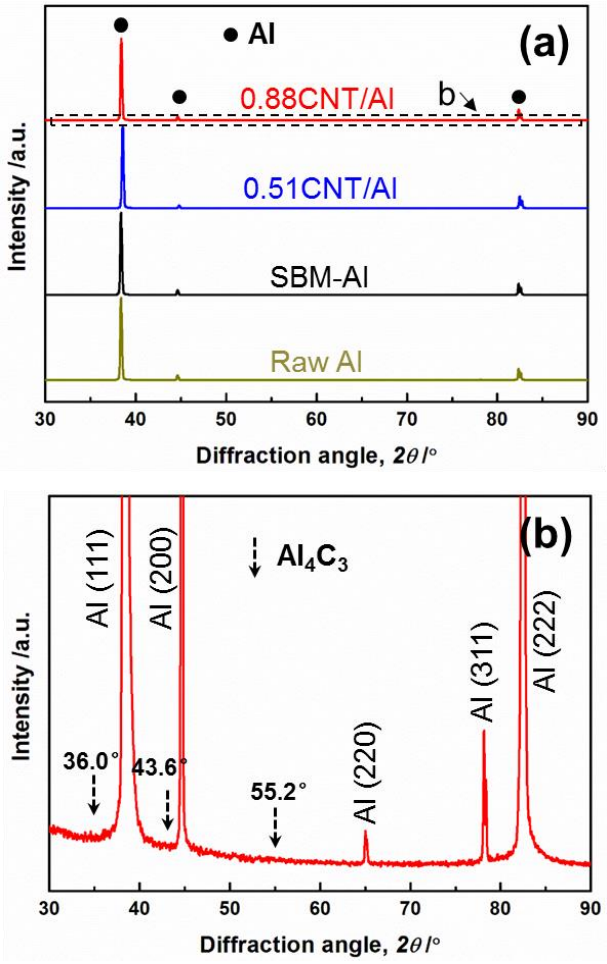

Figure 3-10. XRD patterns of processed materials. (a) Normalized patterns with same intensity of the (111) peak. (b) Magnified patterns of 0.88CNT/Al.

From the TEM observation, Al_4C_3 phases were, however, occasionally observed as typically shown in **Figure 3-11**. The Al_4C_3 compounds showed a rod-like shape in an ultra-fine size with a diameter of ~50 nm (Figure 3-11a). The Al_4C_3 phase can be clearly identified by the SAD patterns in Figure 3-11b. The fully physical contact between dispersed CNTs and Al in the SBM process (Figure 3-5 and Figure 3-6) might be helpful to achieve an ideal

reactive interface via the combination with SPS and hot-extrusion. Therefore, the chemical reaction between Al matrix and CNTs, especially damaged CNTs [20], was then greatly promoted. From the BF-TEM image (Figure 3-11a) and corresponding SAD patterns (Figure 3-11b), the nanorod were identified as single-crystal Al_4C_3. Interestingly, the in-situ formed Al_4C_3 nanorods had basal planes (001) of the hexagonal crystal parallel to the axis direction. Since CNT has the same crystal characteristic (Figure 2-3d), it suggested that Al_4C_3 nanorods might be *in situ* formed by the template reaction of CNT and matrix Al.

The in-situ Al_4C_3 nanorods were reported helpful to increase the strength of CNT/Al composites [21], probably due to their fine size and the load transfer enhancement from damaged CNTs to the mono-crystal nanorods. Combination of XRD and TEM analysis indicated the small quantity of Al_4C_3 phases.

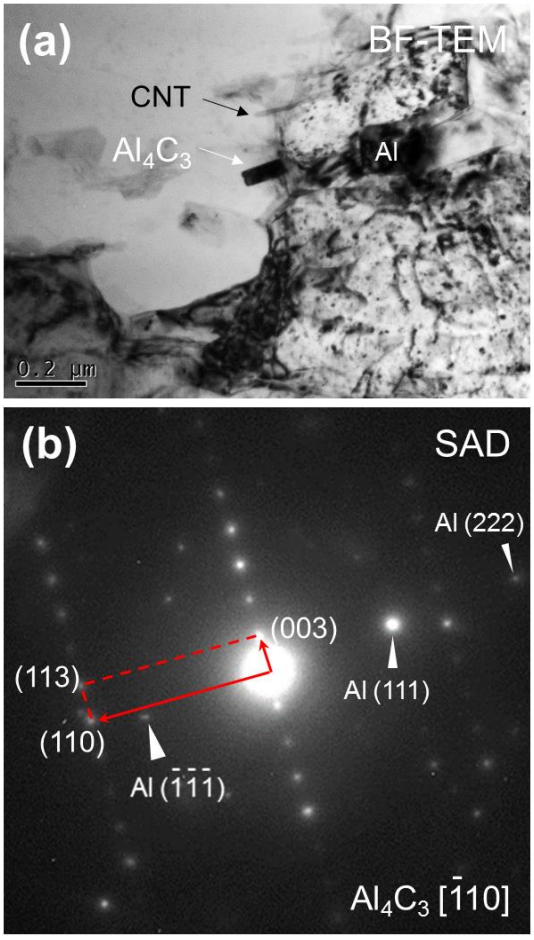

Figure 3-11. BF-TEM observation (a) and SAD patterns (b) of Al composite reinforced with 0.88CNT.

3.4 Mechanical properties

3.4.1 Tensile properties and hardness

Mechanical properties of CNT-reinforced composites were greatly dependent on the dispersion state of CNTs [17, 22]. Therefore, the strengthening effect of CNT addition in AMCs was also investigated. **Figure 3-12** shows the true tensile stress-strain curves of the processed materials. It was observed that a little increase of tensile strength (UTS) of Al happened from 133 MPa of pure Al to 140 MPa of SBM-Al, probably because of the small work hardening effect of milling balls on Al matrix in SBM process. Compared with the reference SBM-Al, the composites consolidated from 0.51CNT and 0.88CNT powders were noticeably increased (Fig. 8a) to 160 MPa and 171 MPa, respectively. Moreover, the CNT/Al composites still had a good plasticity with elongation of ~20%. The hardness of Hv0.025 was measured as 48.2±0.7 MPa, 52.1±1.2 MPa, 57.8±1.1 MPa and 63.0±1.5 MPa for pure Al, SBM Al, 0.51CNT/Al and 0.88CNT/Al. It also showed noticeable reinforcing effect by adding CNTs.

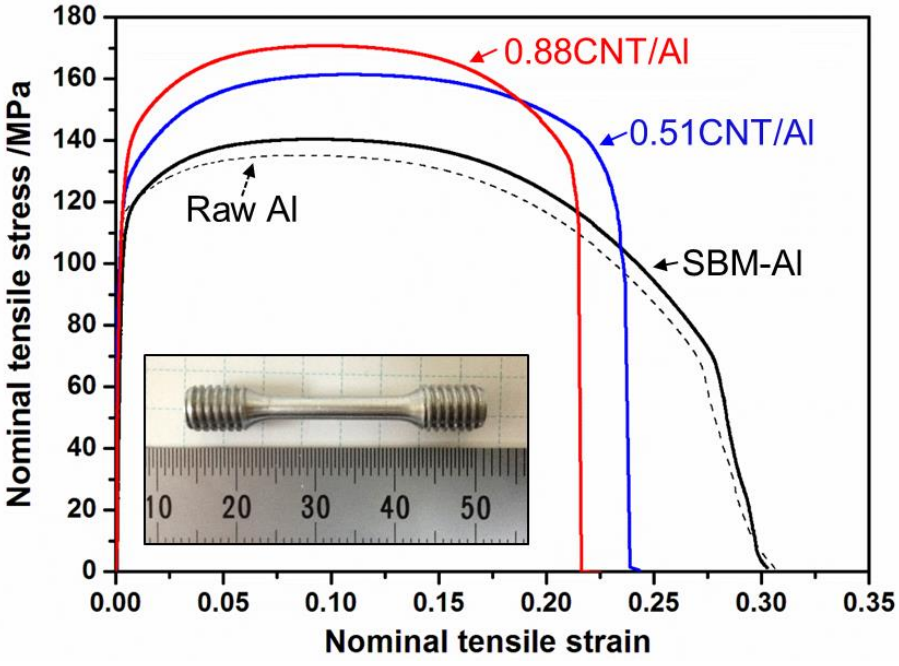

Figure 3-12. Nominal tensile stress-strain curves of processed materials. Inset shows appearance of a tensile specimen.

3.4.2 Reinforcing effect of carbon nanotubes

Figure 3-13 shows the fracture morphology of pure Al materials without CNTs after the tensile test. Both raw Al and SBM Al exhibited a highly ductile fracture mode, with large area reduction ratio (ARA) (Figure 3-13a and c) and hierarchical dimples (Figure 3-13b and d). The necking or fracture area of raw Al and SBM were reduced from 3 mm to ~1 mm, suggesting large ARA values of ~67%. However, CNT/Al composites (**Figure 3-14**) showed distinct fracture morphologies compared with pure Al. Necking phenomenon was not obvious during the tensile test, and ARA values were greatly reduced. Moreover, the dimple size became much more uniform (Figure 3-14a and c) than that of pure Al materials. These facts agreed with the observed decrease of tensile elongation of CNT/Al composites (Figure 3-11).

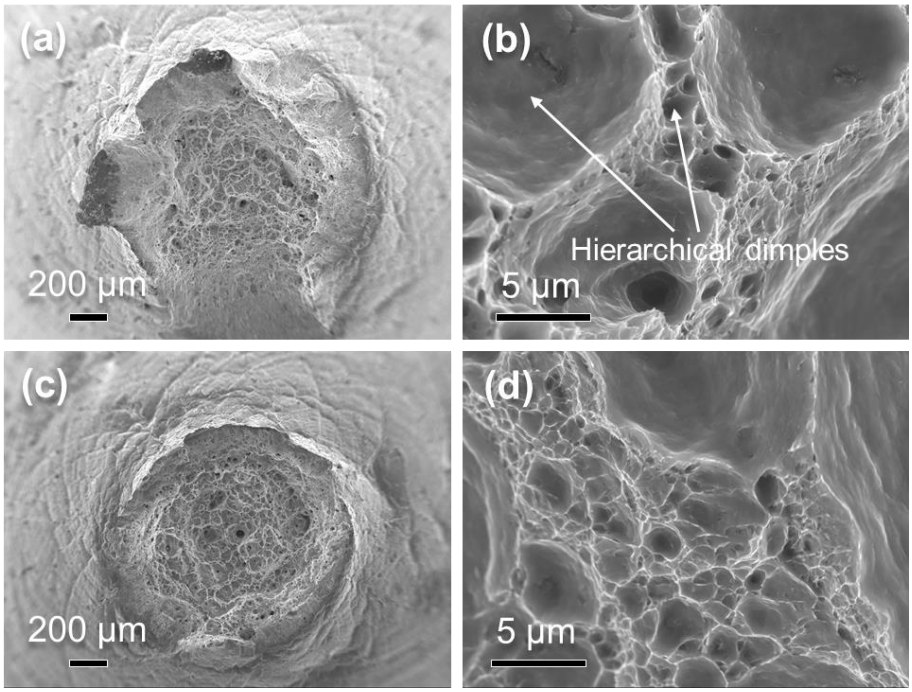

Figure 3-13. Fracture morphology of pure Al (a,b) and SBM Al (c,d) specimen at different magnifications.

Another difference is that pulled-out CNTs were observed on the fracture surface of CNT/Al composites (Figure 3-14b and d), suggesting the effective load transfer from matrix to CNTs during tensile failure. The high load transfer efficiency in CNT/Al composites were

resulted from a strong interfacial strength between CNTs and Al matrix [23]. The strong interfacial bonding was originated from the effective physical contact between CNTs and Al matrix.

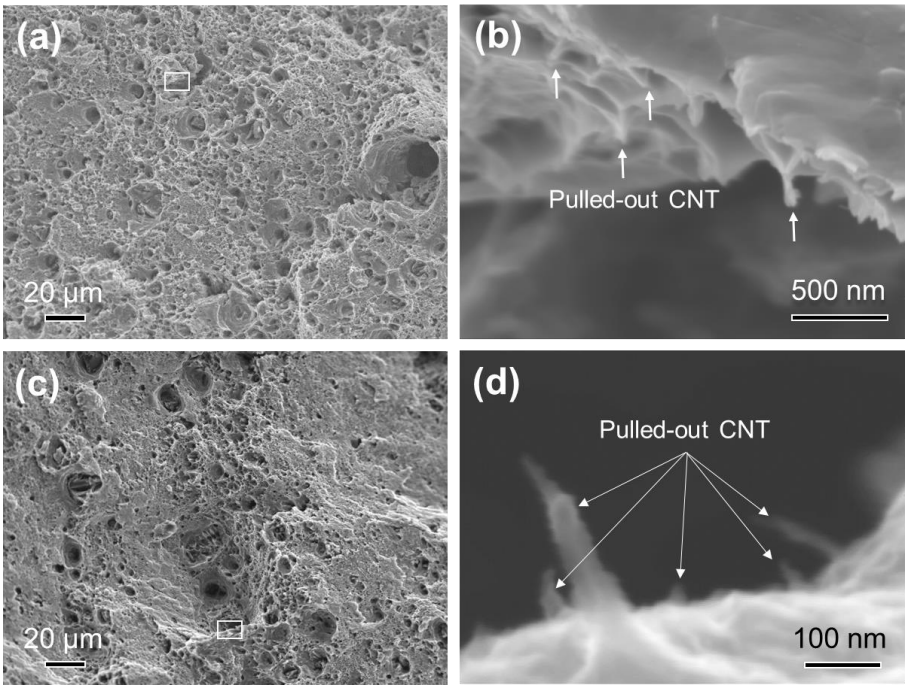

Figure 3-14. Fracture morphology of 0.51CNT/Al (a,b) and 0.88CNT/Al (c,d) specimens at different magnifications.

The matrix could be strengthened by CNTs in the possible mechanisms of grain refining and load transfer strengthening [24, 25]. The average grain size of SBM-Al, 0.51CNT/Al and 0.88CNT/Al materials were measured as similar values of ~2 μm (Figure 3-8). It suggested that the grain refining contributed little (~1 MPa) to the strength improvement in AMCs according to Hall-Petch formula [24]. Considering the load transfer strengthening of CNTs, the composite strength (σ_c) can be obtained from the generalized shear-lag model [26] and expressed as:

$$\sigma_c = \sigma_m + \frac{S}{2} V \sigma_m \qquad \text{(Eq. 3-1)}$$

where σ_m was the matrix strength, and V and S are the volume fraction and aspect ratio of CNTs, respectively. The reinforcing effect (r) of CNTs, or the relative strength improvement of CNT/Al composites, can be expressed as:

$$r = \frac{\sigma_c - \sigma_m}{\sigma_m} \quad \text{(Eq. 3-2)}$$

By introducing Eq. 3-1 to Eq. 3-2, r can be expressed as:

$$r = \frac{S}{2} \cdot V . \quad \text{(Eq. 3-3)}$$

Since S was estimated as 53 for CNTs in SBM process from Figure 3-5 and 6, the relation between predicted r from Eq. 3-3 and measured r from Eq. 3-2 are shown in **Figure 3-15**. The strengthening efficiency (R), or the slope of r-V line, was half of S of CNTs, which was 26.5 for SBM composites. It can be seen that yield strength (0.2%YS), UTS and hardness of CNT/Al composites agreed well with the predictions (Figure 3-15). It suggested that the high strengthening potential of CNTs has been almost achieved through the load transfer mechanism by the SBM process.

R of CNT/Al composites processed by SBM showed the similar value of Flake PM, and it was far larger than R of 7.5 by HEBM, which was reasonably due to the small S of CNT fragments in HEBM [27]. However, UTS of the present 0.88CNT/Al composite (192 MPa) was still low compared with the CNT/Al composites processed by HEBM (345-366 MPa) [28]. It was because σ_c was proportional to σ_m (Eq. 3-1), and σ_m of CNT/Al composites by SBM (140 MPa) was far lower than that by HEBM (284-377 MPa) [28]. CNT/Al composites with excellent mechanical properties could be expected by applying strong Al matrix with ultra-fined grains or alloy-strengthening elements in the present SBM process.

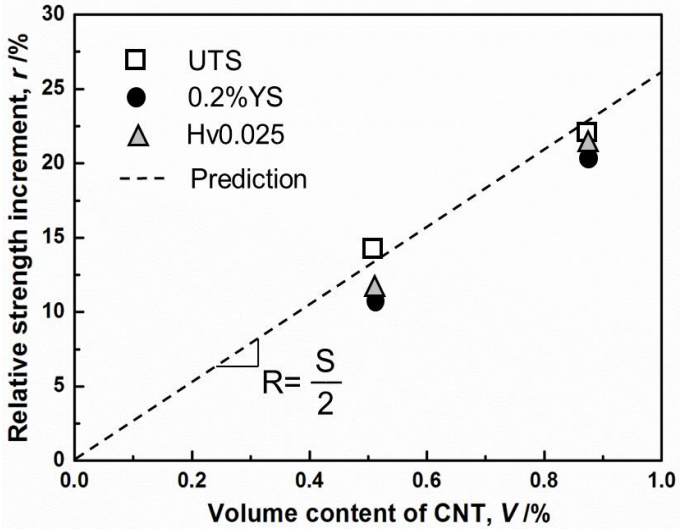

Figure 3-15. Increment of mechanical properties of CNT/Al composites as a function of CNT volume content.

3.5 Characteristics of different dispersion methods

The structural damages of CNTs were another significant aspects to evaluate the dispersion methods. Raman spectra has been used for characterize the crystal-structure change of CNTs after processing in many studies [28-32]. The peaks at ~1350 cm^{-1} and ~1572 cm^{-1} correspond to a typical D-band (defect) and G-band (graphite), respectively. The relative intensity between the two peaks (I_D/I_G) is known to provide information about the quality of the internal CNTs. A higher value of I_D/I_G suggests a higher defect density in CNTs.

Figure 3-16 shows the Raman spectra of processed materials using different dispersing methods with starting CNT contents of 1.3 vol.%. The value of I_D/I_G of raw CNT powder was 1.19. SC powder showed the same value, and it suggested a minor CNT change of the dispersion process by coating. However, I_D/I_G was respectively increased to 1.46 and 1.49 of HEBM 1 h powder and HEBM 12 h powder, which suggested the noticeable structure change of CNTs in HEBM process. I_D/I_G of SBM powder was 1.33, much smaller than that of HEBM powders. After consolidation, I_D/I_G of CNT in SBM was almost kept the same value, which suggested the minor effect of consolidating on the structure of remained CNTs. A peak at ~830 cm^{-1}, which might be the Al_4C_3 peak from the study of Sun et al. [33],

was also detected. It suggested the probable formation of Al_4C_3 phase in the present consolidation conditions.

Moreover, it was observed that there was a peak shift of G-band for HEBM powders and the SBM-consolidated materials, which agreed with the observations in the HEBM powder mixture [34]. The peak shift of G-band came from the compressive strain in CNTs induced by a high-velocity impact of balls on CNTs during HEBM. It was noted that the SBM powder showed no peak shift of G-band, because solution acted like a buffer to reduce the impact of high-velocity balls on CNTs. Therefore, from the information on the morphologies (Figure 3-5 and Figure 3-6) and crystal-structure (Figure 3-16) of CNTs, homogeneously dispersed CNTs with a large aspect ratio and small structure change were obtained in Al through the SBM process.

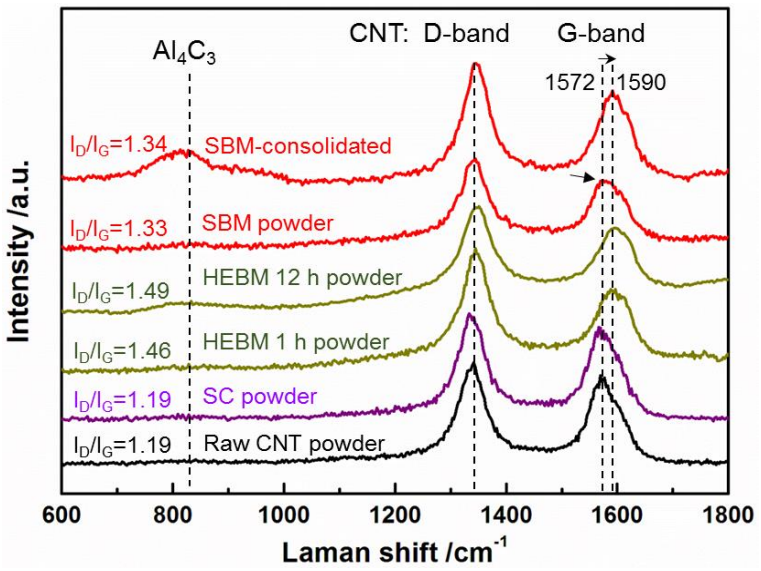

Figure 3-16. Raman spectra of raw CNT powder, solution coating (SC) powder, high energy ball milling (HEBM) Al-CNT powder for 1 h and 12 h, solution ball milling (SBM) powder and SBM-consolidated composite. All starting CNT contents are 1 wt.%. Note that no peak shift of G-band happens to SBM powder.

The characteristics, including the description, dispersion effect, CNT damages, merits and demerits of previous dispersion methods as well as the SBM process were summarized in **Table 3-1**. The conventional SC [1, 13], LEB [35] and HEBM processes [15, 16, 21, 28, 31,

32, 34, 36, 37] were simple processes but difficult to obtain well-dispersed and little-damaged CNTs in AMCs. The results in Section 3.1 also confirmed this point.

Table 3-1. Characteristics of different dispersion methods in CNT-Al system.

Dispersion method	Method description	CNT dispersion and dispersed CNT content	Merits	Demerits or limitations
Solution coating (SC)	Al powders bath in inorganic [9] or organic [1] solutions containing dispersed CNT. Ultrasonic vibration is sometimes used [13].	Large quantity of CNT clusters are observed on dried powder surface.	Simple and fast. Small or minor CNT structure change.	Difficult to obtain well-dispersed CNTs in composites.
Mechanical mixing	Low energy blending (LEB): CNT-Al powders are blended without balls or ball milled with low energy [35].	Small content of CNTs is broken up from clusters. Minor change of Al powder shape.	Simple and low-cost. Small CNT structure change.	Ineffective to get well-dispersed CNTs in composite.
	High energy ball milling (HEBM) without process control agent (PCA): Large BPR and high speed [40].	CNT fragments are dispersed into cold-welded and large-sized Al powders.	Effective to obtain well dispersed CNT. Process is flexible.	Cold-welding degrades the CNT dispersion. Difficult to disperse high-content CNTs.
	HEBM with PCA: milling agents such as solid acid [41], methanol [36], alcohol [27], and polymer [37] are added to assist the milling of CNT and Al powders.	CNT fragments are well-dispersed on flaky powder surface. High content CNTs can be dispersed.	Effective to obtain well dispersed and high-content CNT. Process is flexible.	Severe CNT structure damage and length reduction. Removing of PCA is often required.
In situ grown [38, 39]	Growth of Ni or Co catalyst on Al powers. Growth of CNTs on Al-Ni or Al-Co powders.	Uniform CNT dispersion. CNTs stand and bend on Al surface.	No need to purchase CNTs. High CNT content.	Nanoparticles are introduced in composites. Difficult to obtain high-quality CNTs.
Flake powder metallurgy [3-5]	Flaky Al is first produced. Modify both CNT and Al surface. Al powders bath in aqueous solution with dispersed CNTs.	Homogeneous CNT dispersion on flaky powder surface. Flake thickness affects dispersed CNT content.	Minor CNT structure change and high dispersed CNT content of 2 vol.%.	Alumina were introduced in composites. Removing of PVA is required.
Solution ball milling (SBM) in this study	Combine solution coating, mechanical ball milling and flaky Al preparing into a single step.	Homogeneous CNT dispersion. CNTs strongly stick to flaky Al surface. CNT content is up to 0.88 vol.%.	Simple, flexible and fast. Small CNT damage change. No need heat treatment.	High content CNTs are under exploring.

In-situ grown [38, 39] and flake powder metallurgy (Flake PM) [3-5] were two recently reported methods to disperse CNTs in AMCs. In-situ grown method elaborately

translates the three problems of CNT dispersion shown in Figure 3-4 to an easier task of dispersing catalyst nanoparticles onto Al powder surface. In the Flake PM, the three problems were respectively overcome by modification of CNTs, modification of Al surface, and utilization of Al flakes. Homogeneous CNTs were dispersed on Al surface and contributed to enhanced composite strengths in these two methods. Compared with in-situ grown and Flake PM, the present SBM process was simple, easy to manipulate, and free of introduction of additional phases, because it combined the two conventional simple approaches of SC and HEBM into one unity. More importantly, the shortcomings of individual SC and HEBM were made up for each other.

The solution in SBM, more of a function in decreasing attractive force between CNTs in SC, decreased the force of high-energy milling balls on CNTs. It also acted as a PCA to help produce Al flakes. Therefore, well-dispersed CNTs can be produced on Al surfaces with much larger length and smaller structure damage than HEBM process. Surfactants were the probable impurity source in the SBM process. However, because high-velocity milling balls strongly impacted CNTs onto the Al surface, the dynamic ball milling process was helpful to depart surfactants to the solution from CNTs. It resulted in little surfactant in the CNT-Al powder mixture (Figure 3-5 and Figure 3-6), and post heat-treatment was not essential for SBM process. However, to remove the remained surfactants, post heat-treatment was essential in the coating process, such as the SC process, SCF process and the Flake PM process. Therefore, these characteristics made SBM process simple and effective to obtain a homogeneous CNT dispersion with a large aspect ratio and small structure damages, which was more fascinating among the present dispersion methods. In a recent study, the SBM process was applied on Ti matrix reported by Wang et al. [42], homogeneous CNT dispersion and noticeable strength improvement were also achieved in Ti matrix composites reinforced with 0.4 wt.% CNTs. It suggested the great application potential of the developed SBM process in metal matrix composites.

3.6 Conclusions

In this chapter, an integrated strategy of SBM process was applied to overcome the problems and challenges in the CNT dispersion. CNT dispersion quality was investigated and compared with those of the conventional approaches in CNT-Al composite system. The

characteristics of the present CNT-dispersion methods, including the conventional and some newly developed processes, were compared with the SBM process. Moreover, CNT/Al composites were fabricated by SBM and following consolidations by powder metallurgy. The mechanical properties of CNT/Al composites were characterized. The role of CNT addition in the strengthening of CNT/Al composites was examined and discussed. Major findings are listed below.

(1) The combining use of the solution coating and HEBM in the SBM process provided a simple and effective approach to obtain un-bundled CNTs on the Al powders. There was small structure damage or length reduction of CNTs dispersed by the SBM process.

(2) CNT addition has small effects on the grain size and orientation on the Al matrix. The CNT/Al composite extrusions had similar smooth surfaces with pure Al.

(3) Small amount of Al_4C_3 nanorods were detected in CNT/Al composites. It might be helpful for the load transfer strengthening and contributed to the strength improvement in CNT/Al composites.

(4) The experimental strengthening effect of dispersed CNTs agreed with the strengthening potential predicted by the generalized shear-lag model. It suggested that the reinforcing potential of CNTs has been almost reached in the present process.

(5) The structure damage of CNTs that dispersed by the SBM process was much smaller than that of the traditional HEBM process. Moreover, there was minor effect of consolidating on the structure of remained CNTs.

(6) The present results showed that the SBM process was promising for producing high-performance metal matrix composites reinforced with CNTs.

References

[1] Fukuda H, Kondoh K, Umeda J, Fugetsu B. Interfacial analysis between Mg matrix and carbon nanotubes in Mg–6wt.% Al alloy matrix composites reinforced with carbon nanotubes. Composites Science and Technology 2011;71:705-9.
[2] Kondoh K, Fukuda H, Umeda J, Imai H, Fugetsu B. Microstructural and mechanical behavior of multi-walled carbon nanotubes reinforced Al–Mg–Si alloy composites in aging treatment. Carbon 2014;72:15-21.
[3] Jiang L, Li Z, Fan G, Cao L, Zhang D. Strong and ductile carbon nanotube/aluminum bulk nanolaminated composites with two-dimensional alignment of carbon nanotubes. Scripta Materialia 2012;66:331-4.

[4] Jiang L, Li Z, Fan G, Cao L, Zhang D. The use of flake powder metallurgy to produce carbon nanotube (CNT)/aluminum composites with a homogenous CNT distribution. Carbon 2012;50:1993-8.
[5] Jiang L, Fan G, Li Z, Kai X, Zhang D, Chen Z, et al. An approach to the uniform dispersion of a high volume fraction of carbon nanotubes in aluminum powder. Carbon 2011;49:1965-71.
[6] Li Z, Jiang L, Fan G, Xu Y, Zhang D, Chen Z, et al. High volume fraction and uniform dispersion of carbon nanotubes in aluminium powders. Micro & Nano Letters 2010;5:379.
[7] Choi H, Shin J, Min B, Park J, Bae D. Reinforcing effects of carbon nanotubes in structural aluminum matrix nanocomposites. Journal of Materials Research 2011;24:2610-6.
[8] Choi HJ, Shin JH, Bae DH. Grain size effect on the strengthening behavior of aluminum-based composites containing multi-walled carbon nanotubes. Composites Science and Technology 2011;71:1699-705.
[9] Islam M, Rojas E, Bergey D, Johnson A, Yodh A. High weight fraction surfactant solubilization of single-wall carbon nanotubes in water. Nano letters 2003;3:269-73.
[10] Coleman JN. Liquid-Phase Exfoliation of Nanotubes and Graphene. Advanced Functional Materials 2009;19:3680-95.
[11] Kim SW, Kim T, Kim YS, Choi HS, Lim HJ, Yang SJ, et al. Surface modifications for the effective dispersion of carbon nanotubes in solvents and polymers. Carbon 2012;50:3-33.
[12] Huang YY, Terentjev EM. Dispersion of Carbon Nanotubes: Mixing, Sonication, Stabilization, and Composite Properties. Polymers 2012;4:275-95.
[13] Simões S, Viana F, Reis MAL, Vieira MF. Improved dispersion of carbon nanotubes in aluminum nanocomposites. Composite Structures 2014;108:992-1000.
[14] Vaisman L, Wagner HD, Marom G. The role of surfactants in dispersion of carbon nanotubes. Advances in colloid and interface science 2006;128-130:37-46.
[15] Morsi K, Esawi A. Effect of mechanical alloying time and carbon nanotube (CNT) content on the evolution of aluminum (Al)–CNT composite powders. Journal of Materials Science 2007;42:4954-9.
[16] Esawi AMK, Morsi K, Sayed A, Taher M, Lanka S. The influence of carbon nanotube (CNT) morphology and diameter on the processing and properties of CNT-reinforced aluminium composites. Composites Part A: Applied Science and Manufacturing 2011;42:234-43.
[17] Bakshi SR, Agarwal A. An analysis of the factors affecting strengthening in carbon nanotube reinforced aluminum composites. Carbon 2011;49:533-44.
[18] Shokrieh MM, Rafiee R. Investigation of nanotube length effect on the reinforcement efficiency in carbon nanotube based composites. Composite Structures 2010;92:2415-20.
[19] Hong SH, Chung KH, Lee CH. Effects of hot extrusion parameters on the tensile properties and microstructures of SiC w-2124Al composites. Materials Science and Engineering: A 1996;206:225-32.
[20] Ci L, Ryu Z, Jin-Phillipp NY, Rühle M. Investigation of the interfacial reaction between multi-walled carbon nanotubes and aluminum. Acta Materialia 2006;54:5367-75.
[21] He CN, Zhao NQ, Shi CS, Song SZ. Mechanical properties and microstructures of carbon nanotube-reinforced Al matrix composite fabricated by in situ chemical vapor deposition. Journal of Alloys and Compounds 2009;487:258-62.
[22] Bakshi SR, Lahiri D, Agarwal A. Carbon nanotube reinforced metal matrix composites - a review. International Materials Reviews 2010;55:41-64.

[23] Kelley A, Tyson W. Tensile Properties of Fiber-Reinforced Metals. Journal of Mechanical and Physical Solids 1965;13:329-50.
[24] Nam DH, Cha SI, Lim BK, Park HM, Han DS, Hong SH. Synergistic strengthening by load transfer mechanism and grain refinement of CNT/Al–Cu composites. Carbon 2012;50:2417-23.
[25] Tjong SC. Recent progress in the development and properties of novel metal matrix nanocomposites reinforced with carbon nanotubes and graphene nanosheets. Materials Science and Engineering: R: Reports 2013;74:281-350.
[26] Ryu HJ, Cha SI, Hong SH. Generalized shear-lag model for load transfer in SiC/Al metal-matrix composites. Journal of materials research 2003;18:2851-8.
[27] Chu K, Jia C-c, Jiang L-k, Li W-s. Improvement of interface and mechanical properties in carbon nanotube reinforced Cu–Cr matrix composites. Materials & Design 2013;45:407-11.
[28] Esawi AMK, Morsi K, Sayed A, Gawad AA, Borah P. Fabrication and properties of dispersed carbon nanotube–aluminum composites. Materials Science and Engineering: A 2009;508:167-73.
[29] Kurita H, Estili M, Kwon H, Miyazaki T, Zhou W, Silvain J-F, et al. Load-bearing contribution of multi-walled carbon nanotubes on tensile response of aluminum. Composites Part A: Applied Science and Manufacturing 2015;68:133-9.
[30] Xu W, Chenchong W, Zhichao Z, Ping L, Yanhua S, Guofu Z. Interfacial microstructure and growth mechanism of Al4C3 in Grf/Al composites fabricated by liquid pressure method. Micron 2014;65:10-4.
[31] Wei H, Li Z, Xiong D-B, Tan Z, Fan G, Qin Z, et al. Towards strong and stiff carbon nanotube-reinforced high-strength aluminum alloy composites through a microlaminated architecture design. Scripta Materialia 2014;75:30-3.
[32] Stein J, Lenczowski B, Anglaret E, Fréty N. Influence of the concentration and nature of carbon nanotubes on the mechanical properties of AA5083 aluminium alloy matrix composites. Carbon 2014;77:44-52.
[33] Sun Y, Cui H, Gong L, Chen J, Shen P, Wang C. Field nanoemitter: one-dimension Al 4 C 3 ceramics. Nanoscale 2011;3:2978-82.
[34] Yoo SJ, Han SH, Kim WJ. Strength and strain hardening of aluminum matrix composites with randomly dispersed nanometer-length fragmented carbon nanotubes. Scripta Materialia 2013;68:711-4.
[35] Liao J-z, Tan M-J, Sridhar I. Spark plasma sintered multi-wall carbon nanotube reinforced aluminum matrix composites. Materials & Design 2010;31:S96-S100.
[36] Pérez-Bustamante R, Gómez-Esparza CD, Estrada-Guel I, Miki-Yoshida M, Licea-Jiménez L, Pérez-García SA, et al. Microstructural and mechanical characterization of Al–MWCNT composites produced by mechanical milling. Materials Science and Engineering: A 2009;502:159-63.
[37] Liao J, Tan M-J. Mixing of carbon nanotubes (CNTs) and aluminum powder for powder metallurgy use. Powder Technology 2011;208:42-8.
[38] He C, Zhao N, Shi C, Du X, Li J, Li H, et al. An Approach to Obtaining Homogeneously Dispersed Carbon Nanotubes in Al Powders for Preparing Reinforced Al-Matrix Composites. Advanced Materials 2007;19:1128-32.
[39] Tang J, Fan G, Li Z, Li X, Xu R, Li Y, et al. Synthesis of carbon nanotube/aluminium composite powders by polymer pyrolysis chemical vapor deposition. Carbon 2013;55:202-8.

[40] Esawi A, Morsi K. Dispersion of carbon nanotubes (CNTs) in aluminum powder. Composites Part A: Applied Science and Manufacturing 2007;38:646-50.
[41] Liu ZY, Xu SJ, Xiao BL, Xue P, Wang WG, Ma ZY. Effect of ball-milling time on mechanical properties of carbon nanotubes reinforced aluminum matrix composites. Composites Part A: Applied Science and Manufacturing 2012;43:2161-8.
[42] Wang F-C, Zhang Z-H, Sun Y-J, Liu Y, Hu Z-Y, Wang H, et al. Rapid and low temperature spark plasma sintering synthesis of novel carbon nanotube reinforced titanium matrix composites. Carbon 2015;95:396-407.

Chapter 4
Interface Control in Carbon Nanotube Reinforced Al Matrix Composites

In this chapter, attempts were made to set up the relationships between interfacial structures and mechanical properties of CNT/Al composites. Two processing routes, i.e. post heat treatment (PHT) and spark plasma sintering (SPS), were applied to tune interfacial structures. Since processing temperature was the most significant factor influencing the interfacial reactions, it was used as the experimental variable in the two routes.

In the first part, the effect of PHT temperature on the interfacial and tensile properties of CNT/Al composites were investigated. To clarify the observed abnormal decrease of both strength and ductility of pure Al and CNT/Al composites at high PHT temperatures, the microstructures were characterized. To clarify the observed cracking phenomenon, an *in-situ* study was performed to examine the microstructures of CNT/Al composites at elevated temperatures. Various SPS temperatures were applied to investigate the effect of powder bonding before PHT on the cracking behaviors. Based on the results, the cracking mechanism was proposed and the approaches for suppressing cracking were discussed.

In the rest part, the interfacial structures of CNT/Al composites processed under various SPS temperatures were systematically investigated by TEM studies. The density and electrical conductivity were characterized to understand the macroscopic interface conditions. The possibly formed interfacial phases were examined by X-ray diffraction and Raman spectroscopy. Detailed TEM and high-resolution TEM analyses were used to investigate the microscopic structures of CNT and interfacial carbide phases. To understand the strengthening effect of CNTs, the tensile properties of pure Al and CNT/Al composites were studied. The effect of SPS temperature and interfacial characteristics on tensile properties were investigated. Strength improvements contributed by grain refinement and load transfer were quantitatively estimated using strengthening models. The fracture morphologies were characterized to understand the failure modes of CNTs in composites during tensile tests. Based on the results, the relation between the interfacial characteristics and the load transfer efficiency was discussed.

4.1 Effect of annealing temperature on interfacial and tensile properties

Figure 4-1 shows the dispersion effect of CNTs on Al powder surface through the solution coating (SC) process. After high energy ball milling (HEBM) for 4 h, Al powders changed to flaky morphologies (Figure 4-1a). The Al flakes had a thickness of several micrometers and a diameter of several tens of micrometers. Many homogeneously dispersed CNTs could be observed on the flaky Al surface (Figure 4-1c), which has been described in Section 3.1. However, some small CNT clusters with size of ~1 μm were still observed, as indicated in Figure 4-1b and d by arrows.

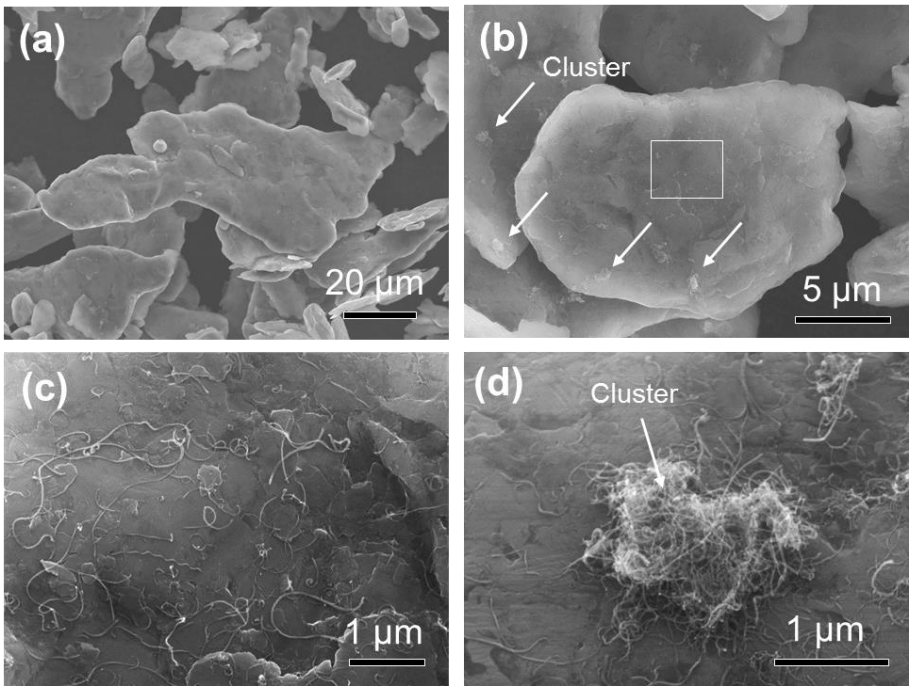

Figure 4-1. CNT distribution on Al powder surface. (a) A low magnification view shows Al flakes. (b) A general view of CNT dispersion. (c) A local view shows good CNT dispersion. (d) A local view shows a typical CNT cluster.

The phase compositions in CNT/Al composites processed under different PHT temperatures are shown in **Figure 4-2**. As the temperature was below 550^{o}C, only Al peaks were observed in CNT/Al composites, similar to the pure Al materials. As PHT temperature is attained to 550^{o}C, weak peaks corresponding to the Al_4C_3 phase were observed in the

CNT/Al composite. When the temperature exceeded 550°C, the Al_4C_3 peak intensity increased, suggesting that the degree of interfacial reaction and the amount of formed Al_4C_3 phase were enhanced at elevated temperatures.

At PHT temperature of 650°C, except for Al and Al_4C_3 peaks, some unknown peaks appeared in the CNT/Al composite (Figure 4-2). It was because that some trinary Al-C-O reactions [1] might happen as the temperature was near the melting point of Al (T_m, 660°C). The results indicated that it might be possible to control the Al_4C_3 amount via the temperature of PHT process.

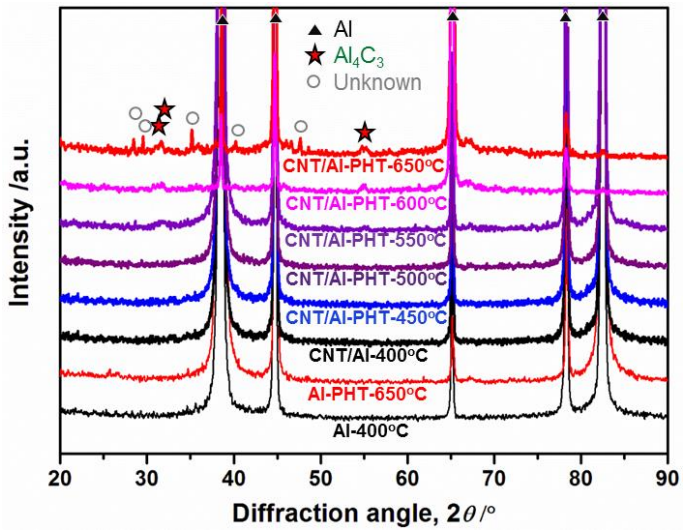

Figure 4-2. XRD patterns of pure Al and CNT/Al composites processed by post heat-treatment at various temperatures.

Figure 4-3 shows the engineering stress-strain curves of pure Al and CNT/Al composites with different PHT temperatures. Both of the two kinds of materials experienced the same Al-flake producing, CNT coating, drying, compacting and hot-extruding processes before PHT. It can be seen that both pure Al and CNT/Al composites showed similar tendencies of mechanical properties, as PHT temperature is increased from 450°C to 650°C. At PHT temperature of 450°C, both the strength and ductility were interestingly improved. It was probably due to the simultaneous enhancement of powder bonding and interfacial bonding during the PHT process at elevated temperatures.

However, as PHT temperature was increased to 550°C, strength and ductility noticeably decreased, even lower than the as-extruded materials. As PHT temperature was further increased to 650°C, the strength dramatically degraded to a low level. The ductility of CNT/Al composite also showed a distinct decrease. The same tendency of pure Al and composites suggested that it is not the interfacial structures but other factors that played dominant roles in determining the observed degradation of mechanical properties of CNT/Al composites processed at high PHT temperatures over 550°C.

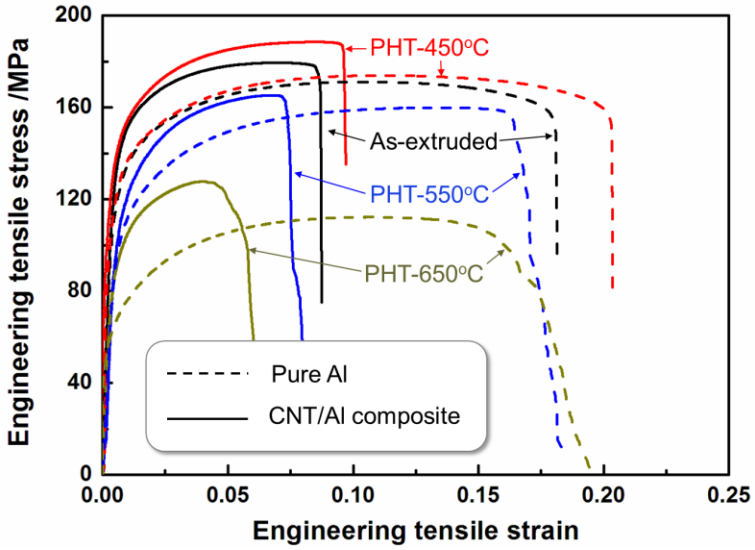

Figure 4-3. Engineering tensile stress-strain curves of pure Al and CNT/Al composites experienced different post heat-treatment temperatures.

4.2 Micro-crack formation in powder metallurgy Al matrix composites during annealing

4.2.1 Cracking in annealed materials

In order to understand the reason causing the degradation of mechanical properties of the materials experienced the PHT process, the microstructures of as-extruded Al and Al sample after PHT-550°C process were examined. From **Figure 4-4**a and b, it is clear that the as-extruded materials showed nearly dense structure, with a relative density of 99.5% measured by the Archimedes method. However, many micro-cracks formed in the Al sample after PHT-550°C process, as shown in Figure 4-4c and d. This observation agreed with the

decrease of the measured relative density (97.3%). Undoubtedly, the formation of micro-cracks was fatal for the mechanical response of Al and CNT/Al composites during tensile test, because they acted as preferential sites for the initiation and growth of cracks [2, 3]. It reasonably resulted in the observed degraded tensile properties (Figure 4-3).

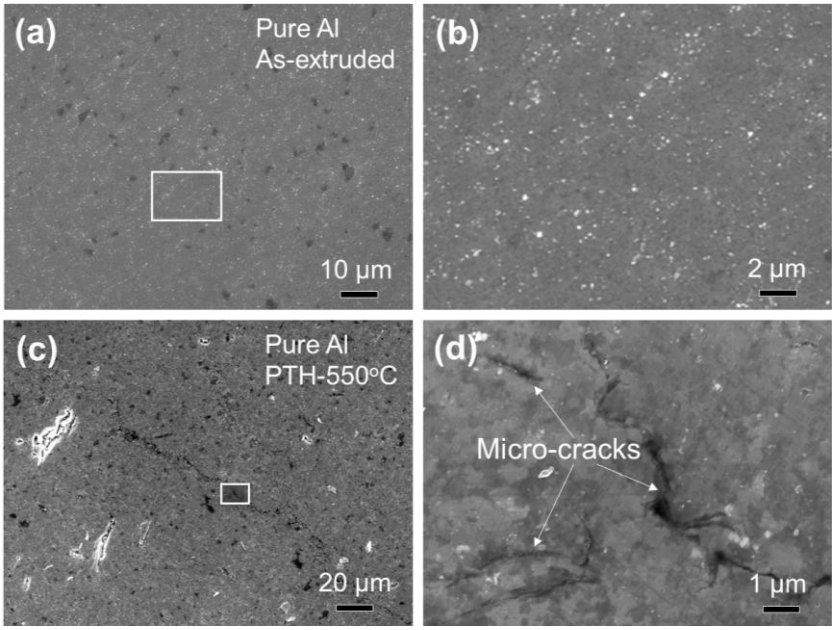

Figure 4-4. SEM observation of as-extruded Al (a, b) and Al sample experienced post heat-treatment (PHT) at 550°C (c,d) at different magnifications.

4.2.2 In-situ observation on micro-crack formation at elevated temperatures

To confirm the cracking phenomenon, an in-situ study was applied on the CNT/Al composite at elevated temperatures. **Figure 4-5** shows the in-situ OM observation results of the as-extruded CNT/Al composite during the PTH process. During the heating-up process from 400-550°C (Stage A-D in Figure 4-5a), no obvious microstructure change was observed (Figure 4-5b). At 567°C (Stage E in Figure 4-5), a micro-crack formed in the sample. As the temperature was further increased, the cracks noticeably expanded with increased length and width (the black area in Stage F-H in Figure 4-5). It was clear that the formation of cracks happened during the heating-up process during PHT. The crack initiation temperature (567°C) was a little higher than 550°C of which temperature micro-cracks were observed

(Figure 4-4d) in the composites. It was probably because the size or dimension of the micro-cracks formed at 550°C was too small (observed at magnification of ×500 in Figure 4-4c) to be detected at low magnification of ×30, as shown in Stage D of Figure 4-5.

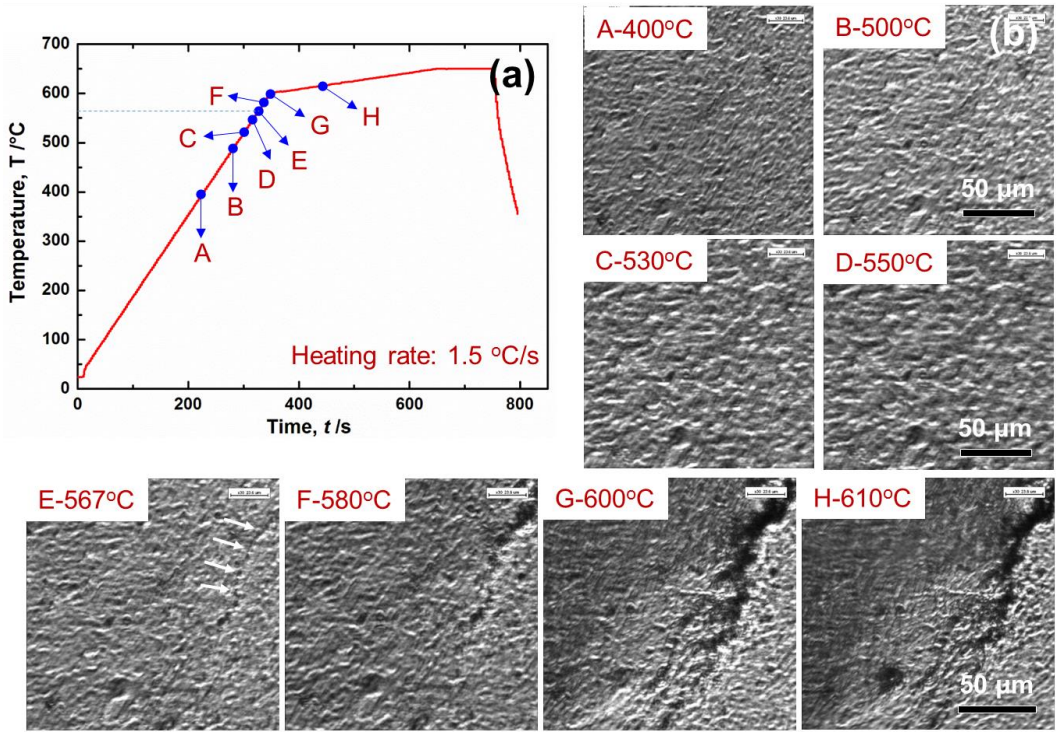

Figure 4-5. The recorded temperature-time curve (a) and corresponding OM images during the in-situ heat-treatment process (b). The capital letters (A-H) indicates different stages during PHT. Note a micro-crack formed during the heating-up process at 567°C as arrows indicated in stage E.

4.2.3 Micro-crack formation mechanism

To further investigate the formation mechanism of micro-cracks during PHT process, CNT/Al composites processed under different consolidation process were experienced a same PHT-650°C process. The OM microstructures are shown in **Figure 4-6**. With the SPS-PHT sample, no crack was were observed in the sample. With the SPS450°C-extrusion-PHT sample, large holes or cracks formed. As SPS temperature was increased to 550°C, the crack size noticeably decreased. As SPS temperature was further increased to 650°C, no crack was observed. The results suggested that the crack formation only happened to those materials experienced hot-extrusion and PHT process. Materials consolidated by SPS process showed

no cracks. Moreover, if hot-extrusion process follows with the SPS process, the SPS temperature showed great effect on the crack formation during the PHT process. High SPS temperature was effective to suppress the crack formation during PHT process.

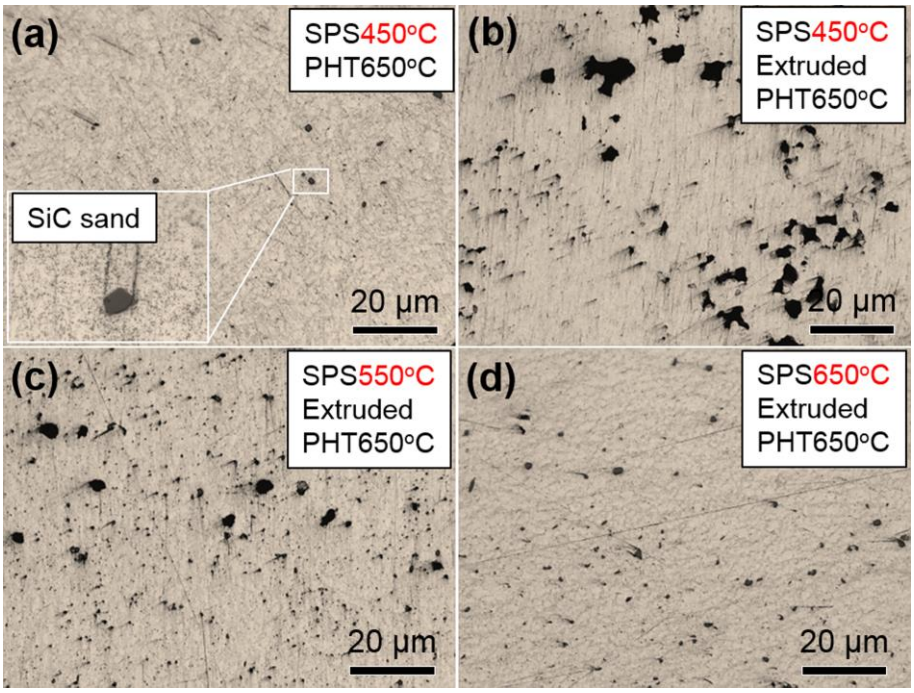

Figure 4-6. OM microstructure of CNT/Al composites under different consolidation processes followed with a same PHT-650°C process. Note that the small grey materials in (a) and (d) are SiC particles set in the soft matrix during sand-grinding. The large black areas in (b) and (c) are holes or cracks.

It was well known that during some severe plastic deformation (SPD) processes where SPD happened to materials, such as torsion, rolling and hot-extrusion, large quantity of energy was stored in materials [4]. The energy existed as various states, such as dislocation, refined grains and residual stress [5]. **Figure 4-7** schematically shows the evolution of stress states in Al powders during processing. The powders acted as springs (Figure 4-7a) that were able to store the stress under the external mechanical force during the SPD processes (Figure 4-7b). At the same time, material density was improved by decreasing the distance between powders, forming primary powder boundaries (PPBs). Both strong metallurgical bonding and weak bonding might exist in the materials, which was dependent

on the SPD parameters. In Al materials, the dense alumina film on Al powder surface was also one factor leading to the weak powder bonding [6].

As a PHT process was applied to the SPD materials, such as compactions of ball milled powders and as-extruded materials, the remained residual stress inside powders would release under the thermal impact, like springs once more. Accompanied with the release of residual stress, strain was produced at the PPBs. If the powder bonding prior to PHT was not effective enough (Figure 4-7b), micro-cracks might form in the material during the PHT process (Figure 4-7c). On the other hand, with strong powder bonding in the composite sintered at high temperatures (Figure 4-6d), the cracks were successfully prevented. Therefore, to suppress possibly formed micro-cracks, low PHT temperatures or good powder bonding before SPD process were recommended. These results might provide significant guidance for the use of PHT process on SPD materials.

Additionally, the results indicated that the information on the relation between the interfacial structure and mechanical properties could not be obtained by the PHT process. It was because the mechanical properties were greatly degraded because of the micro-crack formation at PPBs. However, the PHT process might be still effective to control the interfacial reaction with different amount of Al_4C_3 phases (Figure 4-3). Direct temperature control of the sintering process would be another approach to investigate the relation between interfaces and mechanical properties, as demonstrated in the following sections.

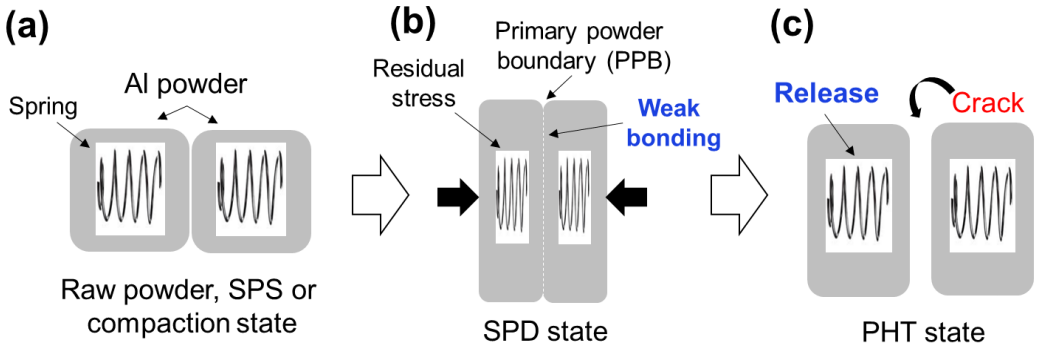

Figure 4-7. Scheme of micro-crack formation in materials experienced SPD and PHT process. (a) Raw powder or consolidated bulk by SPS or compaction. (b) The materials experienced SPD process. (c) The SPD materials experienced PHT state. Note that springs inside powders schematically suggested stress state in materials.

4.3 Macroscopic analysis on interfacial characteristics of carbon nanotube/Al composites

4.3.1 Carbon nanotube dispersion

Figure 4-8 shows the CNT dispersion effect on the fabricated flaky Al powder surface after the developed mechanical solution coating (MSC) process. The homogeneously dispersed single CNTs on Al surface could be observed in Figure 4-8b. Compared with the previous solution coating process, the improved CNT dispersion was achieved in the present MSC process due to the dynamic blending assisted dispersion of CNTs, as revealed in Section 3.1 and Section 3.2. Compared with the previous SBM process as described in Chapter 3, the MSC method developed in this study was simpler and would cause less CNT damage because of the low energy input during the dispersion process [7].

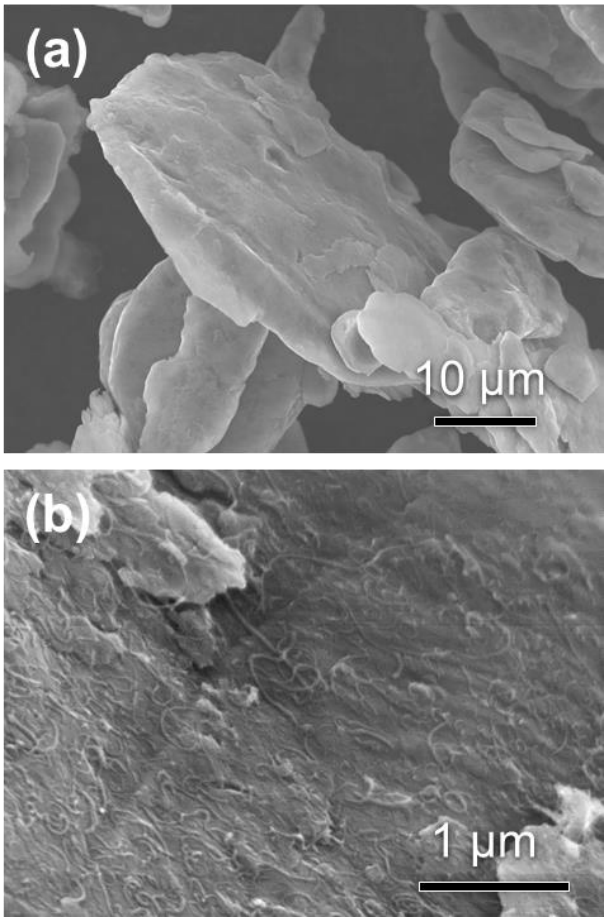

Figure 4-8. CNT distribution on flaky Al powder surface. (a) A low magnification view. (b) A high-magnification view shows well-dispersed CNTs on flakey powder surface.

4.3.2 Density and electrical conductivity

Figure 4-9 shows the relative density of as-sintered pure Al and CNT/Al composites. It was observed that the relative densities of both pure Al and CNT/Al increased with increasing SPS temperature from 427°C to 627°C (Figure 4-9), which was reasonably due to the improved plastic deformation and resultant decrease of porosities and increase of bonding conditions at higher sintering temperatures. It was also seen that before 627°C, the relative density of CNT/Al was lower than that of the corresponding pure Al material. At 627°C, both of CNT/Al and pure Al had a high relative density of ~99%. However, relative density only reflects the apparent compactness but not the atom-scale bonding conditions between Al powders or between Al and CNT. The conductive properties, such as electrical conductivity (EC), were greatly dependent on the bonding conditions in MMCs [8].

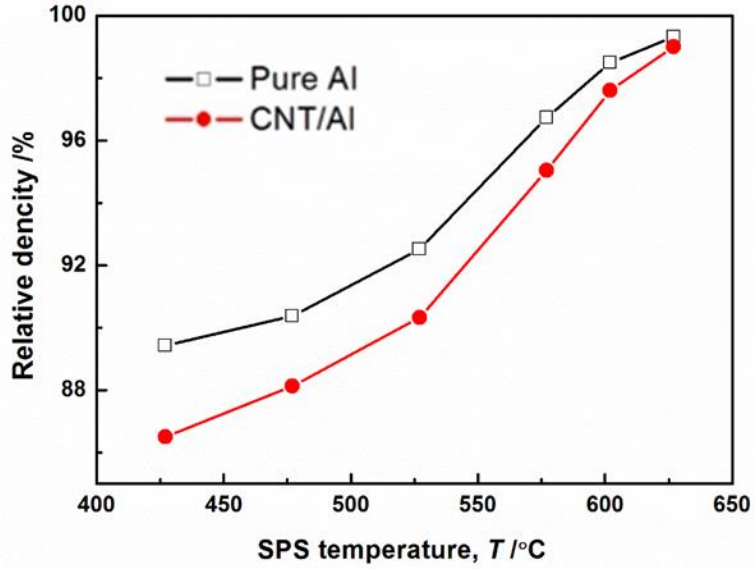

Figure 4-9. Relative density of as-sintered pure Al and CNT/Al composites with various sintering temperatures.

Figure 4-10 shows the measured EC of as-sintered pure Al and CNT/Al composites. It was observed that at 427°C and 477°C, the EC of pure Al and CNT/Al composites showed extremely low values of ~0 IACS%, suggesting the non-bonding state of Al grains. It was interesting to see that dramatic EC increases of pure Al and CNT/Al composites happened when ST exceeded 527°C. However, EC of CNT/Al composite was much smaller than that of

pure Al at 527°C and 577°C. Then at 627°C, this difference became very small. These facts suggested that CNT additions had great effect on inhibiting the sintering-induced bonding of Al powders at low sintering temperatures [9].

The results suggest that in as-sintered CNT/Al composites, the bonding between Al powders and between CNTs and Al matrix were effective at 627°C, but insufficient below it. After hot-extrusion, relative density of all pure Al and CNT/Al composites sintered at different sintering temperatures were measured as over 99%. Although EC was not able to measure due to the size restrict of extruded samples, it could be expected that the bonding conditions were still different because of their large difference in as-sintered materials.

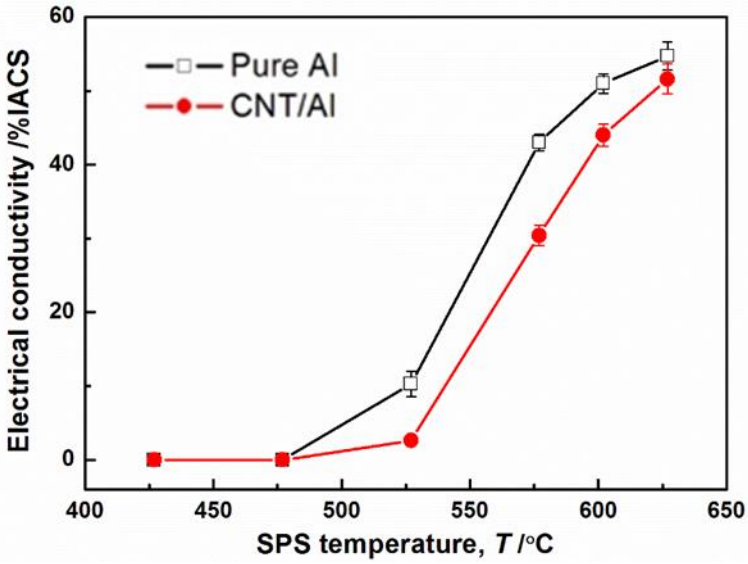

Figure 4-10. Electrical conductivity of as-sintered pure Al and CNT/Al composites with various sintering temperatures.

4.3.3 Grain information

The grain orientation and grain size (GS) of pure Al and CNT/Al composites are shown in **Figure 4-11**. All pure Al (sintered under 427°C, 527°C and 627°C as typically shown in Figure 4-11a through c respectively) and corresponding CNT/Al composites (Figure 4-11d through f) showed <111> oriented texture along the extrusion direction. This type of texture became extremely strong at 627°C for pure Al (Figure 4-11c) and CNT/Al composite (Figure 4-11f). It was reasonably because during hot-extrusion the grain rotation

ability could be improved with enhanced bonding conditions between Al powders at a high sintering temperature of 627°C (Figure 4-10).

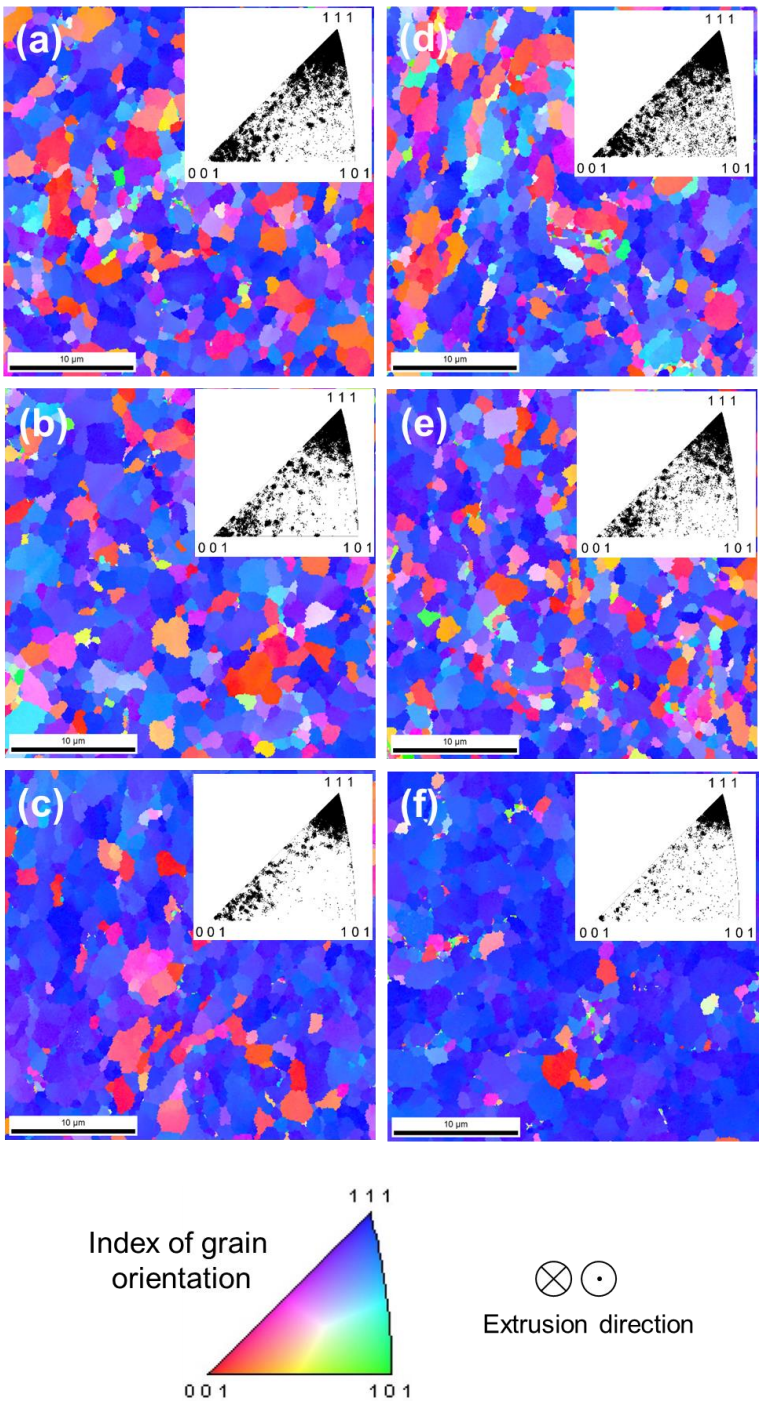

Figure 4-11. Inverse polar figures (IPFs) of grains in pure Al (a-c) and CNT/Al composites (e-g) at various sintering temperatures: (a,d) 427°C, (b,e) 527°C, (c,f) 627°C. Insets of (a)-(f) shows corresponding polar figures.

<111> texture was reported as a beneficial texture to enhance the strength of face-centered cubic materials like Al and Cu [10, 11]. Combination of SPS and hot-extrusion has been reported to produce CNT/Al composites with <111> texture, as revealed in Section 3.3.1. The present study further suggested that this kind of texture was affected by the sintering conditions prior to hot-extrusion.

Figure 4-12 shows the average GS of pure Al and CNT/Al composites as functions of sintering temperatures. The GS of pure Al was maintained within 427-577^{o}C, and increased at 627^{o}C reasonably due to the grain growth at a high sintering temperature. However, the average GS of CNT/Al composites was maintained at similar values at all STs, suggesting the pinning effect of CNTs at PPBs to prevent the grain growth during SPS, even at a high temperature (627^{o}C) near the melting point of Al (660^{o}C).

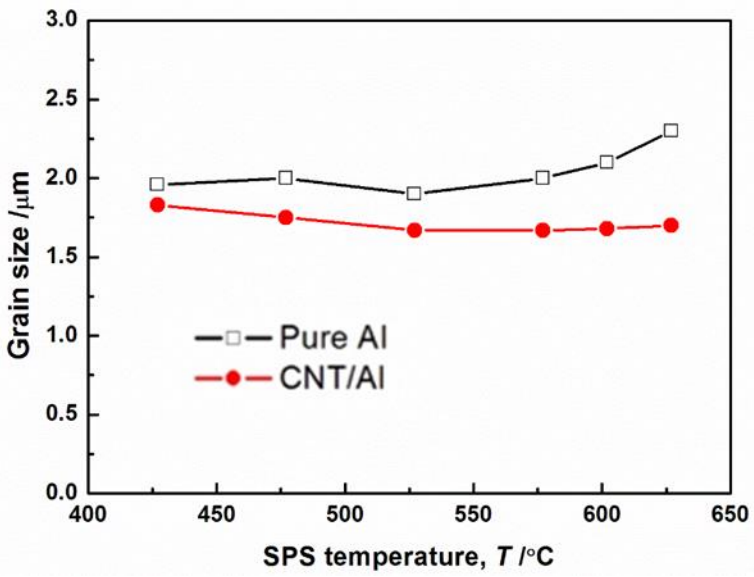

Figure 4-12. Average grain size of pure Al and CNT/Al composites as functions of SPS temperatures.

4.3.4 Phase compositions

Raman spectrum has been used for characterizing the crystal-structure of carbon-related reinforcements in AMCs in many previous studies [11-15], with CNT damage-band (D-band) near 1350 cm^{-1} and CNT graphite-band (G-band) near 1570 cm^{-1}and aluminum carbide (Al_4C_3) bands near 350 cm^{-1} and near 840 cm^{-1}. **Figure 4-13** shows the Raman

analysis of the processed materials in this study. Strong peaks at 1345 cm^{-1} and 1572 cm^{-1} in raw CNT powder and CNT/Al composites with sintering temperatures ranging from 427-627°C suggested the general remaining of CNT phases in the composites. Two weak peaks at ~360 cm^{-1} and ~830 cm^{-1}, which might be the Al_4C_3 peaks [16], was also detected in CNT/Al-602°C and CNT/Al-627°C. It suggested the probable formation of Al_4C_3 phases in the two composites.

Moreover, it was observed that there was a noticeable peak shift of G-band to 1598 cm^{-1} for CNT/Al-602°C and CNT/Al-627°C but no shift in other materials. The peak shift phenomenon has been observed accompanying with carbide formation in CNT/Al composites processed by solution ball milling as described in Chapter 3. In the present composites, Al_4C_3 was also detected by the combination of Raman and TEM analysis (TEM results are shown in the next section). These facts indicated that some specific CNT structure changes (because of G-band shift) might be the precondition for the formation of Al_4C_3 phase.

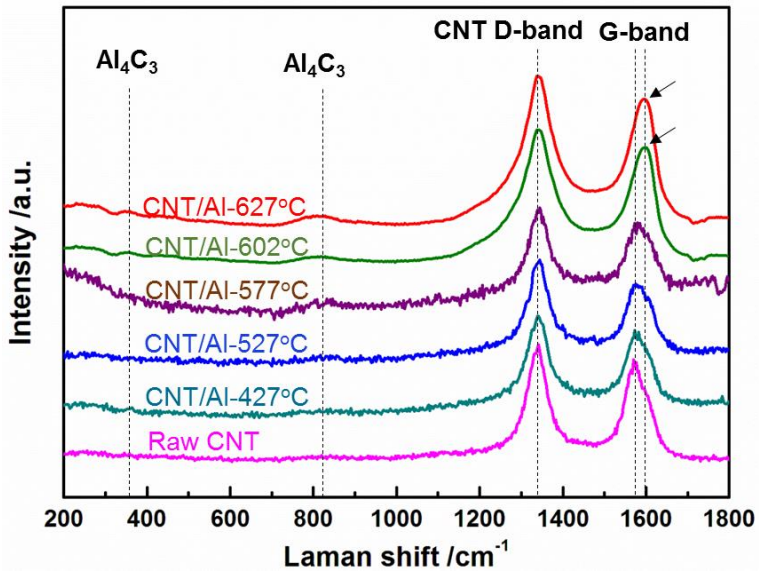

Figure 4-13. Raman spectra of CNT/Al composites processed under different sintering temperatures.

The XRD patterns of CNT/Al composites sintered at various sintering temperatures as well as the pure Al sintered at 627°C are shown in **Figure 4-14**. For CNT/Al composite sintered at 427-602°C, only Al peaks were detected. However, Al_4C_3 peaks were observed in CNT/Al-627°C (Figure 4-14), confirming the formation of Al_4C_3 phase in CNT/Al-627°C as

revealed by Raman spectra (Figure 4-13). From the combination of Raman and XRD analysis, it suggested that Al_4C_3 phases started to form at 602°C, and their amount was noticeably increased at 627°C.

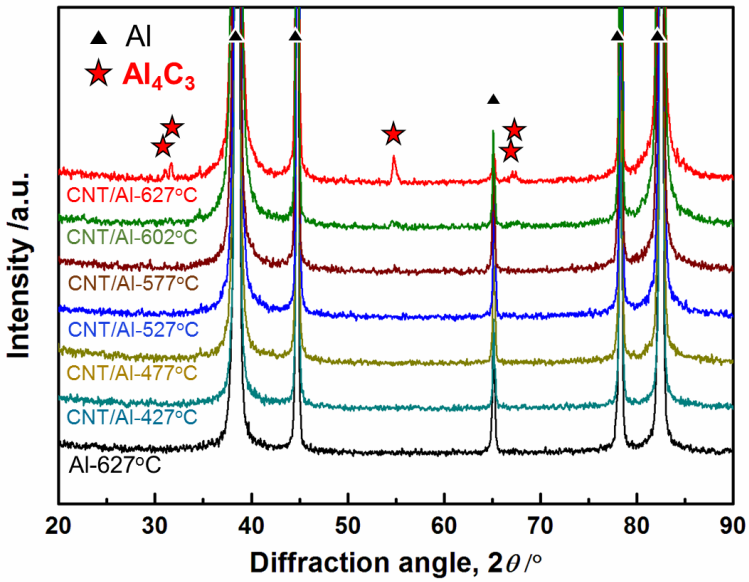

Figure 4-14. XRD spectra of CNT/Al composites processed under different STs.

4.4 TEM analysis on interfacial characteristics processed at various sintering temperatures

Low-magnification TEM views on CNT/Al composites processed at various sintering temperatures are typically shown in **Figure 4-15**. The composites showed similar average grain size of ~1.5 μm, basically agreeing with the EBSD results (Figure 4-12). Only dislocations were observed at low-magnification views. To confirm the CNT phase, the analysis results by combining TEM and EDS on the composite CNT/Al-527°C are shown in **Figure 4-16**. From BF-TEM images (Figure 4-16a), some fibrous phases were observed in the matrix. From the element distribution images (Figure 4-16b through d), high carbon concentration and low Al concentration were observed corresponded to the fibrous phases. These fibrous phases were therefore identified as CNTs. Around CNTs, rich oxygen content was also observed. However, some Al grains were also rich in oxygen. High oxygen concentration in CNT/Al was resulted from the Al-flake producing process using HEBM [17].

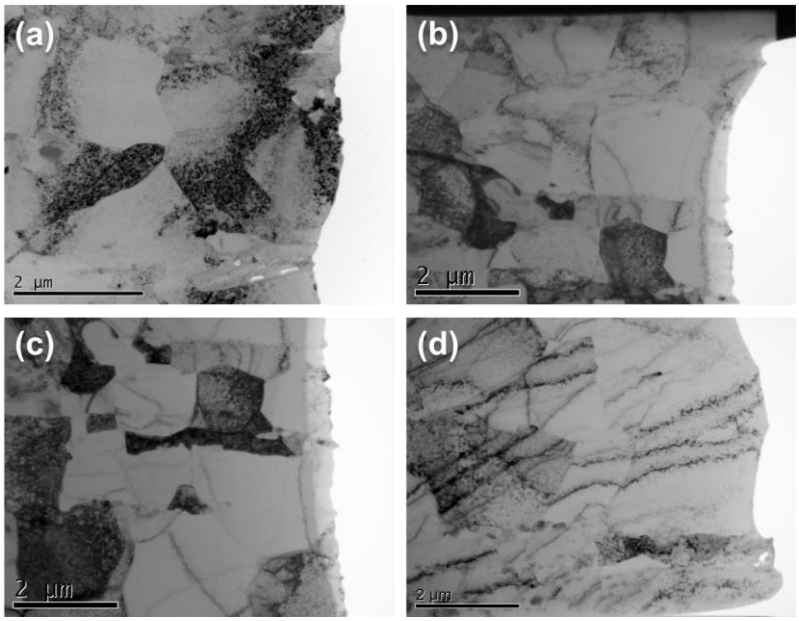

Figure 4-15. Low-magnification TEM views on CNT/Al composites processed under sintering temperatures of 527ºC (a), 577 ºC (b) and 627ºC (c).

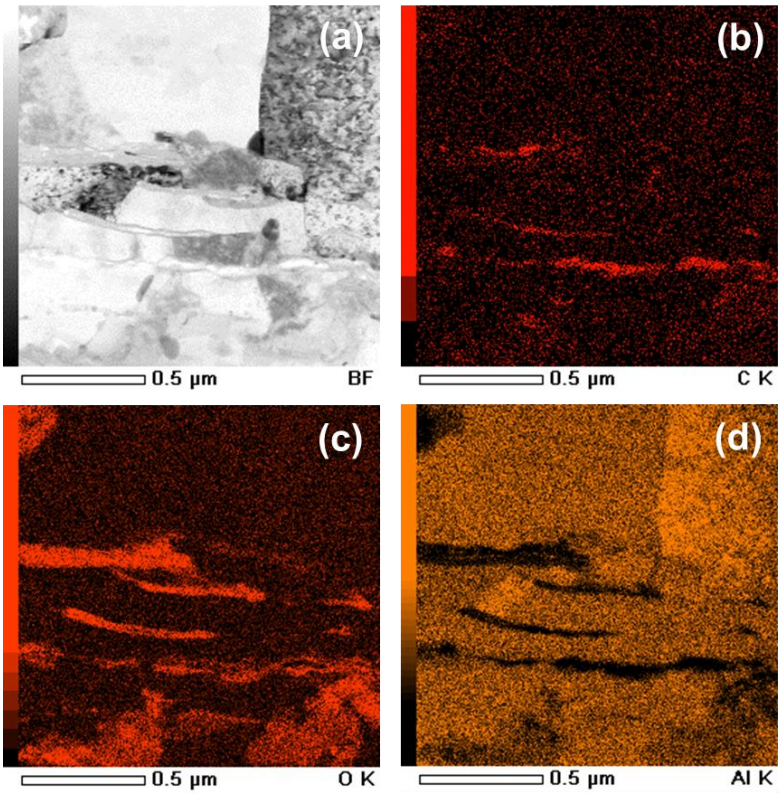

Figure 4-16. Combination of TEM and EDS analysis on CNT/Al-527ºC. (a) BF-TEM view, (b) Carbon, (c) Oxygen and (d) Al elements.

Figure 4-17 shows high-magnification views on CNTs in CNT/Al-527ºC. Owing to the similar atom weights of carbon and Al, CNTs had similar contract to matrix Al in the BF-TEM image (Figure 4-17a). However, the interfaces had a relative black contrast, so the CNTs were distinguishable in the Al matrix (Figure 4-17a). An HR-TEM image on the interface is shown in Figure 4-17b. The outline of the CNT or the CNT-Al interface can be clearly observed in black contrast. The structure of CNT walls were not seen probably due to the overlap of carbon atoms and Al atoms during the TEM observation.

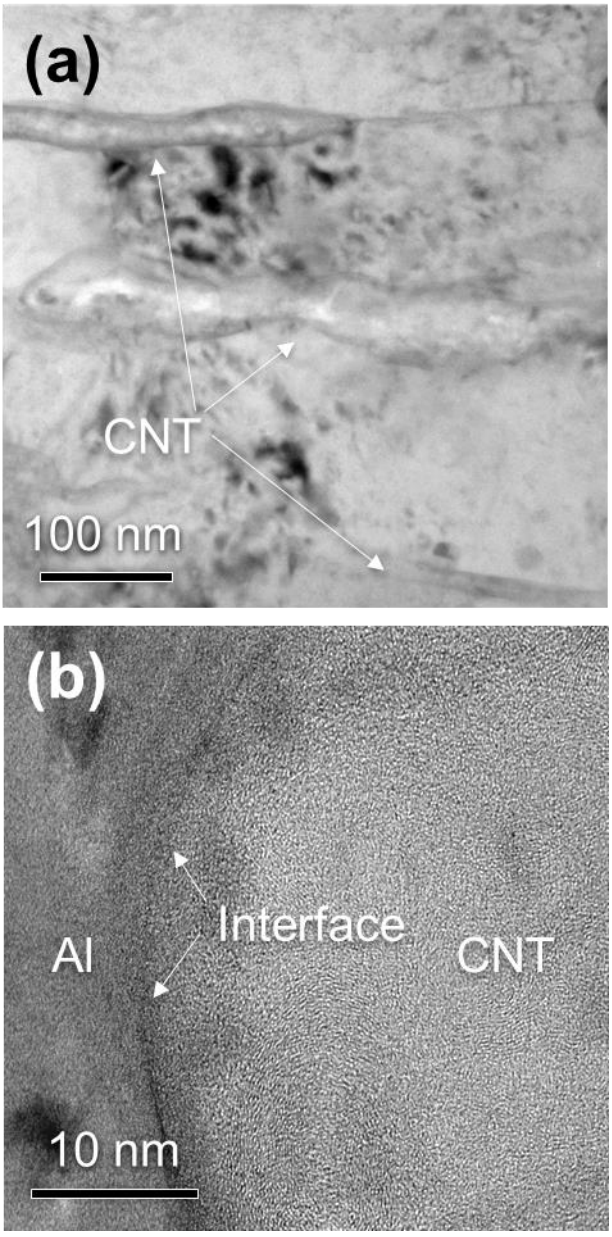

Figure 4-17. High-magnification TEM views on CNTs in CNT/Al-527ºC.

Figure 4-18 and **Figure 4-19** show the TEM observations on CNT/Al-577^{o}C. Many CNTs without interfacial Al_4C_3 phases were also observed, as shown in Figure 4-18 at different magnifications. The CNTs phases with distinguishable interfaces were observed in Al matrix as the black arrows indicated in Figure 4-19a. However, Al_4C_3 phases were occasionally detected at the CNT end, as the white arrow indicated in Figure 4-19b. The Al_4C_3 phase was identified through the SAD patterns (Figure 4-19c). The Al_4C_3 phase had a fine size with a similar diameter of CNTs.

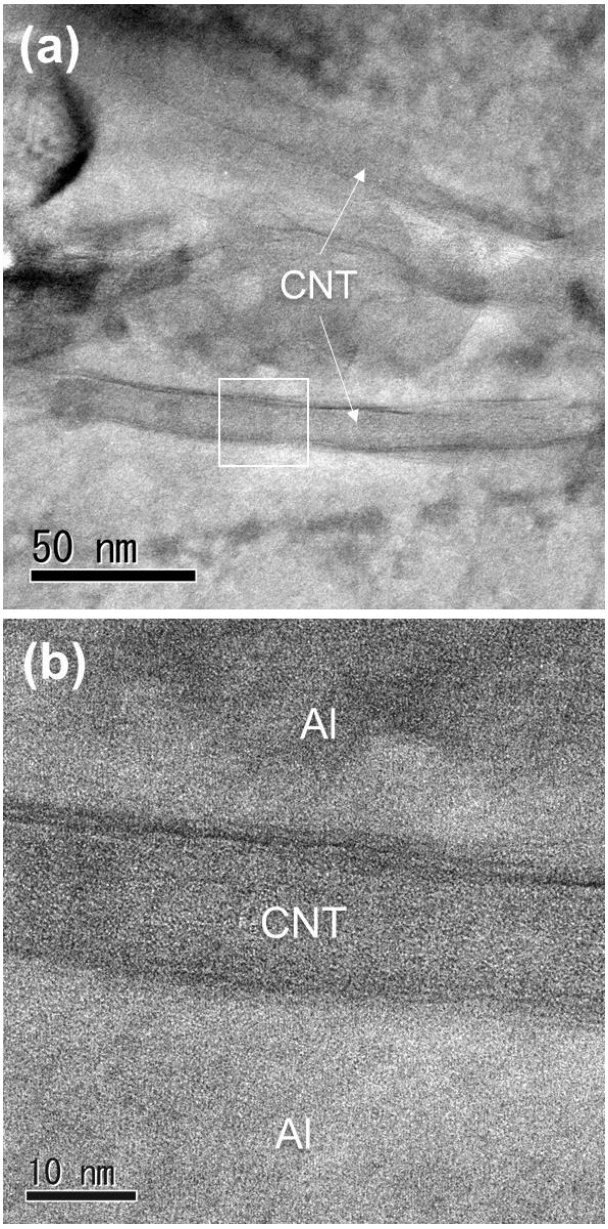

Figure 4-18. TEM views on CNTs in composite CNT/Al-577^{o}C.

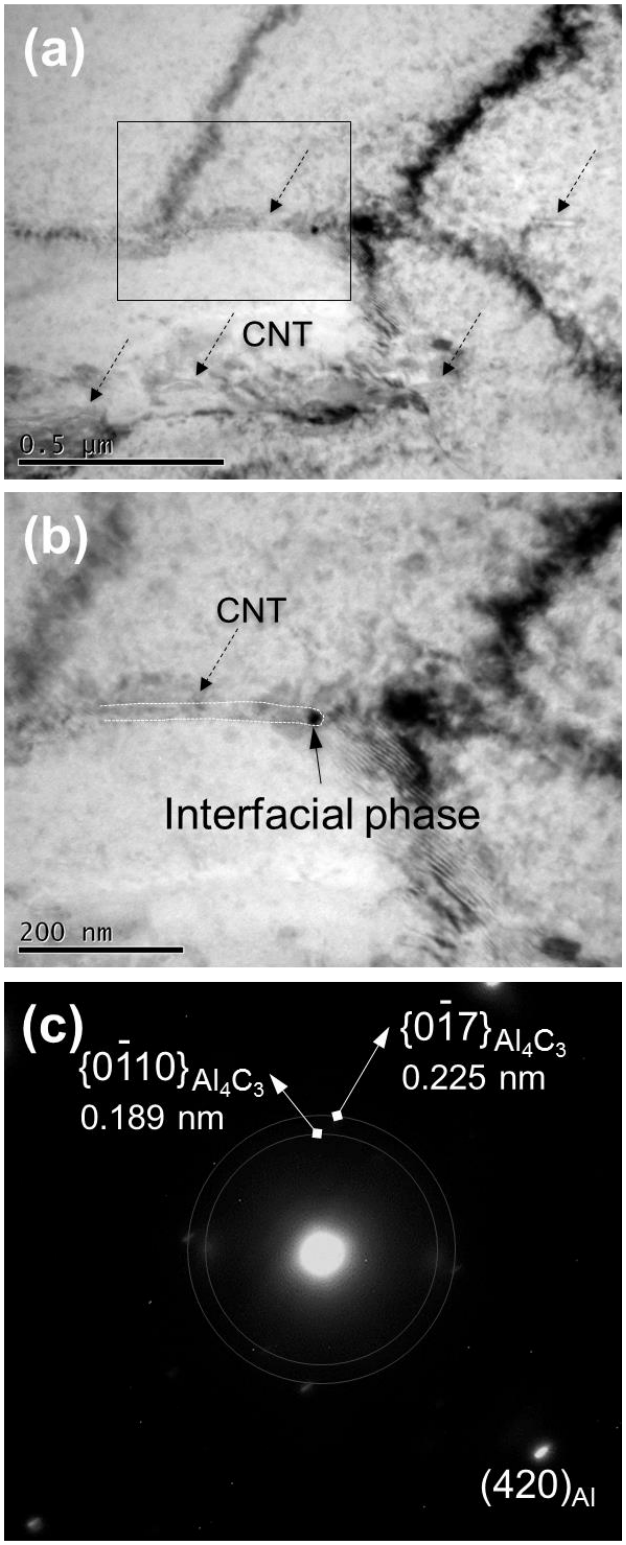

Figure 4-19. TEM views on CNT/Al-577ºC. (a) A low-magnification view, (b) A high-magnification view and (c) SAD patterns.

As sintering temperature was increased to 602ºC, the reaction degree between CNTs and Al further increased, resulting in the increase of the size and amount of Al_4C_3 phases. **Figure 4-20a** shows two typical Al_4C_3 particles formed at the interface. The Al_4C_3 phases were identified through the DF-TEM (Figure 4-20b) and SAD patterns (Figure 4-20c). A clear mono-crystal structure was detected from the SAD patterns of the carbide phase. The increase of size also contributed to clearer SAD patterns compared with the composite CNT/Al-577ºC (Figure 4-19). Remained CNT phases with gray contrasts were detected in the matrix, as black arrows indicated in Figure 4-20a. 4

From the high magnification TEM images (**Figure 4-21**), the crystal structure of the interfacial Al_4C_3 was clearly observed. The (003) atom planes of Al_4C_3 were detected. It can be seen that the Al_4C_3 phase was well-bonded to both CNT and Al matrix. Al_4C_3 was metallurgically bonded to the matrix via a straight Al_4C_3-Al boundary. However, the Al_4C_3-CNT boundary was curvilinear with several sidesteps. Owing to the fact that chemically reaction advances usually had coarse morphologies [18], the observed coarse Al_4C_3-CNT boundary (Figure 4-21b) was the place where the metallic reaction was happening. The results suggested that the interfacial reaction direction was from the matrix to CNT side, as the discontinuous arrow indicated in Figure 4-24b. In other words, Al atoms diffused from matrix to the CNT and reacted with carbon atoms, forming the *in-situ* Al_4C_3 phase. Through the interfacial Al_4C_3 phase, the remained CNT part can be tightly locked to the Al matrix, which was helpful to enhance to load transfer efficiency during tensile load.

An HR-TEM observation on the remained CNT part is shown in **Figure 4-22**. The regular CNT walls (Figure 2-3d) were not observed. One reason is that in the composite, the overlap of CNT atoms and matrix atoms increased the difficulty in observing the CNT structure during manipulating TEM (Figure 4-17b). Another possible reason is that the infiltration of Al atoms inside CNTs increased the irregularity of the CNT structure. It was reasonably due to the improved diffusion ability of Al atoms at elevated processing temperatures. The latter explanation was supported by the observed phenomenon of G-band shift (Figure 4-13). Although Al_4C_3 phase was locally detected by TEM, it was absent in the XRD patterns and very weak in the Raman profiles at 602ºC. These facts indicated the small size and limited amount of Al_4C_3 in the composite CNT/Al-602ºC. Interfacial Al_4C_3 phase

has also been observed in the study of Ci et al. [19], using heat treatment on CNT arrays and Al deposit between 450ºC and 950ºC.

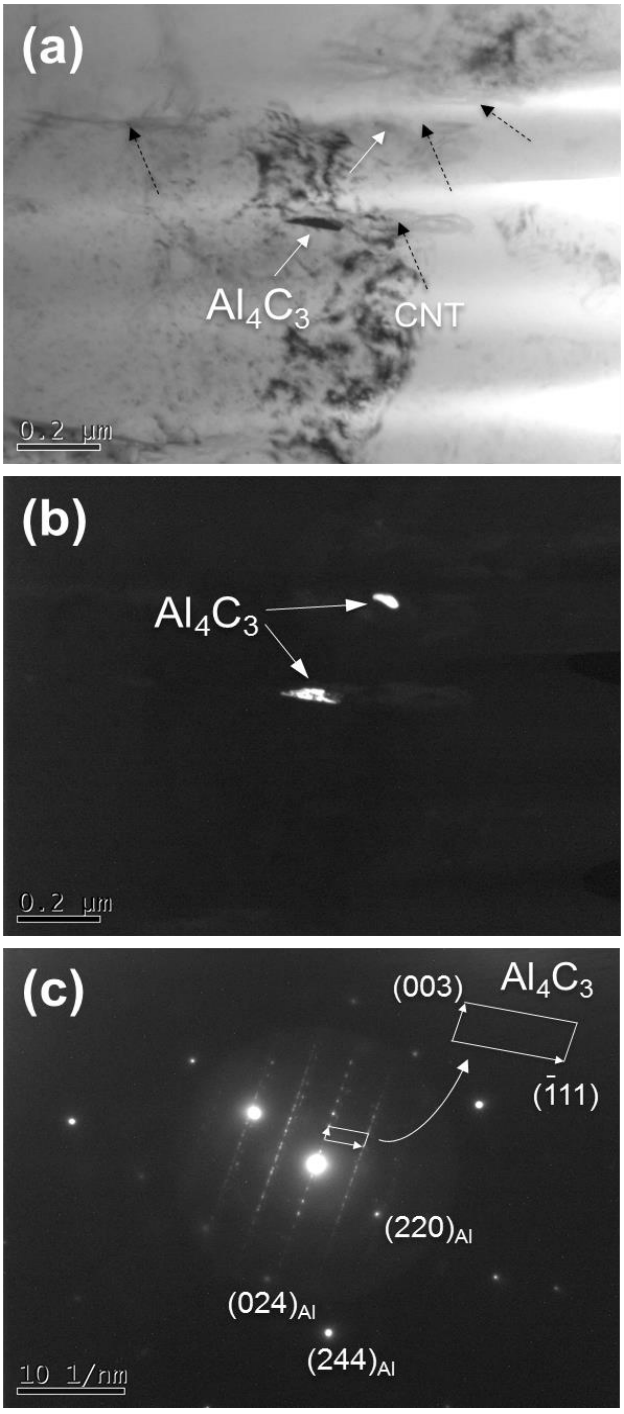

Figure 4-20. TEM views on CNT/Al-602ºC. (a) A BF-TEM view. (b) A DF-TEM view. (c) SAD patterns.

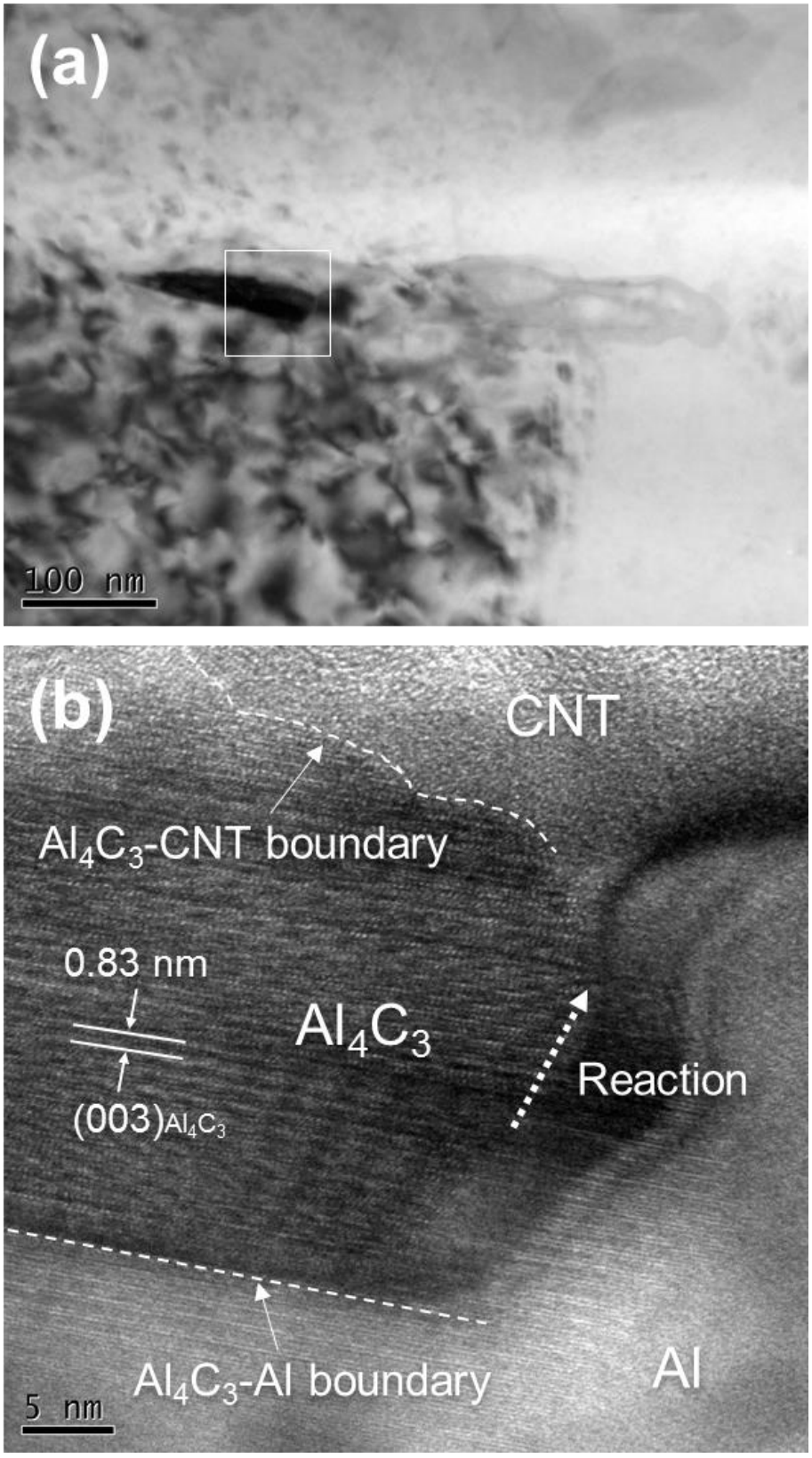

Figure 4-21. High-magnification TEM views on interfacial Al_4C_3 phase in CNT/Al-602^{o}C.

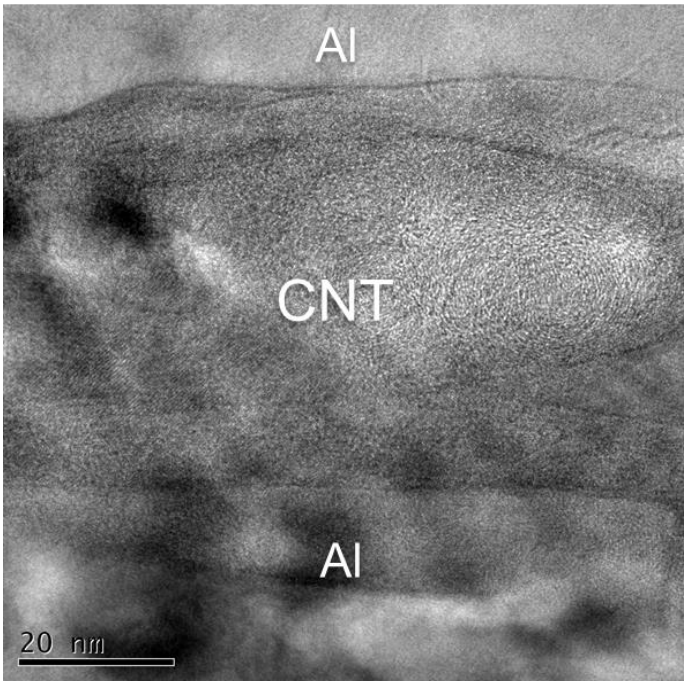

Figure 4-22. High-magnification TEM views on CNT in CNT/Al-602ºC.

As the sintering temperature was increased to 627ºC, large amount of Al_4C_3 formed in AMCs because strong Al_4C_3 peaks were observed in the XRD patterns (Figure 4-14). From the TEM observations (**Figure 4-23**), it was found that some CNTs completely transformed to Al_4C_3 phase. The crystal structure was examined by the SAD patterns (Figure 4-23b). It was noted that the in situ formed Al_4C_3 phase had a large distribution of size from several tens to several hundreds of nanometers. The carbide in Figure 4-23 had a width of ~200 nm and a length of ~500 nm.

Figure 4-24 and **Figure 4-25** show typically tiny Al_4C_3 nanorods with a diameter of ~20 nm, which was similar to that of CNTs. The structural characteristics of the carbides were clearly observed from their SAD patterns (Figure 4-24b and Figure 4-25b) and the HR-TEM view (Figure 4-24c). The diversity of Al_4C_3 size might be attributed to the different sizes of template raw CNTs [20].

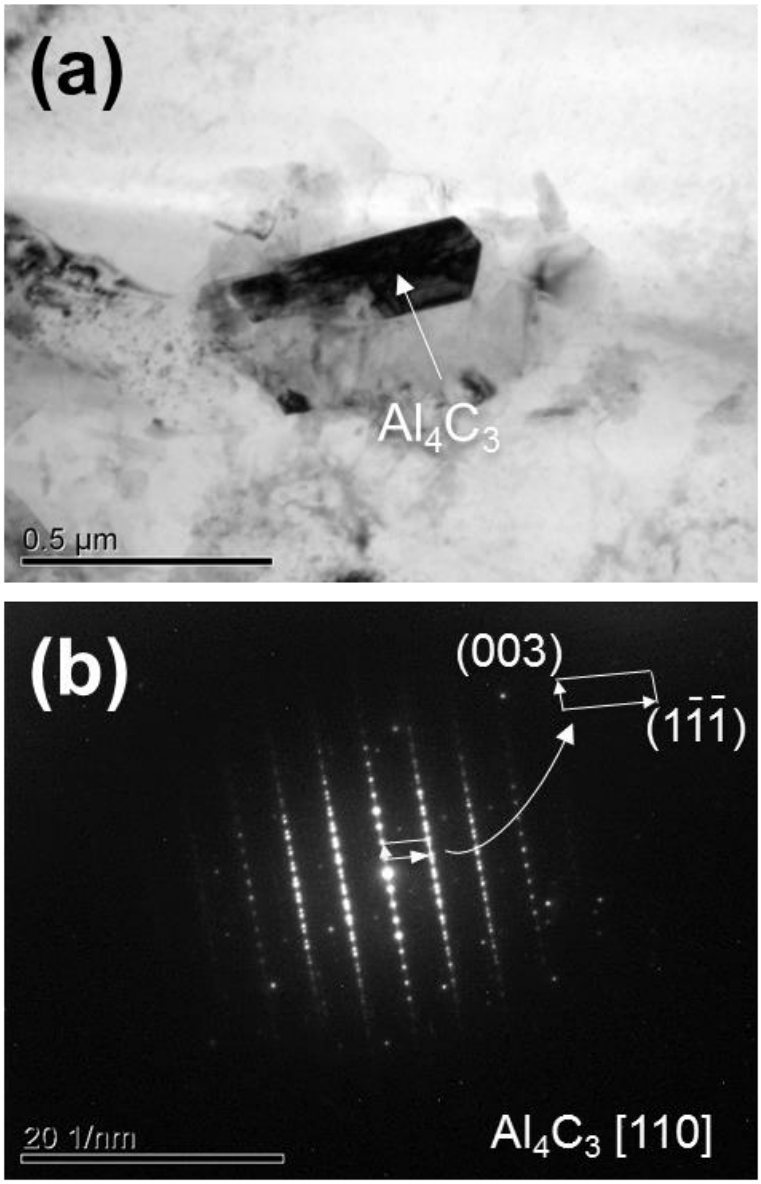

Figure 4-23. TEM views on CNT/Al-627°C. (a) BF-TEM view and (b) SAD patterns.

The configuration of Al_4C_3 shown in Figure 4-24c was similar to the phase observed in the Al-2 wt.% MWCNTs composite reported in [21]. However, the phase was demonstrated differently as a CNT through the BF-TEM image, probably owing to the similar dimension and morphology of Al_4C_3 and CNT. Actually, as revealed in the present study, Al_4C_3 has comparatively black contracts and characteristic stripes with a large distance of 0.83 nm of the (003) planes along the rod-axis [22].

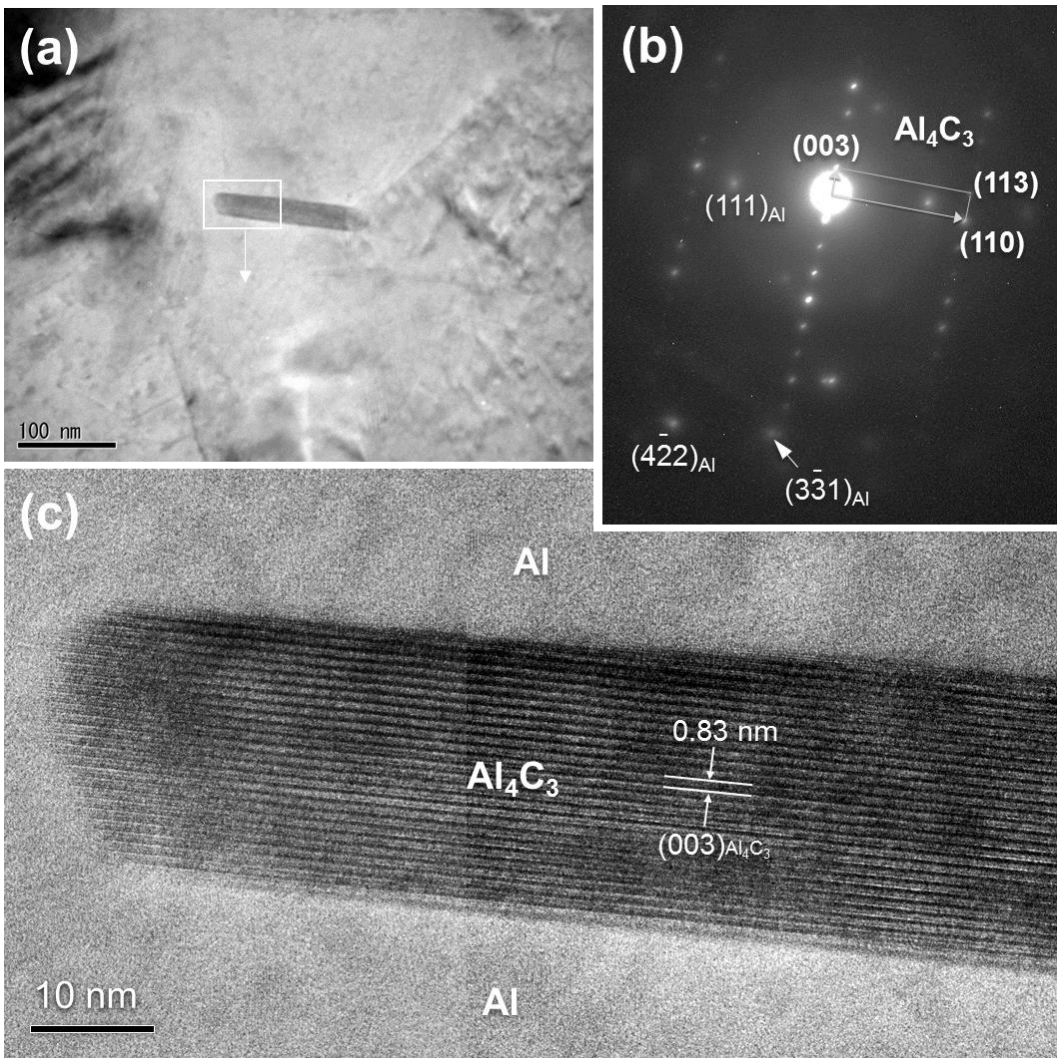

Figure 4-24. TEM views on CNT/Al-627ºC. (a) BF-TEM view, (b) SAD patterns and (c) HR-TEM view on box area in (a).

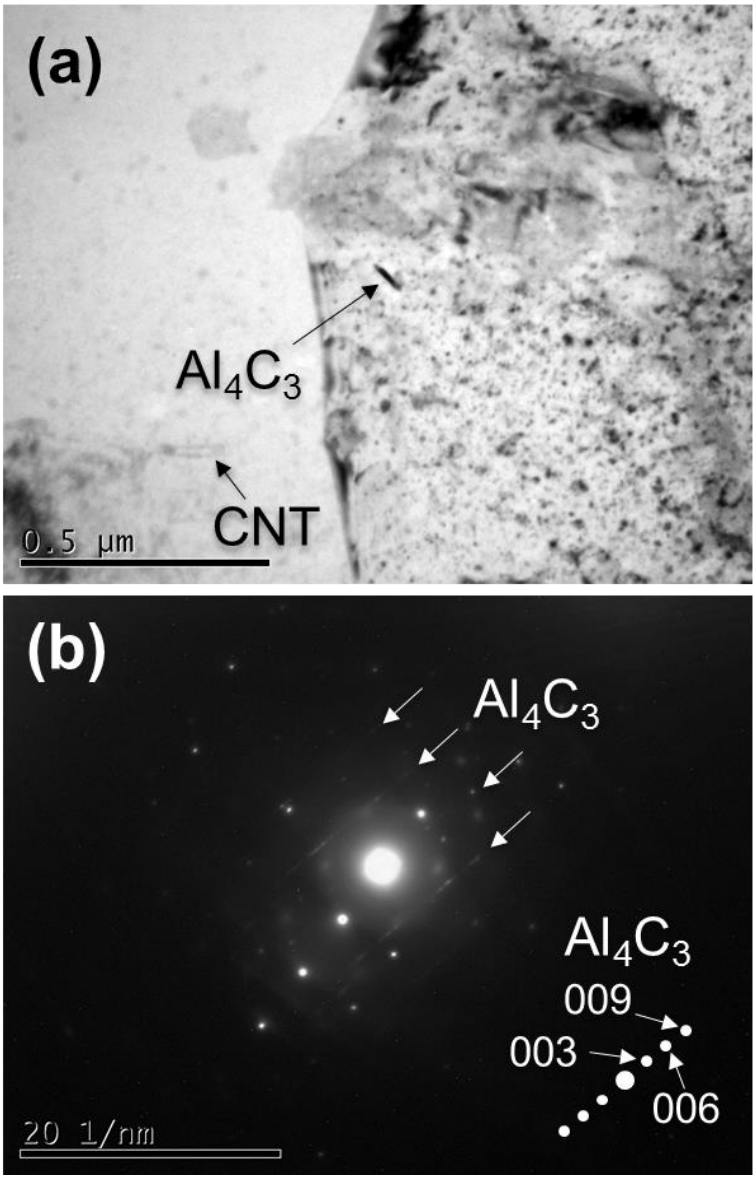

Figure 4-25. TEM views on Al_4C_3 and CNT in CNT/Al-627°C. (a) BF-TEM view and (b) SAD patterns.

Although Al_4C_3 phase was commonly detected in CNT/Al-627°C, remained CNT phases were still observed in Al matrix, as shown in **Figure 4-26**. However, compared with the remained CNTs in the composite processed under lower sintering temperatures (Figure 4-17, Figure 4-18 and Figure 4-21), the detected CNTs in CNT/Al-627°C showed dim structure with faint interfaces, as shown in Figure 4-26a. The CNT walls and Al atom planes were differentiated in the HR-TEM image (Figure 4-26b). However, similar to the CNTs in

CNT/Al-622ºC (Figure 4-21), the regularity of CNT structure was also decreased compared with the raw CNTs (Figure 2-3).

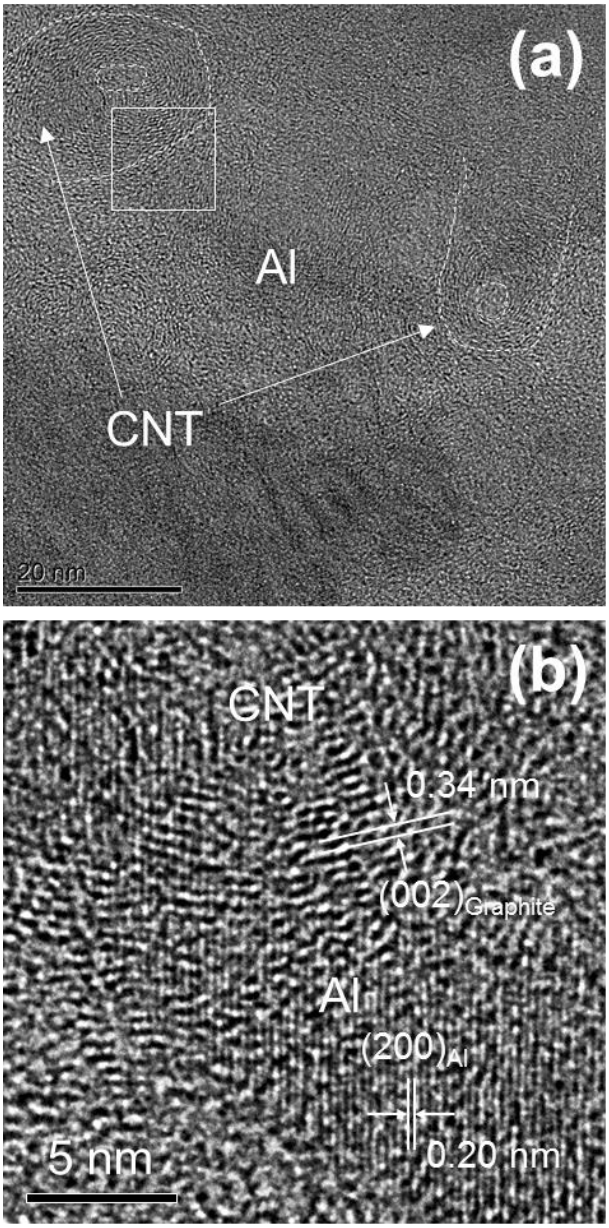

Figure 4-26. High-magnification TEM views on interface between matrix and remained CNTs in CNT/Al-627ºC. (b) shows box area in (a).

4.5 Relationship between strengthening effect and interfacial characteristics

4.5.1 Tensile properties

The yield strength (YS), ultimate tensile strength (UTS) and elongation of pure Al and CNT/Al composites with various SPS temperatures obtained from the tensile tests are shown in **Figure 4-27**. From Figure 4-27a and b, it is seen that the YS and UTS of pure Al was kept at similar values of ~120 MPa and ~170 MPa under SPS temperature from of 427^{o}C to 627^{o}C, respectively. Small strength decrease was observed at 602^{o}C and 627^{o}C for pure Al, reasonably due to the accelerated grain growth at elevated temperatures near the melting point. However, CNT/Al composites showed a distinct tendency in YS and UTS. At low SPS temperatures within 427-527^{o}C, CNT/Al composites had similar YS and UTS of ~130 MPa and ~185 MPa, respectively. From 527^{o}C to 602^{o}C, the YS and UTS of CNT/Al were rapidly increased to 160 MPa and 232 MPa, respectively. As SPS temperature was further increased to 627^{o}C, small decrease of YS and UTS were observed. Therefore, the CNT/Al-602^{o}C had highest YS and UTS.

Different from the situations in YS and UTS, elongation of both pure Al and CNT/Al composites gradually increased with increase in SPS temperature from 427^{o}C to 627^{o}C. At SPS temperature of 602^{o}C and 627^{o}C, CNT/Al composite had high elongations of 17.3% and 20.4%, respectively. It was also seen that before 527^{o}C, the increasing rate of elongation of both pure Al and CNT/Al was small. As SPS temperature was larger than 527^{o}C, the elongation was improved dramatically with increasing SPS temperature. The noticeable change of mechanical properties within 527-627^{o}C could be further examined in the tensile stress-strain curves of pure Al and CNT/Al composites, as shown in **Figure 4-28**. Only one curve is typically shown for each material. The results suggested that there were two critical SPS temperatures (527^{o}C and 602^{o}C) which divided the tensile properties-SPS temperature curves of CNT/Al composites into three stages.

In the first stage with low SPS temperatures (427-527^{o}C), CNT/Al composites had similar mechanical properties (YS, UTS and elongation). In this stage, CNT structure was greatly remained in the composites without interfacial Al_4C_3 phases. In the second stage of medium SPS temperature (527-602^{o}C), both the strength and ductility of CNT/Al composites increased dramatically with increasing SPS temperature. As temperature was increased, the size and amount of interfacial Al_4C_3 phases gradually increased. In the final high SPS temperature stage (over 602^{o}C), the ductility was improved but with decreased YS and UTS.

In this stage, the reaction between CNTs and Al was greatly accelerated that large amount of precipitant Al_4C_3 phases were formed in the matrix. These results suggested that the interfacial Al_4C_3 phases played a dominant role in strengthening the composites.

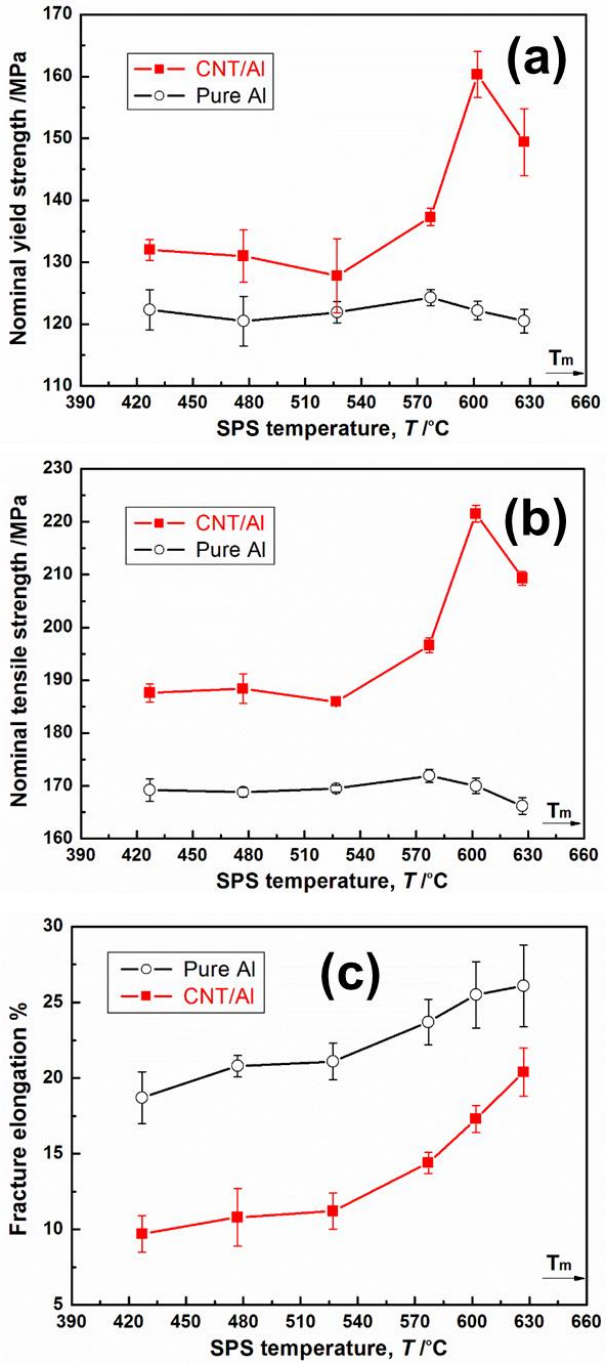

Figure 4-27. Tensile properties of pure Al and CNT/Al composites processed under various SPS temperatures. (a) YS, (b) UTS and (c) Elongation.

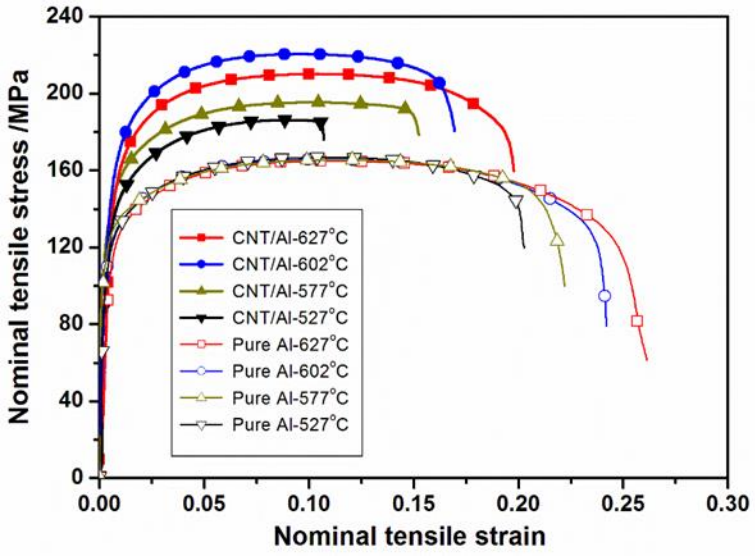

Figure 4-28. Tensile stress-strain curves of pure Al and CNT/Al composites with SPS temperatures from 527ºC to 627ºC.

4.5.2 Strengthening effect of carbon nanotubes

CNT-induced strength improvement in Al matrix might be contributed by possible mechanisms of grain refining and the strengthening of reinforcements (CNTs or Al_4C_3) [23, 24]. The contribution of grain refining to the tensile strength ($\Delta\sigma_{GR}$) could be estimated according to the Hall-Petch formula [25], which is expressed as

$$\Delta\sigma_{GR} = K(d^{-0.5} - d_0^{-0.5}) \qquad \text{(Eq. 4-1)}$$

where d and d_m is respectively the GS of composites and pure Al, and K is a constant (0.04 MPa $m^{0.5}$ for Al [23]). The strength contributions of the reinforcements could be further estimated by subtracting $\Delta\sigma_{GR}$ from the composite strength. The estimated strength contributions in CNT/Al composites are shown in **Figure 4-29**. It was seen that the grain refining only contributed to a small part to the total strength improvement of the composites. The dominant part was ordinated from the strengthening effect of CNTs or Al_4C_3. For example, with CNT/Al-602ºC, the grain refining and the strengthening of reinforcement contributed 2.5 MPa and 48.5 MPa to UTS of CNT/Al composites, respectively. Therefore, the influence of SPS temperature on mechanical strength of the composites was coincident with that on the strengthening effect of reinforcements.

As SPS temperature was increased from 527ºC to 602ºC, the strengthening effect of reinforcements was kept increasing. At 627ºC, the strength contribution of reinforcements (mixing of CNTs and Al_4C_3) was 38.8 MPa, showing 20% reduction compared with CNT/Al-602ºC. These results suggested that the CNTs with partial interfacial Al_4C_3 phases at 602ºC had the maximum strengthening effect in Al matrix.

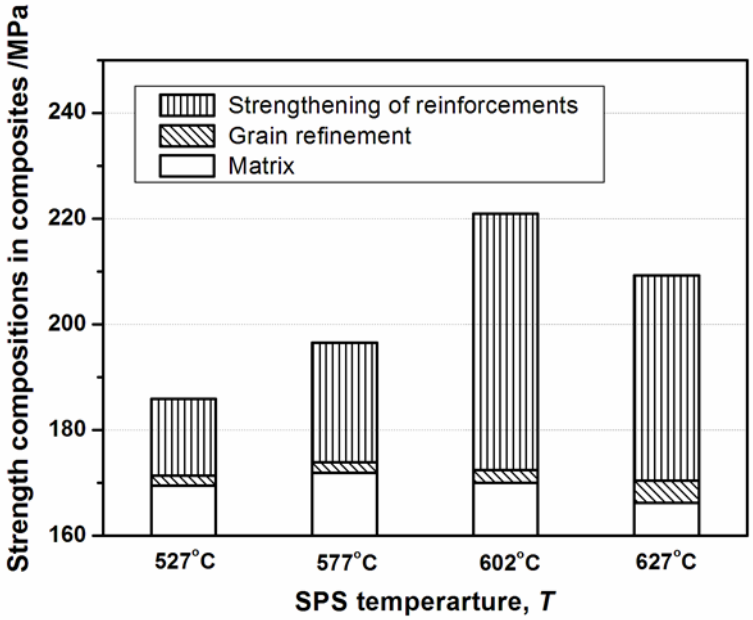

Figure 4-29. Contributions to the UTS of CNT/Al composites with SPS temperatures from 527ºC to 627ºC.

To better understand the SPS temperature-dependent mechanical properties, the failure behaviors of CNTs were studies by examining the fracture morphology of CNT/Al composites sintered under various SPS temperatures, as shown in **Figure 4-30**. At low SPS temperatures of 427ºC and 527ºC, it was clear to observe the phenomenon of Al powder debonding (Figure 4-30a and c) from Al matrix, suggesting the insufficient bonding conditions at Al-Al, which agreed with the observed low EC before 527ºC (Figure 4-10). As revealed in Section 3.1 and Section 3.2, insufficient powder bonding is detrimental for dislocation movement through the powder boundaries, and it might act as initial site to produce micro-cracks, resulting in low ductility of metal materials. Moreover, at the debonded powder boundaries, detached CNTs were observed (Figure 4-30b and d), suggesting comparatively weak interfacial bonding. A weak Al-CNT interface is

disadvantageous for achieving effective load transfer from matrix to CNT [26, 27] and it resulted in low composite strength [13, 28]. Therefore, the three composites SPSed below 527^{o}C exhibited comparatively low ductility and low strength (Figure 4-27).

As ST was improved to 602^{o}C, the fraction of debonded powders was noticeably decreased (Figure 4-30e). Moreover, CNT pull-out was observed as the dominant failure mode of CNTs during tensile failure. It suggested that the bonding conditions of Al-Al powder and CNT-Al interface were simultaneously enhanced from 527^{o}C to 602^{o}C. As SPS temperature was elevated further to 627^{o}C, the fracture surface exhibited ductile failure mode with numerous dimples and plastically deformed powder/grain boundaries (Figure 4-30g). Powder debonding phenomenon was rarely observed on the fracture surface. Pulled-out CNTs (some might be Al_4C_3) was observed as the dominant failure mode of CNTs during tensile failure (Figure 4-30).

It suggested that the reason leading to elongation improvements of pure Al and CNT/Al was that the bonding conditions of Al matrix were enhanced with increasing the SPS temperature. Consequently, the density and EC were increased. Considering the dramatic EC and elongation improvement above 527^{o}C, the temperature at 527^{o}C was regarded as a critical point above which the sintering-induced bonding of powders started to accelerate. At the same time of powder bonding, the diffusion of Al atoms were promoted driven by the improved thermal force at elevated temperatures. Therefore, the chemical reaction between CNTs and Al matrix was improved with the increase of SPS temperature. At 602^{o}C, interfacial Al_4C_3 phases were formed and they locked the remained CNT part in the matrix (Figure 4-21b). As the interfacial bonding condition was improved, the load transfer efficiency from matrix to CNTs was attained to the maximum value during tensile response at 602^{o}C. As the temperature was further increased to 627^{o}C, severe interfacial reaction happened and many CNTs were completely transformed to Al_4C_3 phase. Although the new Al_4C_3 had fine sizes, their fracture strength was much smaller than the CNTs with super-high strength [24, 29]. Therefore, the load transfer effect was decreased, resulting in the degraded tensile strength of CNT/Al composites.

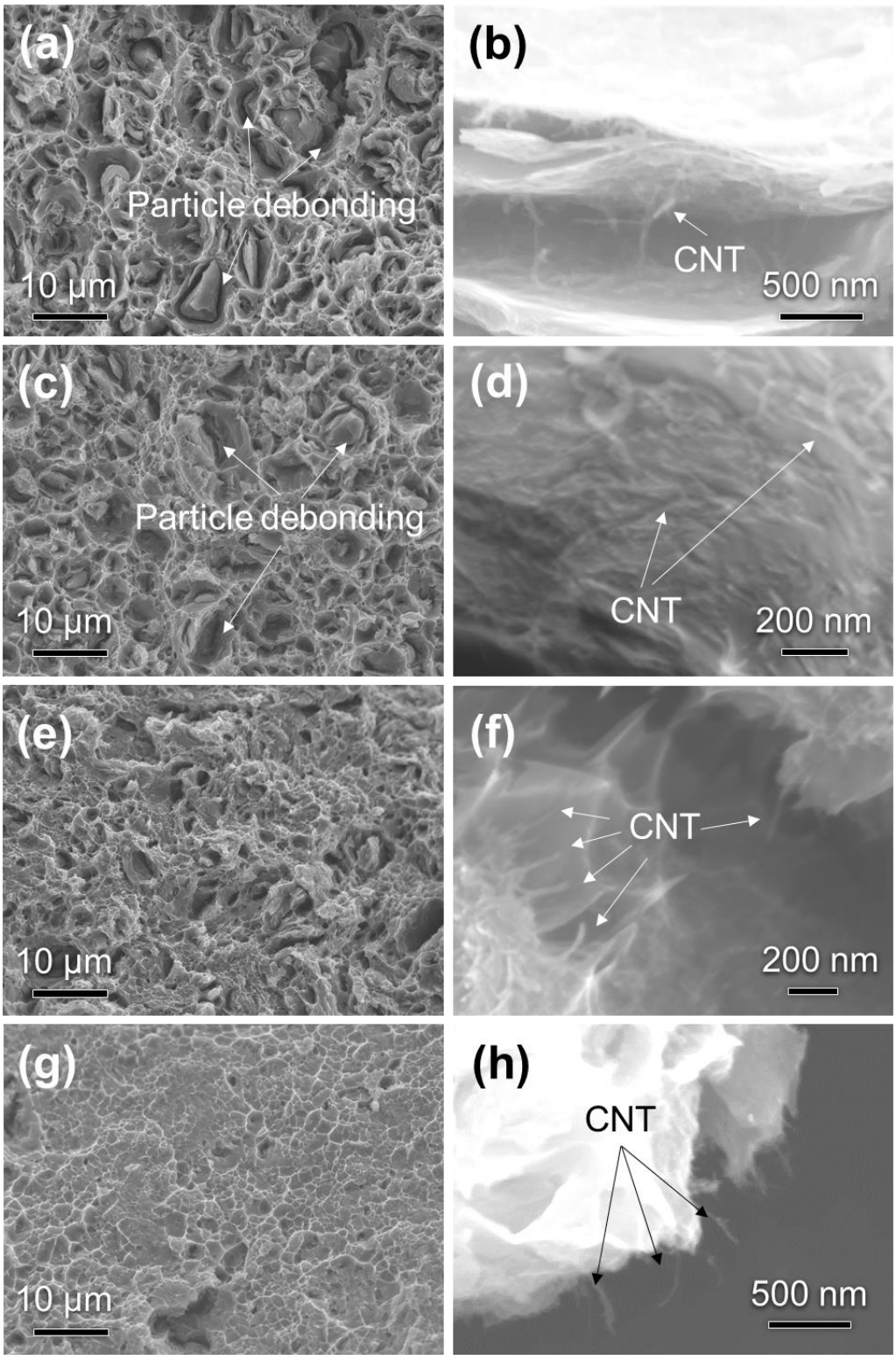

Figure 4-30. Fracture morphologies of CNT/Al composites with SPS temperatures of 427°C (a,b), 527°C (c,d), 602°C (e,f), and 627°C (g,h).

4.6 Conclusions

In this chapter, processing temperature was explored as the experimental valuable to tune interfacial microstructures. Two processing routes, PHT and SPS, were applied to investigate the temperature-dependent interfacial characteristics. PHT-induced cracking phenomenon was described and its formation mechanism was clarified. In SPS, the interfacial characteristics were correlated to the reinforcing effect of CNTs. The main findings can be concluded as below.

(1) Micro-cracks were observed in the powder metallurgy Al and CNT/Al materials experienced SPD and PHT process, resulting in greatly degraded mechanical properties.

(2) As revealed from the in-situ study, micro-cracks formed during the heating-up stage. The release of residual stress in SPD materials was thought responsible for the cracking phenomena during PHT process.

(3) Physical and chemical bonding state of CNT-Al interface generally kept increasing with increasing SPS temperature under the melting point of Al (427-627^{o}C). It led to improved density and EC of as-sintered composites. The ductility of as-extruded composites increased with increasing temperature.

(4) At the low SPS temperature stage (427-527^{o}C), CNTs were found stable in AMCs with trace content of interfacial Al_4C_3 phase. The composites showed similar tensile strength. Debonding of matrix grains and CNT-Al interface were the dominant failure modes.

(5) At the medium SPS stage (527-602^{o}C), the size and amount of interfacial Al_4C_3 phase kept increasing. CNT pull-out was the dominant failure mode.

(6) At 577^{o}C and 602^{o}C, particulate Al_4C_3 phases formed between Al matrix and partially remained CNTs. The Al_4C_3 phase locked the CNT phase in Al matrix. The tensile strength and load transfer efficiency increased with increasing SPS temperature from 527^{o}C to 602^{o}C.

(7) At high SPS temperature of 627^{o}C, mono-crystal Al_4C_3 phase with rod shapes formed in Al matirx. The tensile strength and load transfer effect decreased comparing with the composite sintered at 602^{o}C.

(8) Interfacial characteristics of CNT/Al composites were dependent on processing temperatures. CNTs with partially formed Al_4C_3 might be an optimal structure for highest load transfer efficiency.

References

[1] Foster L, Long G, Hunter M. Reactions Between Aluminum Oxide and Carbon The Al2O3—Al4C3 Phase Diagram. Journal of the American Ceramic Society 1956;39:1-11.
[2] Chen B, Li S, Imai H, Jia L, Umeda J, Takahashi M, et al. Carbon nanotube induced microstructural characteristics in powder metallurgy Al matrix composites and their effects on mechanical and conductive properties. Journal of Alloys and Compounds 2015;651:608-15.
[3] Murakami Y. Metal fatigue: effects of small defects and nonmetallic inclusions: effects of small defects and nonmetallic inclusions: Elsevier; 2002.
[4] Shekhar S, Cai J, Basu S, Abolghasem S, Shankar MR. Effect of strain rate in severe plastic deformation on microstructure refinement and stored energies. Journal of Materials Research 2011;26:395-406.
[5] Sauvage X, Wilde G, Divinski S, Horita Z, Valiev R. Grain boundaries in ultrafine grained materials processed by severe plastic deformation and related phenomena. Materials Science and Engineering: A 2012;540:1-12.
[6] Balog M, Poletti C, Simancik F, Walcher M, Rajner W. The effect of native Al 2 O 3 skin disruption on properties of fine Al powder compacts. Journal of Alloys and Compounds 2011;509:S235-S8.
[7] Liao J, Tan M-J. Mixing of carbon nanotubes (CNTs) and aluminum powder for powder metallurgy use. Powder Technology 2011;208:42-8.
[8] Xie G, Ohashi O, Yoshioka T, Song M, Mitsuishi K, Yasuda H, et al. Effect of Interface Behavior between Particles on Properties of Pure Al Powder Compacts by Spark Plasma Sintering. Materials transactions 2001;42:1846-9.
[9] Saheb N, Iqbal Z, Khalil A, Hakeem AS, Al Aqeeli N, Laoui T, et al. Spark plasma sintering of metals and metal matrix nanocomposites: a review. Journal of Nanomaterials 2012;2012:18.
[10] Jayaganthan R, Brokmeier H-G, Schwebke B, Panigrahi S. Microstructure and texture evolution in cryorolled Al 7075 alloy. Journal of Alloys and Compounds 2010;496:183-8.
[11] Wei H, Li Z, Xiong D-B, Tan Z, Fan G, Qin Z, et al. Towards strong and stiff carbon nanotube-reinforced high-strength aluminum alloy composites through a microlaminated architecture design. Scripta Materialia 2014;75:30-3.
[12] Esawi AMK, Morsi K, Sayed A, Gawad AA, Borah P. Fabrication and properties of dispersed carbon nanotube–aluminum composites. Materials Science and Engineering: A 2009;508:167-73.
[13] Kurita H, Estili M, Kwon H, Miyazaki T, Zhou W, Silvain J-F, et al. Load-bearing contribution of multi-walled carbon nanotubes on tensile response of aluminum. Composites Part A: Applied Science and Manufacturing 2015;68:133-9.
[14] Xu W, Chenchong W, Zhichao Z, Ping L, Yanhua S, Guofu Z. Interfacial microstructure and growth mechanism of Al4C3 in Grf/Al composites fabricated by liquid pressure method. Micron 2014;65:10-4.
[15] Stein J, Lenczowski B, Anglaret E, Fréty N. Influence of the concentration and nature of carbon nanotubes on the mechanical properties of AA5083 aluminium alloy matrix composites. Carbon 2014;77:44-52.
[16] Sun Y, Cui H, Gong L, Chen J, Shen P, Wang C. Field nanoemitter: one-dimension Al 4 C 3 ceramics. Nanoscale 2011;3:2978-82.

[17] Liu ZY, Xu SJ, Xiao BL, Xue P, Wang WG, Ma ZY. Effect of ball-milling time on mechanical properties of carbon nanotubes reinforced aluminum matrix composites. Composites Part A: Applied Science and Manufacturing 2012;43:2161-8.
[18] Tao FF, Salmeron M. In situ studies of chemistry and structure of materials in reactive environments. Science 2011;331:171-4.
[19] Ci L, Ryu Z, Jin-Phillipp NY, Rühle M. Investigation of the interfacial reaction between multi-walled carbon nanotubes and aluminum. Acta Materialia 2006;54:5367-75.
[20] He CN, Zhao NQ, Shi CS, Song SZ. Fabrication of aluminum carbide nanowires by a nano-template reaction. Carbon 2010;48:931-8.
[21] Pérez-Bustamante R, Gómez-Esparza CD, Estrada-Guel I, Miki-Yoshida M, Licea-Jiménez L, Pérez-García SA, et al. Microstructural and mechanical characterization of Al–MWCNT composites produced by mechanical milling. Materials Science and Engineering: A 2009;502:159-63.
[22] Chen B, Jia L, Li S, Imai H, Takahashi M, Kondoh K. In Situ Synthesized Al4C3Nanorods with Excellent Strengthening Effect in Aluminum Matrix Composites. Advanced Engineering Materials 2014;16:972-5.
[23] Nam DH, Cha SI, Lim BK, Park HM, Han DS, Hong SH. Synergistic strengthening by load transfer mechanism and grain refinement of CNT/Al–Cu composites. Carbon 2012;50:2417-23.
[24] Tjong SC. Recent progress in the development and properties of novel metal matrix nanocomposites reinforced with carbon nanotubes and graphene nanosheets. Materials Science and Engineering: R: Reports 2013;74:281-350.
[25] Hansen N. Hall–Petch relation and boundary strengthening. Scripta Materialia 2004;51:801-6.
[26] Kelley A, Tyson W. Tensile Properties of Fiber-Reinforced Metals. Journal of Mechanical and Physical Solids 1965;13:329-50.
[27] Cox H. The elasticity and strength of paper and other fibrous materials. British journal of applied physics 1952;3:72.
[28] Fan G, Yu Z, Tan Z, Li Z, Zhang D. Evolution, Control, and Effects of Interface in CNT/Al Composites: a Review. Acta Metallurgica Sinica (English Letters) 2014;27:839-43.
[29] Lee C, Wei X, Kysar JW, Hone J. Measurement of the elastic properties and intrinsic strength of monolayer graphene. Science 2008;321:385-8.

Chapter 5
Load Transfer Strengthening in Carbon Nanotube Reinforced Al Matrix Composites

In this chapter, *in-situ* observation of tensile tests were performed to investigate the failure behaviors and strengthening mechanisms of multi-walled carbon nanotubes (MWCNTs) in Al matrix composites (AMCs). To investigate the structure of CNTs in composites before tensile test, the dispersion, size and alignment of carbon nanotubes (CNTs) were characterized. The diameter and length were quantitatively counted to estimate the aspect ratio, which was a significant parameter influencing the load transfer effect. The structural stability and interfacial characteristics were studied by X-ray diffraction, Raman spectrum and TEM. The structure evolution of CNTs during the processing were described.

To record possible CNT failure phenomena during the *in-situ* tensile test, the fracture morphology was kept watching on the composite specimen under low magnifications. The displacement or strain of tensile specimens was manually stopped at serval stages to capture high-magnification images. The corresponding failure modes of CNTs were examined at each stages throughout the tensile test. The detailed fracture process of MWCNTs were described. The possible mechanisms of breaking and peeling of MWCNTs were explored. The failure behavior of Al matrix was also investigated.

To accurately characterize the mechanical properties, regular tensile tests were applied. The fracture morphologies of the two kinds of tensile tests were compared. Based on the examinations of CNT failure modes and mechanical properties, the possible strengthening mechanisms in CNT/Al composites were quantitatively characterized based on the strengthening theories. To reveal the grain-related strengthening effects, the grain information of pure Al and CNT/Al composites was characterized by EBSD. The dispersion strengthening and load transfer strengthening were estimated and discussed. Owing to the dominant strengthening effect of load transfer, the relation between the strengthening efficiency and interfacial strength under different failure modes of CNTs was set up using Kelly-Tyson’s shear-lag theory.

5.1 Structure evolution of carbon nanotubes in composites

5.1.1 Carbon nanotube dispersion

The microstructures of CNTs in CNT-Al powder mixture and the CNT/Al composite are shown in **Figure 5-1**. After the low energy blending (LEB) process, there was minor shape change of Al powder particles (Figure 5-1a and b), comparing with the raw course Al powder (Figure 2-1a and b). Uniformly dispersed CNTs were found on the Al powder surface (Figure 5-1b and c). Possible CNT clusters were observed on the grooves of the Al powder particles. Comparing with the fine CNT and fine Al powder mixture dispersed by the same LEB process (Figure 3-2), the CNT dispersion was improved greatly. It is because the morphology and diameter of raw CNT had great influence on the dispersion effect [1, 2]. CNTs with a large diameter and straight shape used in this chapter would be easier to disperse uniformly in Al matrix. Moreover, the decreased CNT content (from 1.0 wt.% to 0.6 wt.%) might also contribute to the improvement of CNT dispersion [3]. Considering the fact that structural parameters affected the reinforcing effect of CNTs [4], the average length (L) and diameter of CNTs were quantitatively measured as 9.2±3.7 μm and 125±32 nm, respectively, from 100 CNTs. Figure 5-1d shows the distribution of L.

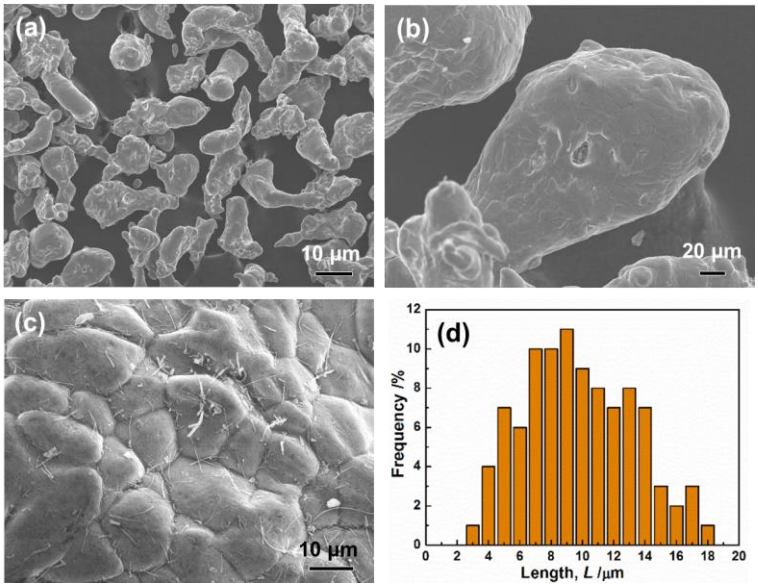

Figure 5-1. CNT dispersion in the CNT-Al powder mixed by low energy blending process. (a-c) Morphologies of CNTs at different magnifications and (d) Length distribution of CNTs.

5.1.2 Carbon nanotube alignment

After consolidation, both reference Al and CNT/Al composite showed high relative density over 99%. **Figure 5-2** shows the microstructure of extruded CNT/Al composite. In the extruded composite which was deeply etched, the primary particle boundaries (PPBs, defined as the grain boundaries originated from the initial powder surface) were revealed between elongated Al particles (Figure 5-2a). CNTs were found siting at PPBs. Figure 5-2b typically shows an exposed CNT which located at the PPB. No large CNT agglomeration was observed. Because the PPBs aligned along the extrusion direction, the long CNTs within the boundaries also took to this orientation (Figure 5-2b). Many etch pits were also observed in Al matrix and at the CNT-Al interface owing to the deep etching process.

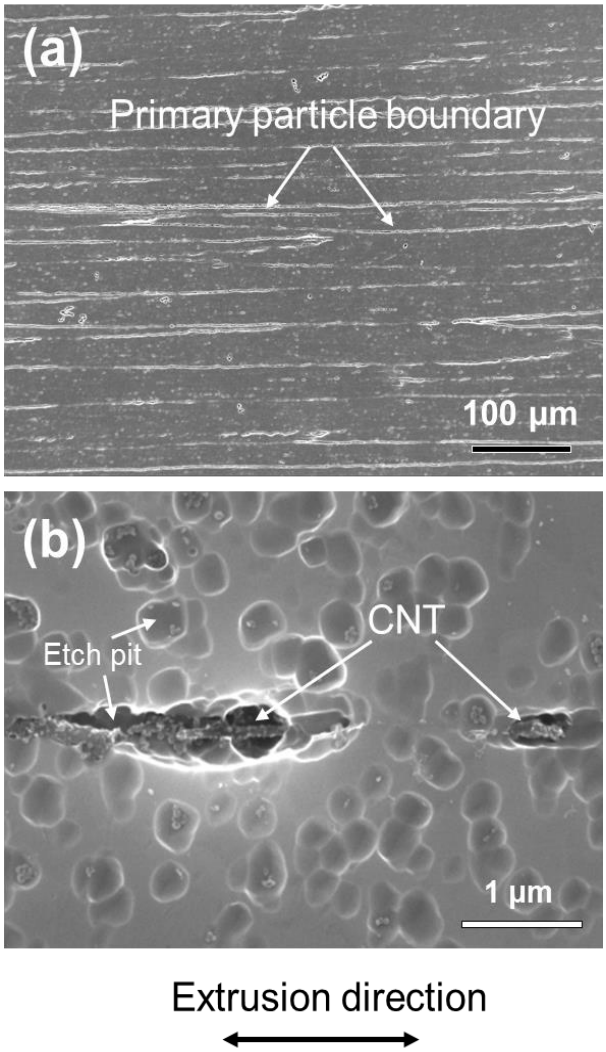

Figure 5-2. CNT alignment in extruded CNT/Al composite at different magnifications.

5.1.3 Structural stability

The XRD patterns of processed materials are shown in **Figure 5-3**a. Only Al peaks are observed in the CNT/Al composite during processing. The intensity of Al(111) planes was increased after hot-extrusion comparing to the as-sintered sample, owing to the crystalline rotation during the extrusion process [5]. It is known that the <111> tensile direction is a strong orientation for face centered cubic (FCC) materials (such as Al and Cu) with classical {111}<110> slip systems [8]. Therefore, the <111> oriented grains were helpful to increase the tensile strength. Absence of the peeks corresponding to CNTs might be due to their fine size and small content.

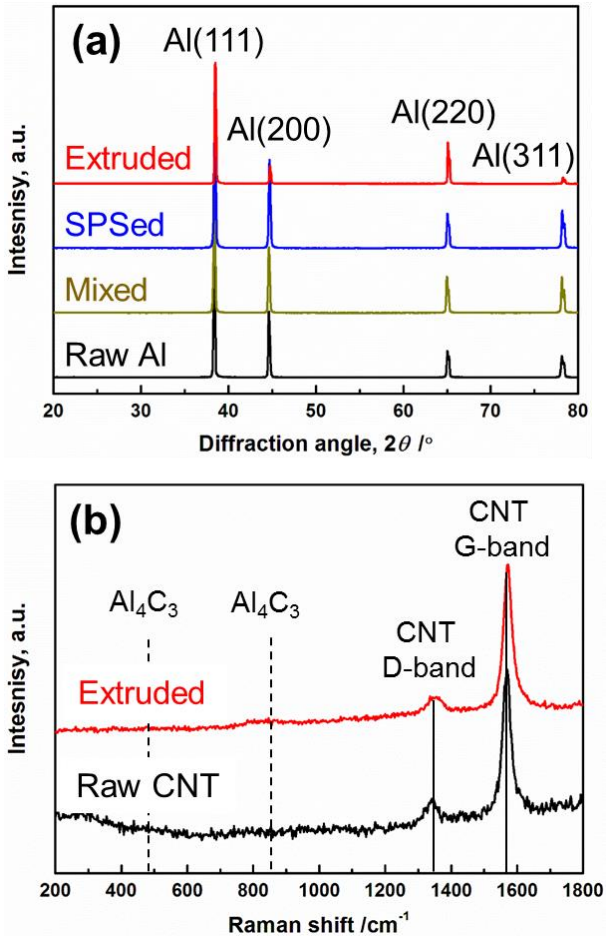

Figure 5-3. XRD spectra (a) and Raman spectra (b) of raw Al powder (Raw Al), raw CNT powder (raw CNT), mixed CNT-Al powder (Mixed), SPSed CNT/Al composite (SPSed), and extruded CNT/Al composite (Extruded). Test surface specimen of composites is vertical to incident wave beams.

Raman analysis has been used for characterizing carbon-related nano-reinforcements, with CNT damage-band (D-band) near 1350 cm^{-1} and CNT graphite-band (G-band) near 1590 cm^{-1} [5-9], and Al_4C_3 bands near 490 cm^{-1} and 855 cm^{-1} [10]. The intensity ratio between D-band and G-band (I_D/I_G) provides the defect conditions of CNTs [11]. The Raman spectra of processed materials are shown Figure 5-3b. A noticeable increase of I_D/I_G has been observed in CNT-Al powder mixture after high energy ball milling owing to the high loads applied on CNTs during milling (Figure 3-16). However, in the present CNT/Al composite, no obvious intensity change happened to I_D/I_G (around 0.1, Figure 5-3b), which suggested little structural damage of CNTs through the used PM route. Moreover, no peak corresponding to Al_4C_3 was observed in the Raman spectra of CNT/Al composite (Fig. 5-3b), suggesting the absence or very few contents of Al_4C_3 phase in the present CNT/Al composite sintered under a comparably low SPS temperature.

Figure 5-4 shows the morphology of MWCNT incorporated in AMCs. CNT and Al phases were identified by the selected area diffraction (SAD) patterns as shown in the insets of Figure 5-4a and b. It was observed that CNT contacted well with Al matrix via a clean interface, and no other phase was at the interface (Figure 5-4a and b). It suggested that CNTs were stable in the present processing conditions.

Moreover, some irregular structures or defects were observed inside the MWCNT, as arrows indicated in Figure 5-4b. A typical defect consisting of ~30 walls (the frame in Figure 5-4b) is shown in Figure 5-4c. These walls were non-parallel to the axis direction and exhibited as bridging walls to cross-line with other walls, which were schematically shown in Figure 5-4d. This structure defect was reasonably originated from the raw MWCNTs, owing to the good stability of CNTs during processing.

Figure 5-5 shows the observed bridging walls in the raw MWCNT. These defective walls (non-parallel to CNT axis) exhibited as bridges that cross-linked the adjacent regular walls (parallel to the axis). Existence of bridging walls might be related to the fact that the present CVD grown CNTs had a comparably high structure-defect density than that of arc-grown CNTs [12]. Cross-linked imperfections were reported to degrade the CNT strength but improve the inter-wall bonding strength [13].

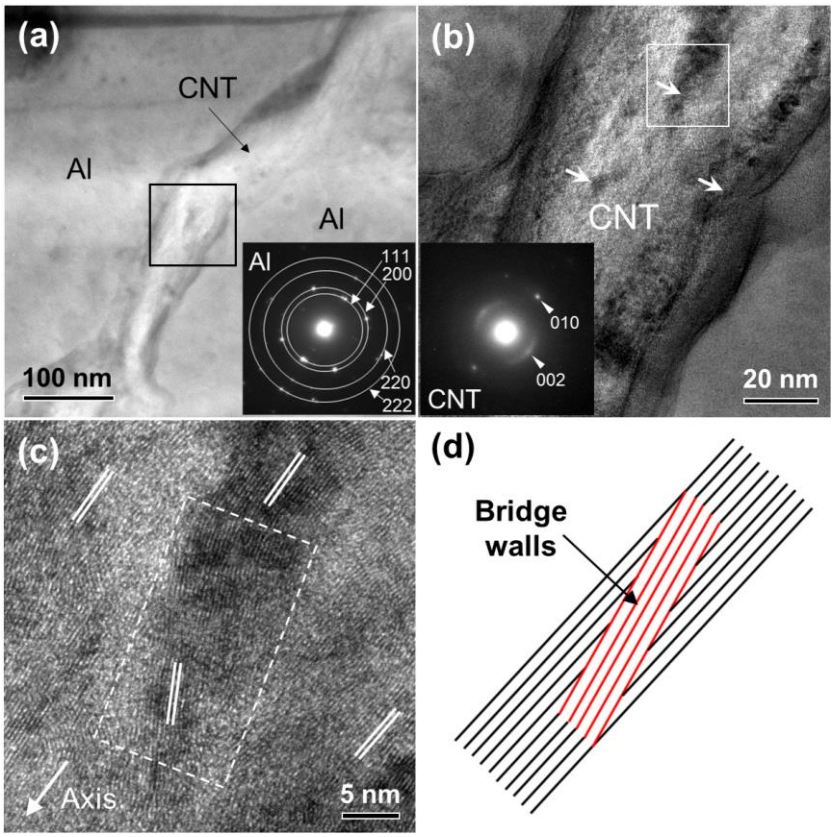

Figure 5-4. Morphology of a MWCNT dispersed in AMCs by TEM observation at different magnifications. (b) and (c) shows box in (a) and (b), respectively. Double-lines in (c) suggest the aligning direction of walls. (d) schematically shows the bridge walls in the frame in (c).

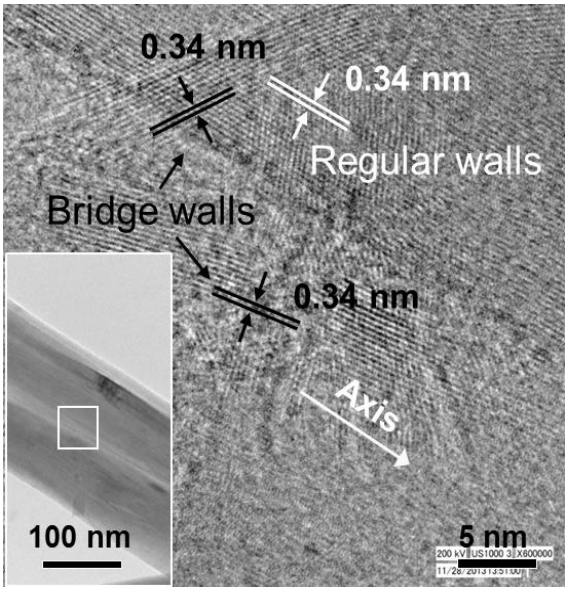

Figure 5-5. Typical bridge walls in raw MWCNTs. Inset shows a low-magnification view.

5.2 In-situ observations on deformation of CNT/Al composites

5.2.1 Yielding stage in tensile test

To control the fracture position of the CNT/Al composite during the in-situ tensile test, a groove precut was made artificially on the machined specimen, as shown in **Figure 5-6**a. Through this way, SEM observations could be focused on the precut area to capture the failure behaviors of CNTs. As the tensile test was manually paused during the test (as the position A-F indicated in Figure 5-6b), the displacement was sustained and high-quality SEM photos were captured. Tensile loading was then restarted to next pause points until the sample fractured.

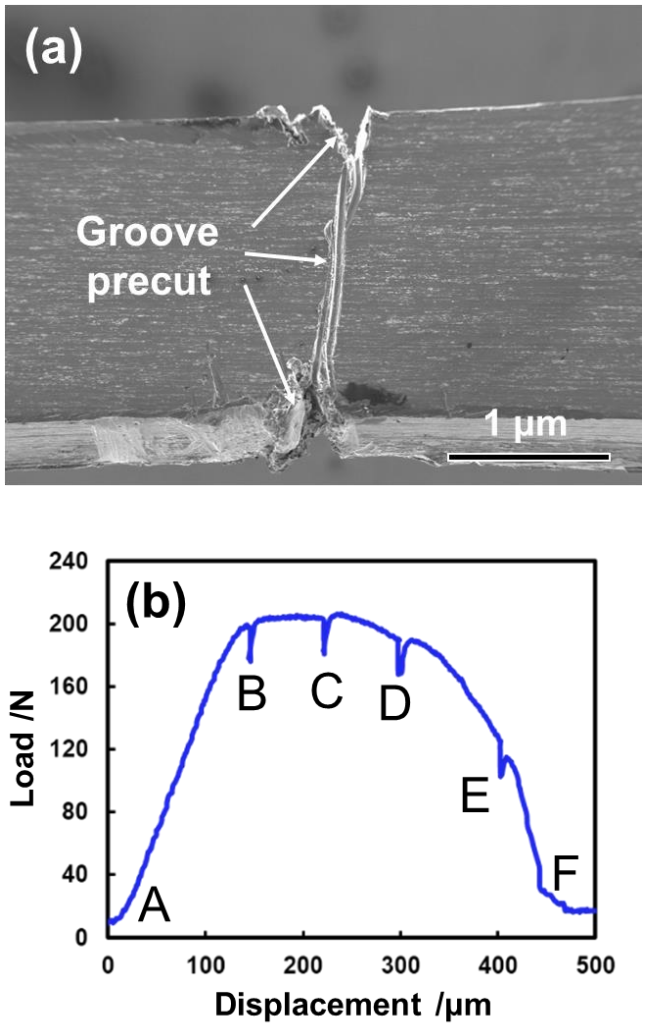

Figure 5-6. Morphology of specimen surface with groove precuts (a) and recorded load-displacement curve of the in-situ test.

Figure 5-7 shows the microstructure evolution of CNT/Al composite within the yielding stage. At the initial state (Figure 5-7a and b, as Point A indicated in Figure 5-6b), a kind of worn feature was observed inside the groove precut owing the scratching process. At the approximate yielding point (Figure 5-7c and d), no obvious microstructure change was observed comparing with the initial state (Figure 5-7a and b). The dimension increase of some pores in the precut (as circles indicated in Figure 5-7a and c) was reasonably due to the deformation under the tensile displacement (~150 μm for the entire specimen, Figure 5-6b).

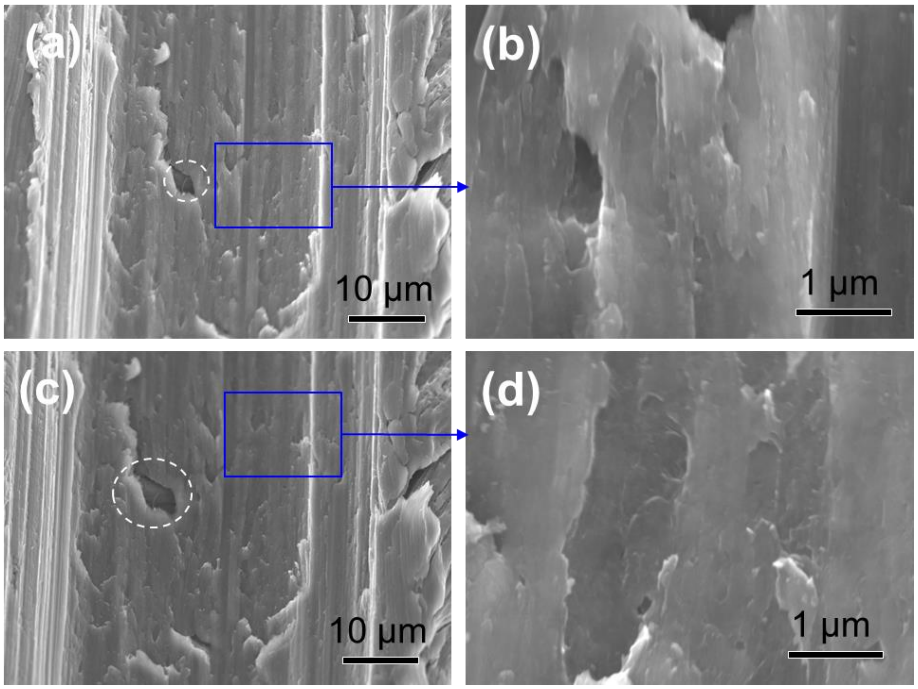

Figure 5-7. Microstructure of CNT/Al composite within the yielding stage. (a, b) Initial state (as Point A indicated in Figure 5-6b). (c, d) Approximate yielding point (as Point B indicated in Figure 5-6b).

5.2.2 Plastic-deforming stage

It was the precut area of the composite where micro-cracks were initially produced (**Figure 5-8**). It was reasonably due to the reduced cross-section area and structural irregularity in the precut. Then the cracks grew in the precut. Figure 5-8b shows a typical crack with a width in sub-micrometers. As the cracks expanded to CNTs (**Figure 5-9**), CNTs seemed to act like bridges that restrained the growth of the crack. Xia et al. [14] also

observed the CNT bridging phenomenon in CNT/ceramic composites during crack propagation. CNT bridging was claimed as one main toughening mechanism due to the suppression of crack growth. It was thus believed that CNTs were beneficial to improve the composite toughness.

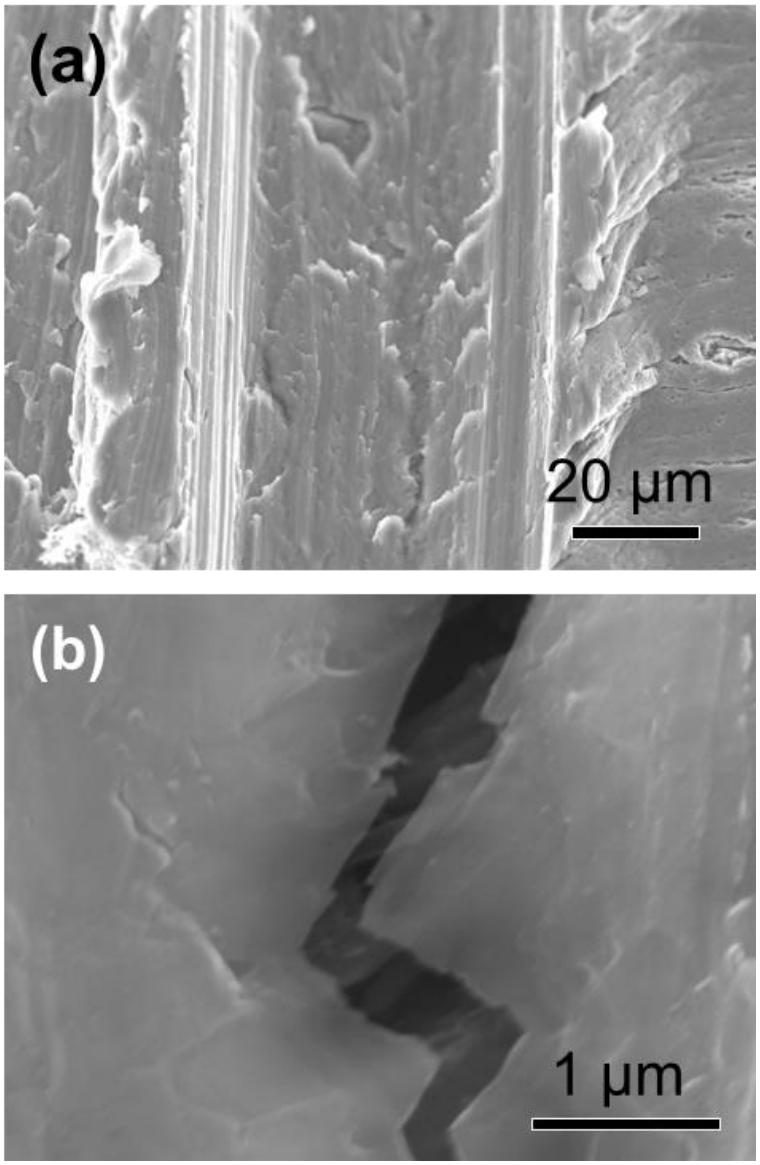

Figure 5-8. Microstructure of CNT/Al composite during the plastic-deforming stage as Point C indicated in Figure 5-6b.

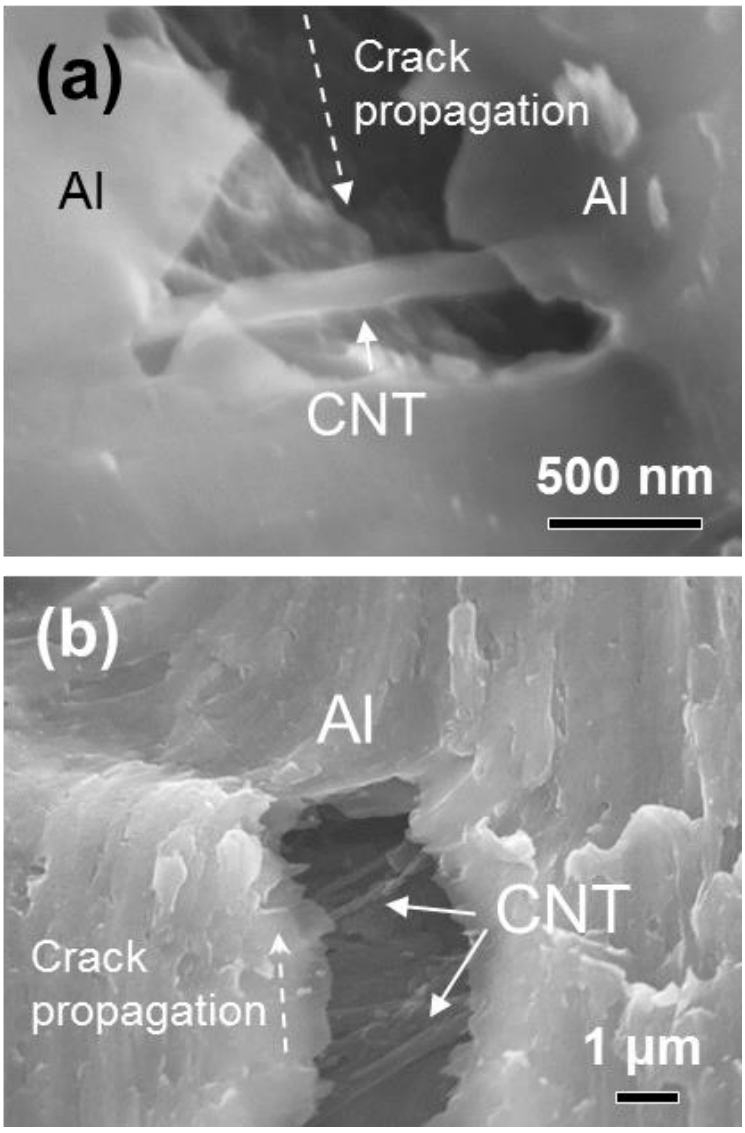

Figure 5-9. Cracks confront CNTs during plastic-deforming stage as Point C indicated in Figure 5-6b.

As the tensile displacement was increased, the CNT bridges started to fracture one by one (**Figure 5-10**). Just at the moment shown in Figure 5-10a, it was observed that the CNT denoted as ① has broken into two parts with all walls fractured, leaving two vertical breaking surfaces. Meanwhile, CNT ② and CNT ③ were experiencing the fracturing moment. From the high-magnification image (Figure 5-10b), it was clearly observed that the outer walls of CNT ② have fractured and some wall debris existed on the broken area. The

fresh inner wall of CNT ② was exposed with a decreased outer-diameter (as the arrow indicated in Figure 5-10b).

Fracturing from outermost part, a significant characteristic of fibrous reinforcements under effective load transfer has been confirmed by some theoretical simulations [15]. However, it was rarely observed in previous studies. According to the shear-lag model set up by Cox [16], it was assumed that the applied load was transferred from matrix to fibrous reinforcements via an interfacial stress along the fiber surface. It indicated that the outermost wall of MWCNT contacted to the interface was firstly loaded and fractured under tensile load. Therefore, the observed fracture behavior that initially started at the outermost-wall supported the interfacial stress assumption of load transfer models.

Spontaneously, CNT ③ is experiencing a kind of multiple peeling fracture process with several fractured stages. From the outer-diameter gradient of the left CNT segment (as arrows indicated with CNT ③ in Figure 5-10b), it indicated that CNT ③ also initially fractured at the outer layer, and the wall-breaking grew from outer walls to the inner walls under the load transferred between CNT walls. Then the fracture position axially shifted to another position on the CNT wall. The peeling behavior will move on until all the walls are fractured. Multi-wall peeling was occasionally observed by other studies on the fractured surface of CNT/MMCs composites after tensile tests [17, 18]. This interesting phenomenon was also attributed to the effective load transfer between CNT walls. As a stress is transferred to an inner wall of the CNT longer than a critical length [16], stresses at the middle regions far from the two ends, may have reached the fracture strength. In this case, the crack advance inside CNTs will shift longitudinally to the weakest point and lead to the peeling phenomenon. Otherwise, if defects are uniformly distributed in CNT, the crack advance will vertically go through the CNT under momentum of the crack front, producing only one fracture plane, as CNT ① exhibited (Fig. 6b).

In a theoretically perfect or low-defect-density MWCNT, stress transferred from the outermost wall to inner walls is quite small [19] because of the weak Van Der Waals bonding between adjacent walls and thus CNTs exhibited a unique failure mode of outermost-wall fracture and inner wall sliding. Oppositely, irregular walls originated from raw MWCNTs might cross-link many adjacent walls together (Fig. 3d and Fig. 5b), and greatly enhanced the inter-wall bonding, which has been proved by the previous studies [13]. Thus effective inter-

wall bonding led to the consequent effective load transfer between walls and the observed CNT fracture. This observation provided direct and compelling evidence for the load transfer strengthening mechanism of MWCNTs in MMCs.

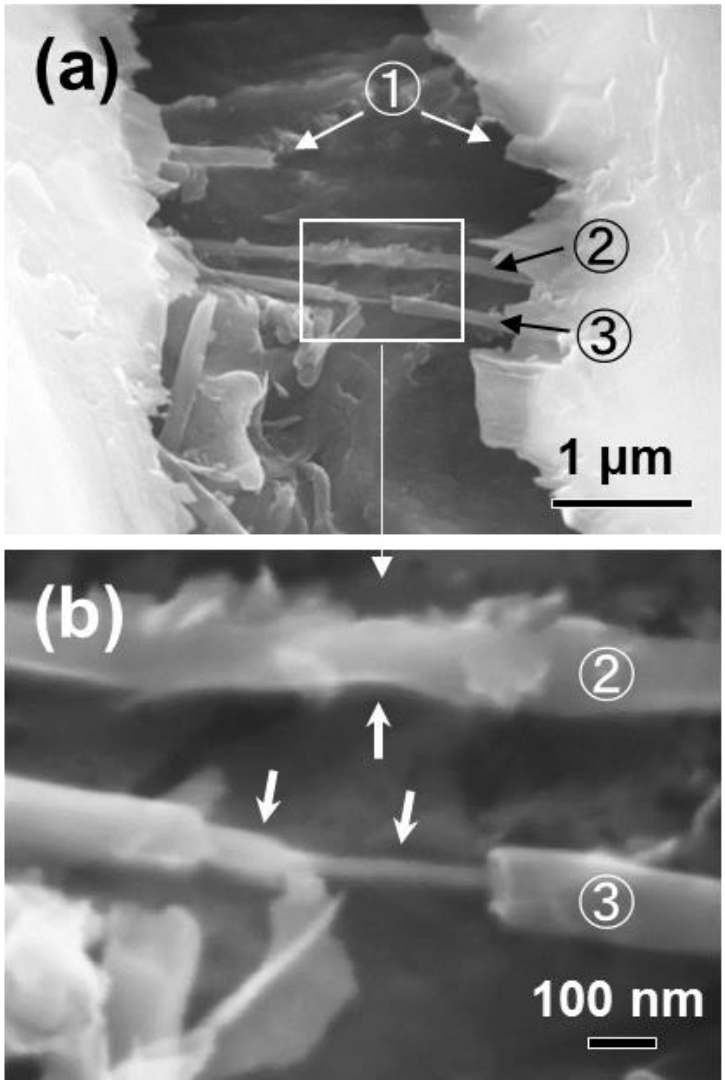

Figure 5-10. CNTs are failing during plastic-deforming stage as Point D indicated in Figure 5-6b.

Actually, the peeling phenomenon was commonly observed during the tensile test. **Figure 5-11** shows another two ruptured CNTs. CNT ④ showed the morphology of only one-time peeling and CNT ⑤ exhibited a multiple peeling (similar with CNT ③ Figure 5-10b). Moreover, at the peeling positions, peeling slopes with gradually changed CNT outer-

diameter were often observed as arrows indicated in Figure 5-10b. With CNT ⑤, there was a long slope between the two stages with outer-diameter of ~230 nm and ~50 nm. The morphology scheme of CNT ⑤ is shown in Figure 5-11c. The existence of peeling slopes suggested that wall fracturing was transferred from outer to inner walls through the bonding structure between walls. These structures, which were non-parallel to the axis direction, were induced by the bridging walls observed in MWCNTs (Figure 5-4 and Figure 5-5).

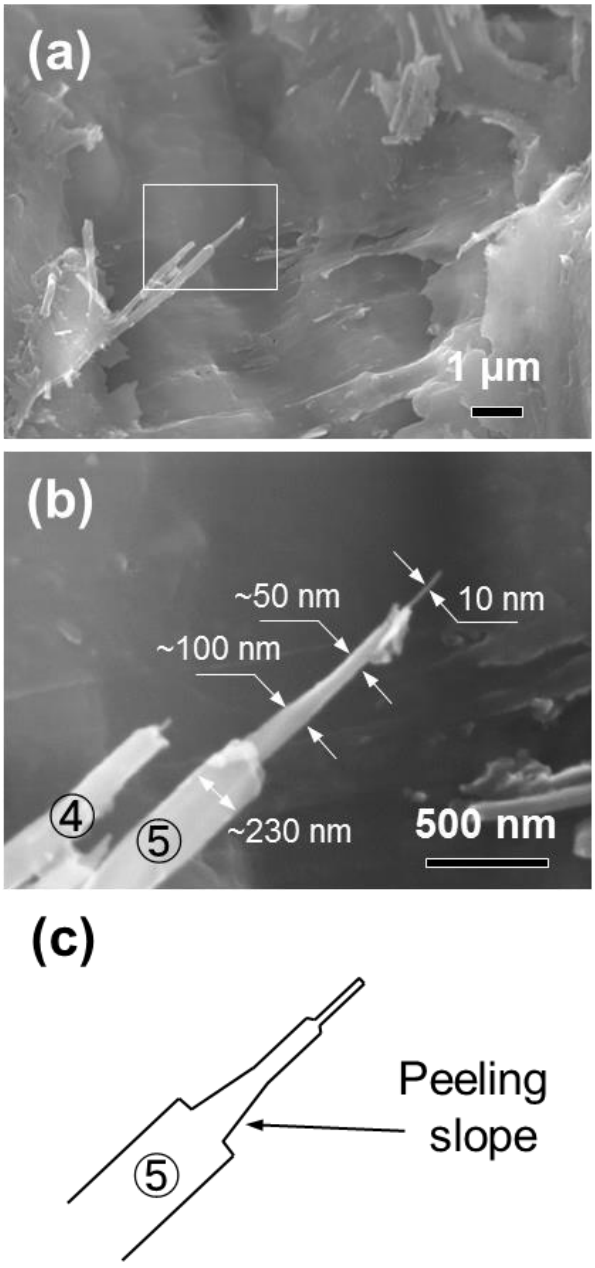

Figure 5-11. Peeled CNTs during plastic-deforming stage as Point E indicated in Figure 5-6b.

5.2.3 Failure state

At the end of tensile test, ruptured CNTs were observed on the fracture surface of the composite (**Figure 5-12**a). A peeled CNT (denoted as CNT ⑥) was also observed, as shown in Figure 5-12b. Similar with CNT ④ (Figure 5-11b), CNT ⑥ also showed one-time peeling morphology with a clear transition slope as an arrow indicated in Figure 5-12b. The morphology scheme of CNT ⑥ is shown in Figure 5-12c.

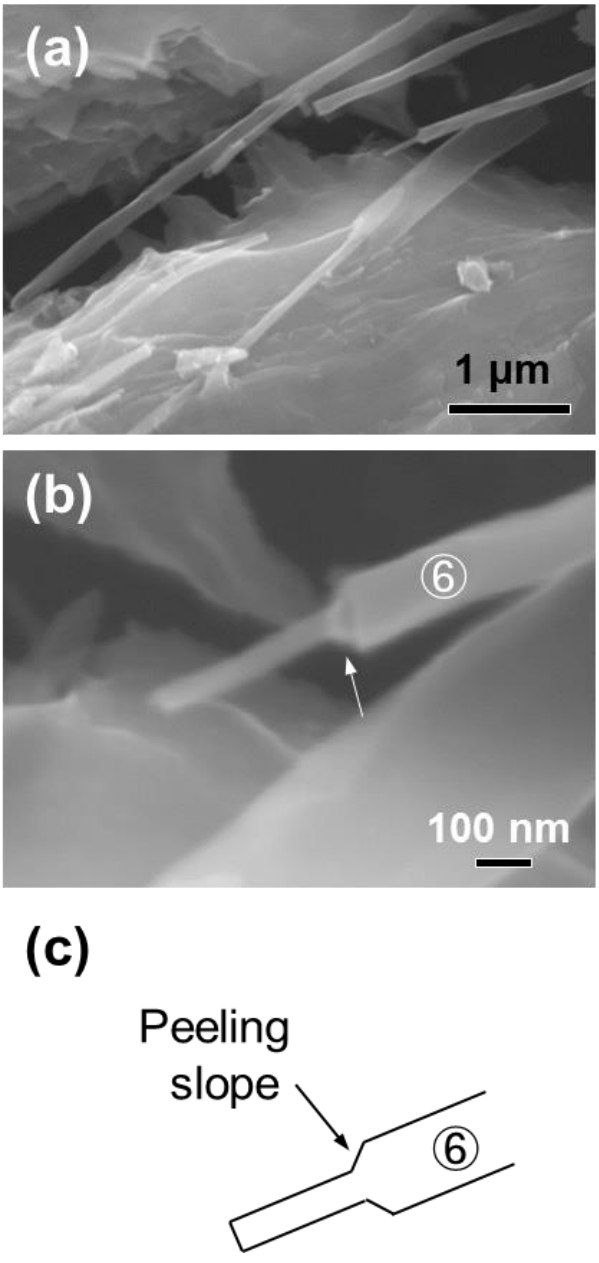

Figure 5-12. Fractured CNTs after tensile test as Point F indicated in Figure 5-6b.

After the tensile test, the low-magnification views of the specimen are shown in **Figure 5-13**. The size of the precut (Figure 5-13a) increased largely comparing with its initial state (Figure 5-6a). The main failure crack went through part of the groove precut. Moreover, many shear bands were observed in the specimen with ~45 ° to the tensile direction near the crack (Figure 5-13b). Such kind of feature was related to the characteristic deformation behavior of metal materials that crystals tended to slide along the preferable direction with 45 °to the tensile axis [20].

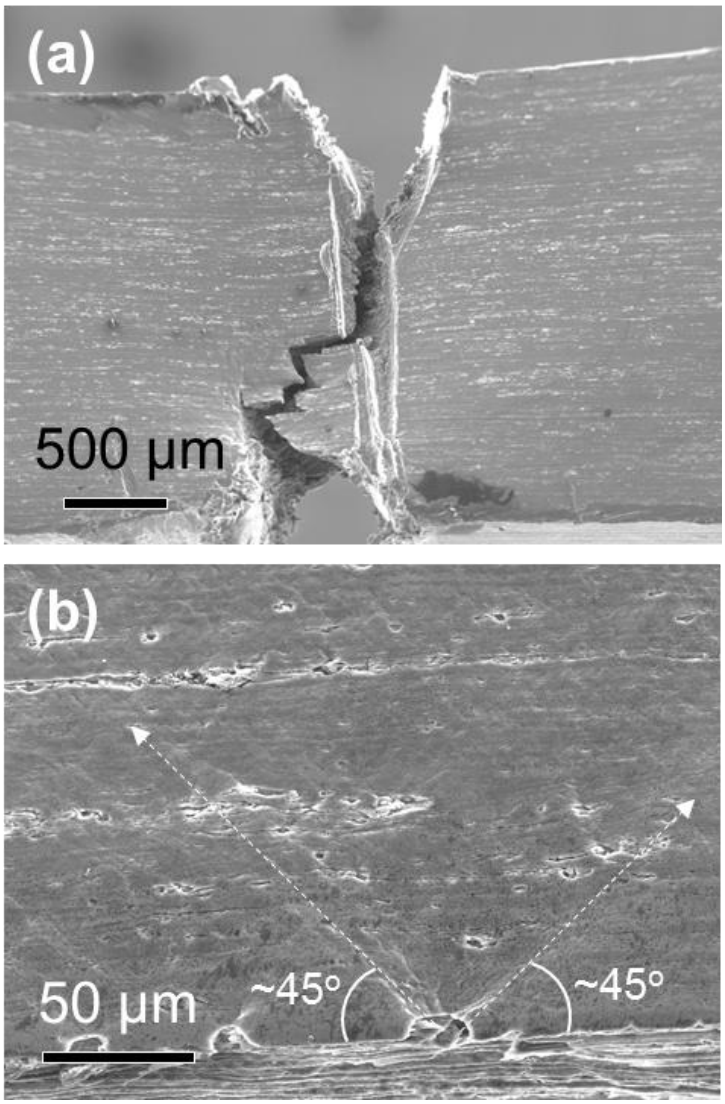

Figure 5-13. Microstructures of CNT/Al composite after failure as Point F indicated in Figure 5-6b.

5.3 Regular tensile test on carbon nanotube/Al composites

5.3.1 Strengthening effect of carbon nanotubes

Since the precut was made on the in-situ tensile specimen, the obtained mechanical properties from the test were not accurate (exactly smaller). The 0.2% offset yield strength (YS) and ultimate tensile strength (UTS) of pure Al were measured as 90.3±0.5 MPa and 100.6±0.6 MPa from the regular tensile test, respectively. YS and UTS of CNT/Al composite were 114.1±2.0 MPa and 122.5±2.3 MPa, respectively, suggesting a noticeable strength improvement by adding CNTs. At the sacrifice of strengthening, the elongation of pure Al was decreased from 38.3±2.8% to 25.4±2.7% of the CNT/Al composite.

These results basically agreed with the strengthening phenomena which were directly observed in the previous in-situ study on CNT/Al composites [21]. In the present in-situ study, it was further revealed that LT strengthening contributed to the strength improvement in composites from the observed CNT fracture. Moreover, the strengthening effect of LT would also be quantitatively clarified through an overall examination of the various strengthening mechanisms in the present CNT/Al composites.

5.3.2 Fracture morphology

The MWCNTs were also observed on the fracture surface of the CNT/Al composite after the regular tensile test (**Figure 5-14**). Fractured CNTs were clearly detected as arrows indicated in Figure 5-14a. The ruptured walls were found at the fractured CNT end (as the arrow indicated in Figure 5-14b). Peeled CNTs were also seen as shown in Figure 5-14c. These observations were coincident with observations during the in-situ tensile test as shown in Section 5.2.

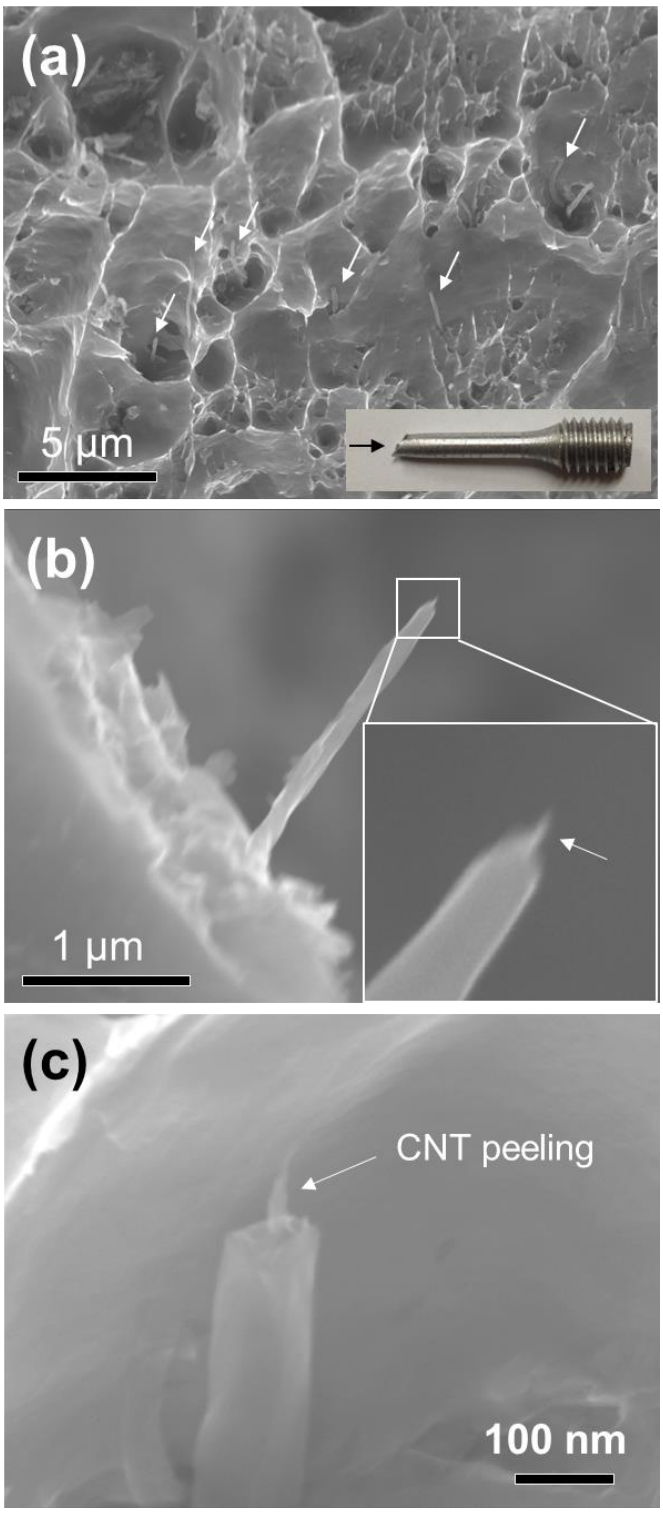

Figure 5-14. Fractured MWCNTs on fracture surface of CNT/Al composite after regular tensile test. (a) A low-magnification view. (b,c) Typical MWCNTs showing fractured walls. Inset of (a) shows the sample appearance with an arrow indicating observation direction.

5.4 Peeling mechanism of MWCNTs

Peeling of MWCNT is an interesting phenomenon during the mechanical response of CNTs under load. Because of the effective interfacial bonding between the outermost wall of CNTs and the matrix Al (Figure 5-4a and b), a shear stress [16] can be formed and helps to transfer load from Al matrix to the outermost wall during composite failure. In the case of CNT fracture observed in Section 5.2 and 5.3, tensile stress applied in the outermost wall must have exceeded the wall strength, so the interfacial strength (τ) should be larger than a critical interfacial strength (τ_c). τ_c can be obtained from the shear-lag theory of Kelly and Tyson [22], expressed as: $\tau_c = \frac{D \cdot \sigma_f}{2L}$, where D, L and σ_f are the diameter, length and the fracture strength of MWCNTs, respectively. This equation will be introduced detailedly in Section 5.5.4. In this study, σ_f of MWCNT was provided as ~5 GPa by the manufacturer. It was basically coincident with in a similar CNT type, σ_f of which was reported as 4 GPa [3]. Therefore, τ_c was estimated as ~30 MPa. It suggested that τ of the present CNT-Al system was larger than ~30 MPa.

As the displacement increased after the outermost wall was ruptured, the load was further transferred to the inner walls. Similarly, if the inter-wall strength (τ_{iw}) is larger than a critical value, the inner wall will be ruptured. In this case, the critical inter-wall strength could be regarded as the same value with τ_c, because of the same values of L and σ_f, and a little decrease (the thickness of one wall, 0.34 nm) of D for the inner wall. In a low defect-density MWCNT, however, the van der Waals (vdW) force between adjacent walls was reported as ~0.45 MPa [19, 23]. It suggests τ_{iw} was farther below the critical value, resulting in the previously observed pulling-out of inner walls or the outermost-wall fracture [19].

Owing to the existence of bridging walls, τ_{iw} was greatly enhanced, even larger than τ_c, leading to the rupture of inner walls which was observed in this study. Moreover, stress concentration was easy to happen at the position of bridging walls due to their structure irregularity. Therefore, the wall fracture position also happened at the bridging walls, leaving the peeling slope on the fractured MWCNT surface. Due to the random distribution of bridging walls, the peeling position would also axially changed, resulting the multiple peeling behavior, as schematically shown in **Figure 5-15**.

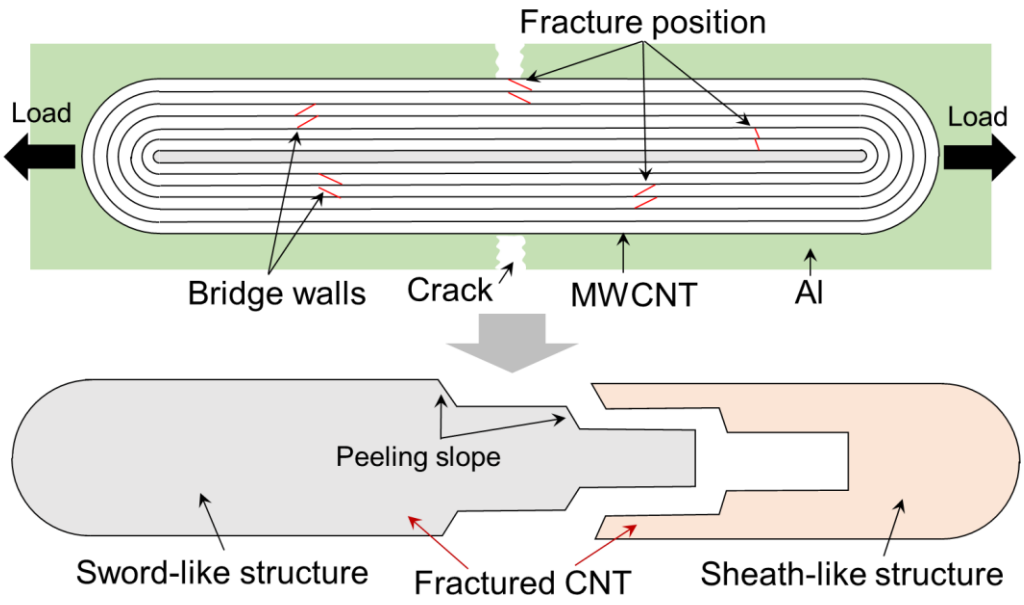

Figure 5-15. Scheme of multiple-peeling of MWCNT induced by inter-wall bridging during tensile failure.

After fracturing, the MWCNT exhibited two distinct parts, one with a sword-like structure and the other one with a sheath-like structure. These feature-shaped structures have attracted great interests as nano-devices, such as probe, filed emission, biological insertion or mechanical nanobearing cantilever [24, 25]. For example, for an atomic force microscopy (AFM) probe, its tip dimensions should be as small as possible without sacrificing rigidity. The sword-like structure with a gradually sharpened shape was an ideal candidate for these structures [25].

5.5 Strengthening mechanisms in carbon nanotube/Al composites

Many strengthening mechanisms have been proposed in CNT-reinforced MMCs, as aforementioned in Section 1.4.2.3. They are (a) load transfer (LT) from matrix to CNT, (b) grain refining (GR) and texture strengthening (TS) by pinning effect of CNT, (c) dispersion strengthening (DS) of CNTs, (d) solution strengthening by carbon atoms, (e) strengthening of in-situ formed or precipitant carbide, and (f) thermal mismatch between CNT and matrix. It is however still unknown which one is dominant. In the present CNT/Al composites, the solution strengthening and resultant precipitation strengthening could be neglected [26],

owing to the comparably good stability of CNTs in solid-state Al matrix at the present consolidating process.

5.5.1 Thermal mismatch strengthening

With thermal mismatch strengthening, it has been observed that there were great mismatches between the predicted strength and the experimental values reported by George et al. [11] and Yoo et al. [27]. Presently, no clear evidence for thermal mismatch induced strengthening has been reported in previous studies on CNT reinforced MMCs as demonstrated in the recent reviews [26, 28, 29]. Therefore, the GR [30], TS [8], DS [27] and LT [31] are reported possible strengthening mechanisms working in CNT/Al composites.

5.5.2 Grain-related strengthening

The grain information including the grain orientations and the average grain size (GS) of pure Al and CNT/Al composite is shown in **Figure 5-16**. The <111> oriented planes of Al crystals were dominant in both pure Al (Fig. 8a) and CNT/Al composite (Fig. 8b). Moreover, from the grain orientation distributions (insets of Fig. 8a and b), there was no noticeable change in the fraction of <111> oriented grains. It suggested the minor effect of TS by adding CNTs. There was a small decrease of GS from pure Al (3.7 μm) to CNT/Al (2.8 μm). The improved YS contributed by GR ($\Delta\sigma_{GR}$) could be estimated from Hall-Petch formula [32] as:

$$\Delta\sigma_{GR} = K(d^{-0.5} - d_0^{-0.5}) \quad \text{(Eq. 5-1)}$$

where K is a constant (0.04 MPa $\cdot m^{0.5}$ for Al [30]), d and d_0 are the average GS of CNT/Al composite and pure Al, respectively. $\Delta\sigma_{GR}$ was calculated as 3.1 MPa, which was much smaller than the observed YS improvement.

In Wei's [8] and Nam's studies [30], noticeable TS and GR were observed at the CNT/Al composites which experienced high energy ball milling (HEBM) process. During HEBM, CNTs were inserted into and distributed between/inside secondary grains and thus they showed noticeable effect on the rotation and growth of grains during processing. However, in this study, CNTs only existed at the PPBs after the blending process, and the selected Al powder particles were far larger than CNTs. Therefore, the pinning effect of

CNTs on the movement and growth of grains were reasonably small in the present CNT/Al composite, resulting in the small effect of grain related strengthening.

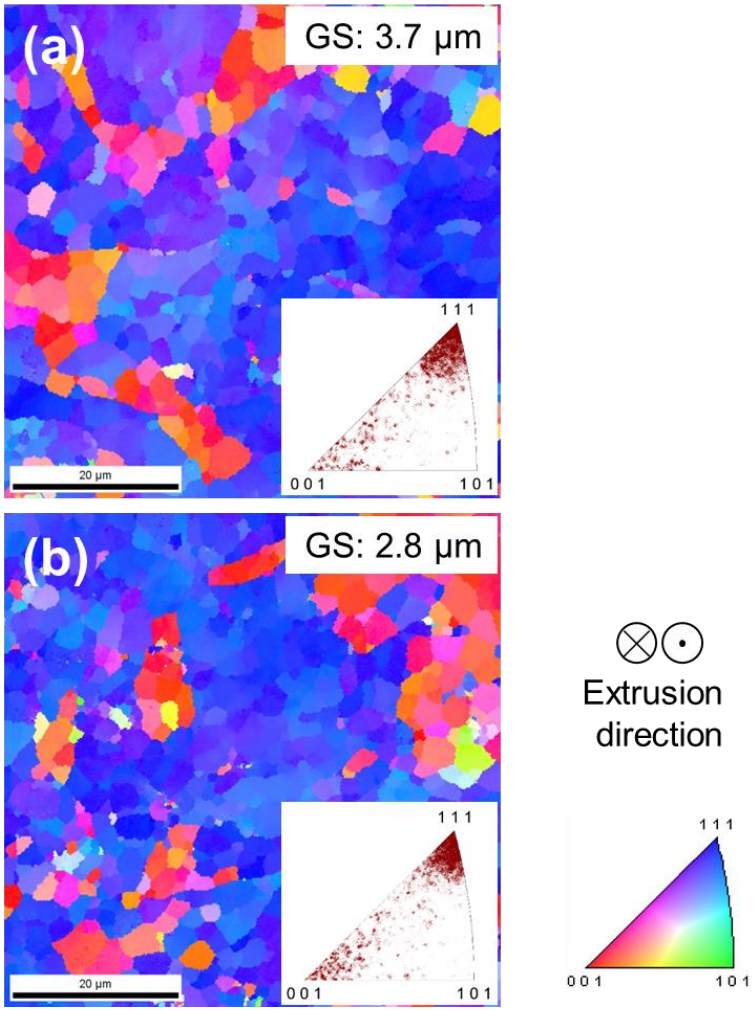

Figure 5-16. Inverse pole figure (IPF) map of pure Al (a) and CNT/Al composite (b). Inset shows the grain orientation distribution, extrusion direction and orientation index of IPF map.

5.5.3 Dispersion strengthening

The improved YS contributed by DS ($\Delta\sigma_{DS}$) of MWCNTs could be estimated from the Orowan-Ashby model [33] as:

$$\Delta\sigma_{DS} = \frac{MGb}{2.36\pi} \cdot \ln\left(\frac{\Phi}{2b}\right) \cdot \frac{1}{\lambda - \Phi} \qquad \text{(Eq. 5-2)}$$

where M is the Taylor factor, taken as 3.06 for the fcc crystal structure [34], G is the shield modulus (25.4 GPa for Al [35]), b is the Burger's vector (0.286 nm for Al [35]), and Φ is the equivalent diameter (with rod-shaped MWCNT, $\Phi = \sqrt[3]{\frac{3D^2L}{2}}$). λ is the inter-particle spacing ($\lambda = \Phi \cdot \sqrt{\frac{\pi}{6V}}$ for rod-shaped MWCNT [36], V is the volume fraction of CNTs). $\Delta\sigma_{DS}$ was calculated as 4.6 MPa, which was also much smaller than the measured YS improvement (23.8 MPa) in the present CNT/Al.

Furthermore, several limitations of the estimation would make the actual strength improvement contributed by Orowan mechanism smaller than the estimated value. First, in Orowan looping model it was assumed that the reinforcements were randomly and uniformly dispersed in the matrix. In this study, CNTs were sited between the PPBs (Figure 5-2) and cross-linking of CNTs was also observed (Figure 5-1a). Thus the actual equivalent diameter of CNTs would be larger than the one estimated from individual CNTs in Orowan strengthening. Another assumption of Orowan model is that reinforcements are in an extremely small size (usually in nano-scale) with a uniform size dimension. However, there was a large size distribution (inset of Figure 5-1d) of CNTs in the present composite and an average value was used for estimation. It has been reported that CNTs having large aspect ratios contributed little to Orowan strengthening [26], probably because it is hard to form dislocations loops around long CNTs, although their equivalent diameter might be still small. Taking these considerations into the estimation from Eq. 5-2, it would produce a smaller $\Delta\sigma_{DS}$, which suggested that Orowan strengthening might contribute a very small percent of strength improvement in the present composite.

5.5.4 Load transfer strengthening

It can be seen that the DS and grains-related strengthening (TS and GR) played non-significant roles in the strengthening of the present CNT/Al composites. The reinforcing effect of MWCNTs in the fabricated AMCs mostly came from the load transfer strengthening observed in the present in-situ tensile tests. Considering the metallic matrix, Kelly and Tyson [22] developed the shear-lag model [16] for fiber reinforced MMCs to predict the composite strength. In the model, the fibers were assumed to align along the tensile direction. This

assumption was generally satisfied in the present composites where long CNTs aligned along the extrusion direction (Figure 5-2) and thus along the tensile direction. It agreed with the previous study that hot-extrusion process was reported as an effective to produce well aligned CNTs in AMCs [37].

During tensile tests, fibers were loaded by the plastically flowed matrix via interfacial shear stress (τ) generated along the fiber surface. If the fiber is longer than a critical length (l_c) given by

$$\frac{l_c}{d} = \frac{\sigma_f}{2\tau} \quad \text{(Eq. 5-3)}$$

where d and σ_f are respectively the diameter and strength of the fiber, the fiber will fail in a totally breaking fracture mode. If the fiber is short ($l<l_c$), the fiber will be pulled out during composite failure. The composite strength (σ_c, UTS) can be then expressed by [22]

$$\sigma_c = \sigma_f V \cdot \frac{l}{2l_c} + \sigma_m(1-V), \text{ for } l<l_c \quad \text{(Eq. 5-4)}$$

$$\sigma_c = \sigma_f V(1-\frac{l_c}{2l}) + \sigma_m(1-V), \text{ for } l \geq l_c \quad \text{(Eq. 5-5)}$$

where σ_m is the strength of the matrix, l and V are respectively the length and volume fraction of the fiber.

From a viewpoint of the relation between the CNT failure behavior and the interfacial strength (τ), a fiber with a specific length (L) will be fractured if τ exceeds a critical interfacial stress (τ_c), which can be obtained from Eq. 5-3 and expressed as:

$$\tau_c = \frac{D \cdot \sigma_f}{2L} = \frac{\sigma_f}{2S} \quad \text{(Eq. 5-6)}$$

where S is the aspect ratio of the fiber (length to diameter ratio). If τ is smaller than τ_c, the fiber will be pulled out.

The strengthening efficiency (R) of fiber in MMCs can be expressed as:

$$R = \frac{\sigma_c - \sigma_m}{\sigma_m} \cdot \frac{1}{V}. \quad \text{(Eq. 5-7)}$$

By introducing Eq. 5-3, Eq. 5-4, Eq. 5-5 and Eq. 5-6 into Eq. 5-7, in pull-out and fracture modes, *R* can be respectively expressed as:

$$R = \frac{S\tau}{\sigma_m} - 1, \text{ for } \tau < \tau_c \qquad \text{(Eq. 5-8)}$$

$$R = \frac{\sigma_f}{\sigma_m}\left(1 - \frac{\sigma_f}{4S\tau}\right) - 1, \text{ for } \tau_c \leq \tau \leq \tau_m \qquad \text{(Eq. 5-9)}$$

where τ_m is the shear strength of the matrix and also the up-limit [22] of τ.

Since MWCNT is comprised many walls, if all walls fail in a same mode, pull-out or CNT fracture, *R* of fiber obtained from Eq. 5-8 and Eq. 5-9 can be reasonably appliable for CNTs, as shown in **Figure 5-17**. However, when a tensile load is effectively transferred to the outermost wall via a strong τ but insufficient between walls, the outermost-wall fracture [19] probably happens. In this case, stress on CNT is the summation of two individual stresses causing CNT pull-out and the outermost-wall fracture. The *R* of outermost-wall fracture must be a little higher than the maximum *R* under pull-out mode at τ_c due to the small volume fraction of the outermost wall, as shown in Figure 5-17. It can be seen that the presently observed CNT fracture mode has the highest *R*. In this mode, because R increases with the increase of τ, maximum *R* (R_{max}) is attained when τ reaches to its maximum value, τ_m. R_{max} corresponding to τ_m (approximately half of the matrix YS [29], 45.0 MPa calculated from YS) was estimated as 30, and the R corresponding to τ_m, ($R = \frac{\sigma_f}{2\sigma_m} - 1$) (Figure 5-17), was got as 20. Therefore, *R* under CNT fracture had values within 20~30. With the CNT pull-out mode, *R* was below 20.

Since the density of CNTs (similar to graphite) and pure Al is respectively 2.1 and 2.7 $g \cdot cm^{-3}$, V is estimated as 0.77% from the rule of mixture. The experimental *R* (R_{exp}) of this study is thus calculated as 28 from Eq. 5-7, locating at the line corresponding to the CNT fracture mode. It suggested a good agreement between the experimental and predicted UTS by the shear lag model. It was worth mentioning that in the shear lag model, all CNTs were assumed to bear load during tensile failure, it indicated that possible CNT agglomeration would decrease the strength improvement predicted by shear lag model. In MMCs with well dispersed CNTs (Figure 5-1), the influence of CNT agglomeration might be small. The

present results suggested that the LT mechanism dominantly contributed to the strength improvement of CNT/Al composite. Resultantly, the obtained high *R* of 28 exceeded the value of 20 reported in Cha's study on MMCs reinforced with CNTs, and it was far larger than *R* (1.7-5.0) for many commonly-used reinforcements [38].

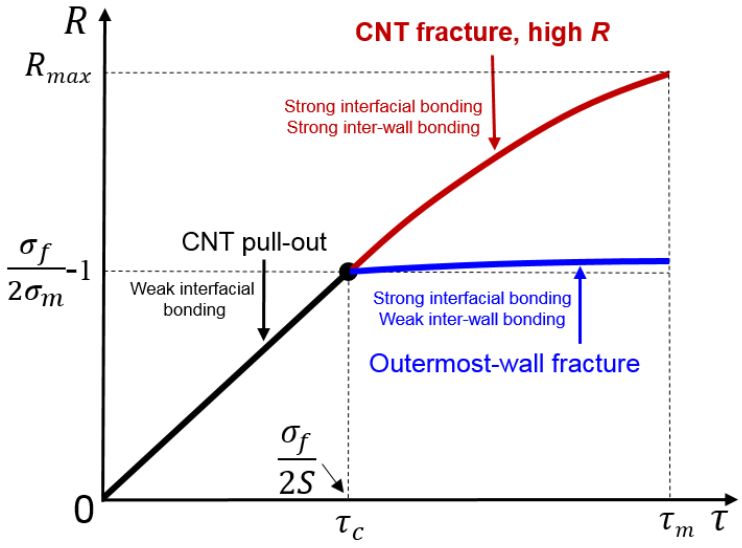

Figure 5-17. Effect of CNT failure mode on strengthening efficiency (R) of composites as functions of interfacial stress (τ) between CNT and matrix based on shear-lag model.

5.6 Conclusions

To clarify the dominant strengthening mechanism of CNT/Al composites, in-situ observation on fracture behavior of the composite specimens during tensile test were performed. The formation mechanism of peeling and fracture of CNTs and resultant effect on the composite strength were investigated. Based on the examinations of CNT failure modes in tensile and mechanical properties, the possible strengthening mechanisms of CNT/Al composites were quantitatively characterized based on the reinforcing models.

(1) The coarse MWCNTs with diameter of ~100 nm and length of ~10 μm were uniformly dispersed and effectively aligned in AMCs through powder metallurgy. There was minor structure changes of CNTs during processing.

(2) A multiple peeling phenomenon was commonly observed during the tensile test. The defective bridging walls were helpful to improve the inter-wall bonding conditions, leading

to the effective load transfer between the walls and resulted in the peeling behaviors of MWCNTs.

(3) The observed CNT fracture mode suggested the effective load transfer between MWCNT and the matrix, and between MWCNT walls in CNT/Al composites during tensile failure. By excluding other strengthening factors, load transfer resulted in a high strengthening efficiency in AMCs, which agreed with the shear-lag model.

(4) Relationships between interfacial strength and strengthening efficiency of MWCNTs under different failure modes were set up using the shear-lag theory. Strong interfacial and inter-wall bonding were critical to achieve high-strength CNT-reinforced AMCs.

(5) The results supported that a load transfer strengthening was effective for CNT reinforced AMCs. Due to a high strengthening potential of load transfer effects, CNTs are promising to enhance the metal matrices to obtain strong and light nano-composites as the next-generation engineering materials.

References

[1] Esawi AMK, Morsi K, Sayed A, Taher M, Lanka S. The influence of carbon nanotube (CNT) morphology and diameter on the processing and properties of CNT-reinforced aluminium composites. Composites Part A: Applied Science and Manufacturing 2011;42:234-43.
[2] Choi H, Wang L, Cheon D, Lee W. Preparation by mechanical alloying of Al powders with single-, double-, and multi-walled carbon nanotubes for carbon/metal nanocomposites. Composites Science and Technology 2013;74:91-8.
[3] Esawi AMK, Morsi K, Sayed A, Taher M, Lanka S. Effect of carbon nanotube (CNT) content on the mechanical properties of CNT-reinforced aluminium composites. Composites Science and Technology 2010;70:2237-41.
[4] Pérez-Bustamante R, Pérez-Bustamante F, Estrada-Guel I, Licea-Jiménez L, Miki-Yoshida M, Martínez-Sánchez R. Effect of milling time and CNT concentration on hardness of CNT/Al2024 composites produced by mechanical alloying. Materials Characterization 2013;75:13-9.
[5] Kurita H, Estili M, Kwon H, Miyazaki T, Zhou W, Silvain J-F, et al. Load-bearing contribution of multi-walled carbon nanotubes on tensile response of aluminum. Composites Part A: Applied Science and Manufacturing 2015;68:133-9.
[6] Esawi AMK, Morsi K, Sayed A, Gawad AA, Borah P. Fabrication and properties of dispersed carbon nanotube–aluminum composites. Materials Science and Engineering: A 2009;508:167-73.
[7] Xu W, Chenchong W, Zhichao Z, Ping L, Yanhua S, Guofu Z. Interfacial microstructure and growth mechanism of Al4C3 in Grf/Al composites fabricated by liquid pressure method. Micron 2014;65:10-4.

[8] Wei H, Li Z, Xiong D-B, Tan Z, Fan G, Qin Z, et al. Towards strong and stiff carbon nanotube-reinforced high-strength aluminum alloy composites through a microlaminated architecture design. Scripta Materialia 2014;75:30-3.
[9] Stein J, Lenczowski B, Anglaret E, Fréty N. Influence of the concentration and nature of carbon nanotubes on the mechanical properties of AA5083 aluminium alloy matrix composites. Carbon 2014;77:44-52.
[10] Sun Y, Cui H, Gong L, Chen J, Shen P, Wang C. Field nanoemitter: one-dimension Al 4 C 3 ceramics. Nanoscale 2011;3:2978-82.
[11] George R, Kashyap KT, Rahul R, Yamdagni S. Strengthening in carbon nanotube/aluminium (CNT/Al) composites. Scripta Materialia 2005;53:1159-63.
[12] Barber AH, Andrews R, Schadler LS, Wagner HD. On the tensile strength distribution of multiwalled carbon nanotubes. Applied Physics Letters 2005;87:203106.
[13] Peng B, Locascio M, Zapol P, Li S, Mielke SL, Schatz GC, et al. Measurements of near-ultimate strength for multiwalled carbon nanotubes and irradiation-induced crosslinking improvements. Nature nanotechnology 2008;3:626-31.
[14] Xia Z, Riester L, Curtin W, Li H, Sheldon B, Liang J, et al. Direct observation of toughening mechanisms in carbon nanotube ceramic matrix composites. Acta Materialia 2004;52:931-44.
[15] Lau K-t. Interfacial bonding characteristics of nanotube/polymer composites. Chemical Physics Letters 2003;370:399-405.
[16] Cox H. The elasticity and strength of paper and other fibrous materials. British journal of applied physics 1952;3:72.
[17] Esawi AM, Morsi K, Sayed A, Gawad AA, Borah P. Fabrication and properties of dispersed carbon nanotube–aluminum composites. Materials Science and Engineering: A 2009;508:167-73.
[18] Fukuda H, Kondoh K, Umeda J, Fugetsu B. Interfacial analysis between Mg matrix and carbon nanotubes in Mg–6wt.% Al alloy matrix composites reinforced with carbon nanotubes. Composites Science and Technology 2011;71:705-9.
[19] Yu M-F, Lourie O, Dyer MJ, Moloni K, Kelly TF, Ruoff RS. Strength and breaking mechanism of multiwalled carbon nanotubes under tensile load. Science 2000;287:637-40.
[20] Tomkins B, Biggs W. Low endurance fatigue in metals and polymers. Journal of Materials Science 1969;4:544-53.
[21] Boesl B, Lahiri D, Behdad S, Agarwal A. Direct observation of carbon nanotube induced strengthening in aluminum composite via in situ tensile tests. Carbon 2014;69:79-85.
[22] Kelley A, Tyson W. Tensile Properties of Fiber-Reinforced Metals. Journal of Mechanical and Physical Solids 1965;13:329-50.
[23] Soule D, Nezbeda C. Direct Basal©\Plane Shear in Single©\Crystal Graphite. Journal of Applied Physics 1968;39:5122-39.
[24] Cumings J, Collins PG, Zettl A. Peeling and sharpening multiwall nanotubes. Nature 2000;406:586.
[25] Wilson NR, Macpherson JV. Carbon nanotube tips for atomic force microscopy. Nature nanotechnology 2009;4:483-91.
[26] Tjong SC. Recent progress in the development and properties of novel metal matrix nanocomposites reinforced with carbon nanotubes and graphene nanosheets. Materials Science and Engineering: R: Reports 2013;74:281-350.

[27] Yoo SJ, Han SH, Kim WJ. Strength and strain hardening of aluminum matrix composites with randomly dispersed nanometer-length fragmented carbon nanotubes. Scripta Materialia 2013;68:711-4.
[28] Bakshi SR, Lahiri D, Agarwal A. Carbon nanotube reinforced metal matrix composites - a review. International Materials Reviews 2010;55:41-64.
[29] Bakshi SR, Agarwal A. An analysis of the factors affecting strengthening in carbon nanotube reinforced aluminum composites. Carbon 2011;49:533-44.
[30] Nam DH, Cha SI, Lim BK, Park HM, Han DS, Hong SH. Synergistic strengthening by load transfer mechanism and grain refinement of CNT/Al–Cu composites. Carbon 2012;50:2417-23.
[31] Jiang L, Li Z, Fan G, Cao L, Zhang D. The use of flake powder metallurgy to produce carbon nanotube (CNT)/aluminum composites with a homogenous CNT distribution. Carbon 2012;50:1993-8.
[32] Hansen N. Hall–Petch relation and boundary strengthening. Scripta Materialia 2004;51:801-6.
[33] Munoz-Morris M, Oca CG, Morris DG. An analysis of strengthening mechanisms in a mechanically alloyed, oxide dispersion strengthened iron aluminide intermetallic. Acta materialia 2002;50:2825-36.
[34] Stoller R, Zinkle S. On the relationship between uniaxial yield strength and resolved shear stress in polycrystalline materials. Journal of Nuclear Materials 2000;283:349-52.
[35] Frost HJ, Ashby MF. Deformation mechanism maps: the plasticity and creep of metals and ceramics. 1982.
[36] Li Q, Viereckl A, Rottmair CA, Singer RF. Improved processing of carbon nanotube/magnesium alloy composites. Composites Science and Technology 2009;69:1193-9.
[37] Kwon H, Estili M, Takagi K, Miyazaki T, Kawasaki A. Combination of hot extrusion and spark plasma sintering for producing carbon nanotube reinforced aluminum matrix composites. Carbon 2009;47:570-7.
[38] Cha SI, Kim KT, Arshad SN, Mo CB, Hong SH. Extraordinary Strengthening Effect of Carbon Nanotubes in Metal‐Matrix Nanocomposites Processed by Molecular‐Level Mixing. Advanced Materials 2005;17:1377-81.

Chapter 6

Summary

This study was focused on the fabrication process and strengthening mechanisms of Al matrix composite reinforced with CNTs via powder metallurgy routes.

In chapter 1, the strengthening approaches of Al materials were reviewed. Composite strengthening is a popular strategy to fabricate light-weight, high-strength and high-modulus AMCs. With the advent of light and strong CNTs, CNT/Al composites has become promising candidates for structural components in aerospace and automotive areas. However, to realize the strengthening potential of CNTs in AMCs, there are three main challenges, 1) homogeneous CNT dispersion, 2) suitable CNT-Al interface, and 3) clarification of strengthening mechanisms in CNT/Al. The former two aspects are specific structural requirements which can be realized by the control of fabrication process. The last aspect provides a fundamental guidance to control the former two. Therefore, in this study the attempts are made to deal with the three challenges in processing the CNT/Al composites. The objectives of this study are to (i) develop a novel approach to uniformly disperse CNTs in AMCs, (ii) investigate the relation between interfacial structures and consolidating conditions, and (iii) illuminate the reinforcing mechanisms in CNT/Al composites. The results and findings are shown in Chapter 3-5, respectively.

In chapter 2, the experimental procedure and equipment, including the newly developed and traditional dispersion methods in the CNT-Al system, were introduced. Cold-compaction, SPS, hot-extrusion and PHT were explored to consolidate the powder mixtures. Different processing temperatures during SPS and PHT were used to tune the interfacial structure. The microstructures were systematically characterized by OM, SEM, TEM, XRD, Raman, EDS, EBSD etc.. To directly observe the cracking phenomenon during PHT and the fracture behaviors during tensile tests, in-situ studies were performed. Regular tensile and hardness tests were applied to characterize the mechanical properties.

In chapter 3, the dispersion quality of CNTs via the SBM process was investigated. An integrated strategy was put forward to overcoming the problems of CNT dispersion in Al matrix in the SBM process. It was found that the combining use of the solution coating and

HEBM in the SBM process provided a simple and effective approach to obtain un-bundled CNTs on the Al powders. There was small structure damage or length reduction of CNTs dispersed by the SBM process. However, traditional methods either failed to achieve good CNT dispersion or brought structural damages to CNTs. During consolidating the SBM powders, CNT addition has small effects on the size and orientation of matrix grains. Small amount of Al_4C_3 nanorods were detected in CNT/Al composites. It might be helpful for the load transfer strengthening and contributed to the strength improvement in CNT/Al composites. The experimental strengthening effect of dispersed CNTs agreed with the strengthening potential predicted by the generalized shear-lag model. It suggested that the reinforcing potential of CNTs has been almost reached in the present process. The present results showed that the SBM process was promising for producing high-performance MMCs reinforced with CNTs.

In chapter 4, temperature-dependent interfacial microstructures were investigated in the processes of PHT and TGS. PHT-induced cracking phenomenon was described and its formation mechanism was clarified. Micro-cracks were observed in the powder metallurgy Al and CNT/Al materials experienced SPD and PHT process, resulting in greatly degraded mechanical properties. As revealed from the in-situ study, micro-cracks formed during the heating-up stage. The release of residual stress in SPD materials was thought responsible for the cracking phenomenon during PHT process. Effective bonding conditions were effective to suppress the cracking in CNT/Al composites during PHT. During SPS, physical and chemical bonding conditions between CNTs and Al matrix generally kept increasing with increasing sintering temperature from 427^{o}C to 627^{o}C. It led to improved density and EC of as-sintered composites. The ductility of as-extruded composites increased with increasing temperature. At the low SPS temperature stage (427-527^{o}C), CNTs were found stable in AMCs with trace content of interfacial Al_4C_3 phase. The composites showed similar tensile strength. The dominant failure modes were debonding of matrix grains and CNT-Al interface. At the medium temperature stage (527-627^{o}C), the size and amount of interfacial Al_4C_3 phase kept increasing. CNT pull-out became the dominant failure mode. At 577^{o}C and 602^{o}C, particulate Al_4C_3 phases formed between Al matrix and the partially remained CNTs. The tensile strength and load transfer efficiency increased with increasing SPS temperature from 527^{o}C to 602^{o}C. At high SPS temperature of 627^{o}C, mono-crystal Al_4C_3 phase with rod

shapes formed in Al matrix. The tensile strength and load transfer effect decreased comparing with the composite sintered at 602^{o}C. It was concluded that mechanical properties of CNT/Al composites were dependent on processing temperatures with the evolution of interfacial characteristics. CNTs with partially formed Al_4C_3 might be an optimal structure for highest load transfer efficiency.

In chapter 5, in-situ observation of tensile tests were performed to clarify the dominant strengthening mechanism in CNT/Al composites. The coarse MWCNTs with diameter of ~100 nm and length of ~10 μm were uniformly dispersed and effectively aligned in AMCs through a powder metallurgy route. There was minor structure change of CNTs during processing. A multiple peeling phenomenon was commonly observed during the tensile test. The defective bridging walls originated from raw CNTs were helpful to improve the inter-wall bonding conditions, leading to the effective load transfer between walls and the peeling behaviors of MWCNTs. The observed CNT fracture mode suggested the effective load transfer between MWCNT and the matrix, and between MWCNT walls in CNT/Al composites during tensile failure. By excluding other strengthening factors, load transfer resulted in a high strengthening efficiency in AMCs, which agreed with the shear-lag model. Relationship between interfacial strength and strengthening efficiency of MWCNTs under different failure modes was set up using the shear-lag theory. Strong interfacial and inter-wall bonding were critical to achieve high-strength CNT-reinforced MMCs. The results supported that load transfer strengthening was effective for CNT reinforced MMCs. Due to the high strengthening potential of load transfer effect, CNTs are promising to enhance metal matrices to obtain strong and light nanocomposites as the next-generation engineering materials.

The above findings might shed some light on understanding the strengthening mechanisms in CNT-reinforced MMCs. To achieve high load transfer efficiency of CNTs in composites, critical microstructural characteristics were demonstrated as homogeneous CNT dispersion, strong interfacial bonding, strong inter-wall bonding, good CNT alignment and large aspect ratio. The relationships between the processing conditions and the former two factors, which were most important, have been clarified in this study. The present results might provide significant guidance to fabricate high-strength AMCs reinforced with CNTs.

Chapter 7
Future work prospects

Strengthening mechanisms in CNT/Al composites have been investigated in Chapter 5. It is revealed that the strength improvement is dominantly contributed by the load transfer from matrix to CNTs, owing to the CNT fracture and small reinforcing effect of other factors. Therefore, under the failure modes of the CNT fracture and CNT pull-out, the relation between composite strength and the structural parameters can be set up by introducing Eq. 5-8 and Eq. 5-9 to Eq. 5-7, and they can be expressed as

$$\sigma_c = \frac{\sigma_e}{2} \cdot V + \sigma_m (1\text{-}V),\ 0 \le \sigma_e \le \sigma_f \qquad \text{(Eq. 7-1)}$$

$$\sigma_c = (1 - \frac{\sigma_f}{2\sigma_e})\sigma_f V + \sigma_m (1\text{-}V),\ \sigma_f < \sigma_e \le S\sigma_m \qquad \text{(Eq. 7-2)}$$

where σ_e ($\sigma_e=2S\tau$) is an eigen stress factor of the CNT-matrix system. It is seen that σ_c is dependent on five structure factors, viz. S (aspect ratio of CNTs), τ (interfacial strength), V (fraction of CNTs), σ_m (matrix strength) and σ_f (strength of CNTs). With the increase of these factors, the changes of σ_c are shown in **Table 7-1**. It is seen that the increases of S, τ and σ_m will result in the increase of σ_c. It suggested that large CNT length, small CNT diameter and strong matrix always tend to obtain a high strength. When increasing V, if σ_e is small ($\sigma_e<2\sigma_m$, or $S\tau<\sigma_m$), the composite strength will be a little decreased (Eq. 7-1). It is because CNTs can be regarded as voids in this way owing to the small load bearing ability of CNTs. If σ_e is large enough ($\sigma_e>2\sigma_m$), higher CNT content leads to higher composite strength. It should be noted that, under the fracture mode (Eq. 7-2), the increase of V also results in the improvement of σ_c because σ_f is usually far larger than σ_m ($\sigma_f>10\sigma_m$).

When increasing σ_f, σ_c has different tendencies in the two fracture modes (Table 7-1), as shown in **Figure 7-1**. In the CNT failure mode, σ_f is smaller than σ_e. σ_c increases with increasing σ_f because of the improvement of load transter efficiency. As σ_f is larger than σ_e, CNTs are not able to be ruptured and they fail in the pull-out mode. Then σ_c is independent on σ_f because the maximum stress on CNTs has not reached to σ_f. In this way, the high

strength of CNTs is 'wasteful' to some extent. The most efficient state is attained when σ_f is equal to σ_e and the maximum σ_c is $0.5V\sigma_f+(1-V)\sigma_m$, which is also the theoretical maximum value in the systems of CNT-reinforced composites (Figure 7-1).

Table 7-1. Relation between composite strength (σ_c) and structural parameters.

Factors (Increase)	S	τ	σ_m	V	σ_f
σ_c	Increase	Increase	Increase	(σ_e<2σ_m) Decrease	(σ_f<σ_e) Increase
				(σ_e>2σ_m) Increase	(σ_f>σ_e) No change

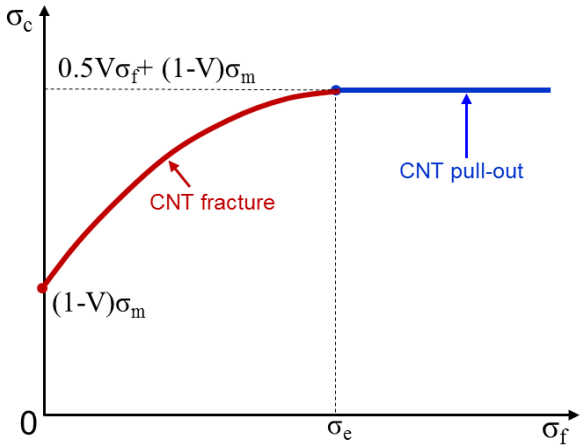

Figure 7-1. Relation between composite strength and CNT strength at different failure modes of CNTs.

It can be concluded that, aiming at fabricating high-strength CNT/Al composites, strong matrix, strong interface and high-fraction CNTs with enough high strength and large aspect ratios are preferable structure parameters. Although the CNT fracture mode has been observed and confirmed in CNT/Al composites (Chapter 5), which suggests a high load transfer efficiency, the tensile strength of composites is still limited to ~120 MPa. It is because, the matrix strength (~100 MPa), CNT fraction (0.6 wt.%), aspect ratio of CNTs (~100) and CNT strength (~4 GPa) are small comparing with the maximum values reported in the literatures. These factors will be discussed point by point.

Strong metal materials are good matrix candidates to get higher composite strength. However, high-strength metals usually have low strain hardening ability or low deformability,

which may be detrimental to the dispersion quality of CNTs, the mechanical performances of composites and thus the reinforcing effect of CNTs. Therefore, the matrix effect has to be demonstrated in CNT/metal composites.

Although a simple and effective approach has been proposed in Chapter 3, the concentration (0.88 vol.%) and aspect ratio (~50) of CNTs are still comparably low compared with the reported long CNTs. The dispersed CNT content has been found related to the starting CNT content, Al powder morphology and milling conditions. If high-content or large-aspect-ratio CNTs are used, the difficulty in dispersing CNTs is undoubtedly increased. Novel methods have to be developed to deal with the CNT dispersion problems of high CNT concentration and large aspect ratios.

With different CNT types, except for aspect ratios, the CNT strength and inter-wall bonding conditions may change at the same time. The morphology and density of defects inside CNTs played critical role in determining the CNT strength and the load transfer efficiency among neighboring walls. To reveal the atomic fracture mechanism of CNTs in MMCs, in-situ TEM study has to be performed during tensile tests. For composites use, CNTs with simultaneous high strength and good inter-wall bonding are urgently demanded, which is also a present challenge for CNT manufacturers.

In despite of the achieved strong CNT-Al interfaces by combination of SPS and hot-extrusion via PM route (Chapters 5), their interfacial structures have not been clearly clarified to understand the dominant factor that leads to a strong interface bonding. Although the relation between interfacial characteristics and SPS temperatures has been set up in Chapter 4, the optimal interface structure seems to be not high enough to break the fine CNTs with strength of ~10 GPa. Detailed atomic reaction mechanisms between CNTs and metals is ought to be investigated by in-situ TEM observations at elevated temperatures. This study may pave up the way to design strong interfaces which are able to break the high-strength CNTs during composite failure.

In summary, the proposed most important works in the near future on CNT-reinforced MMCs are listed below.

(1) To investigate the matrix effect on the reinforcing of CNTs by using high-strength metals with ultra-fined grains or alloy elements.

(2) To develop approaches to disperse CNTs with large aspect ratios over 100 (for example 500) and high fractions over 2 wt.% (for example 10 wt.%).

(3) To clarify the reaction mechanisms between CNTs and metals via in-situ TEM observations at elevated temperatures.

(4) To reveal the atomic fracture mechanism of CNTs in MMCs via in-situ TEM observations during tensile tests.

List of Contributions

A. Journals

1) **B. Chen**, L. Jia, S. Li, H. Imai, M. Takahashi, K. Kondoh. In-situ synthesized Al_4C_3 nanorods with excellent strengthening effect in aluminum matrix composites. ***Advanced Engineering Materials*** 2014, 16(8): 972-975. (**Backcover article**)
2) **B. Chen**, S. Li, H. Imai, J. Umeda, M. Takahashi, K. Kondoh. Inter-wall bridging induced peeling of multi-walled carbon nanotubes during tensile failure in aluminum matrix composites. ***Micron*** 2015, 69: 1-5.
3) **B. Chen**, H. Imai, S. Li, L. Jia, J. Umeda, K. Kondoh. Crack formation in powder metallurgy carbon nanotube (CNT)/Al Composites during post heat-treatment. ***JOM***, 2015, 67(12): 2887-2891.
4) **B. Chen**, S. Li, H. Imai, L. Jia, J. Umeda, M. Takahashi, K. Kondoh. An approach for homogeneous carbon nanotube dispersion in Al matrix composites. ***Materials & Design*** 2015, 72: 1-8.
5) **B. Chen**, S. Li, H. Imai, L. Jia, J. Umeda, M. Takahashi, K. Kondoh. Load transfer strengthening in carbon nanotubes reinforced Al matrix composites via in-situ tensile tests. ***Composites Science and Technology*** 2015, 113: 1-8. (**Top 25 Hottest Articles, Composites Science and Technology, April to June 2015, ranking 9th**)
6) **B. Chen**, S. Li, H. Imai, L. Jia, J. Umeda, M. Takahashi, K. Kondoh. Carbon nanotube induced microstructural characteristics in powder metallurgy Al matrix composites and their effects on mechanical and conductive properties. ***Journal of Alloys and Compounds*** 2015, 651: 608-615.
7) **B. Chen**, K. Kondoh, H. Imai, J. Umeda, M. Takahashi. Simultaneously enhancing strength and ductility of carbon nanotube/aluminum composites by improving bonding conditions. ***Scripta Materialia*** 2015, 113: 158-162.
8) **B. Chen**, K. Kondoh, H. Imai, J. Umeda, M. Takahashi. Effect of initial state on dispersion evolution of carbon nanotubes in aluminum matrix composites during high energy ball milling process. Under review.

9) **B. Chen**, K. Kondoh, S. Li, L. Jia, H. Imai, M. Takahashi, J. Umeda, J. Shen, X. Ye, F. Staub, M. Qian, Overcoming the low ductility of high-strength aluminum (Al) metal matrix composites (MMCs): Strong and ductile Al MMCs reinforced synergistically with carbon nanotubes, in situ formed carbide nanorods and alumina nanoparticles. (In preparation)
10) **B. Chen**, K. Kondoh, S. Li, L. Jia, H. Imai, M. Takahashi, J. Umeda, Effect of oxygen content on mechanical properties of high-strength carbon nanotube (CNT)/Al composites. (In preparation)
11) **B. Chen**, S. Li, H. Imai, J. Umeda, M. Takahashi, K. Kondoh. Peeling of carbon nanotubes during tensile failure in Al matrix composites. ***Transactions of JWRI***, 43, 1 (2014) 29-32. (Organization research paper)
12) L. Jia, **B. Chen**, S. Li, H. Imai, M. Takahashi, K. Kondoh. Stability of strengthening effect of in situ formed TiCp and TiBw on the elevated temperature strength of (TiCp+TiBw)/Ti composites. ***Journal of Alloys and Compounds*** 2014, 614: 29-34.
13) L. Jia, **B. Chen**, S. Li, H. Imai, K. Kondoh. Pinning effect of in-situ TiCp and TiBw on the grain size and room temperature strength of (TiC + TiB)/Ti composites. ***KONA Powder and Particle Journal*** 2015, 32:264-269.
14) L. Jia, S. Li, H. Imai, **B. Chen**, K. Kondoh. Size effect of B_4C powders on metallurgical reaction and resulting tensile properties of Ti matrix composites by in-situ reaction from Ti–B_4C system under a relatively low temperature. ***Materials Science & Engineering A*** 2014, 614:129–135.
15) S. Li, K. Kondoh, H. Imai, **B. Chen**, L. Jia, J. Umeda. Microstructure and mechanical properties of P/M titanium matrix composites reinforced by in-situ synthesized TiC-TiB. ***Materials Science & Engineering A*** 2015, 628: 75-83.
16) L. Jia, K. Kondoh, H. Imai, M. Onishi, **B. Chen**, S. Li. Nano-scale AlN powders and AlN/Al composites by full and partial direct nitridation of aluminum in solid-state. ***Journal of Alloys and Compounds*** 2015, 629: 184-187.

B. Conferences

1) B. Chen, L. Jia, S. Li, H. Imai, M. Takahashi, K. Kondoh: Synthesis and Strength of Al_4C_3 Nanorods-Reinforced Al Matrix Composites by in-Situ Reaction during Powder Metallurgy Process from Al-Carbon Nanotube System, (*粉体粉末冶金協会平成 26 年度春季大会第 113 回講演大会*), 124, 東京, (Jun. 3-5, 2014).
2) L. Jia, B. Chen, S. Li, H. Imai, M. Takahashi, K. Kondoh: Stability of the Strengthening Effect of in‐situ Formed TiCp and TiBw in Powder Metallurgy Ti-B_4C Composites, (*粉体粉末冶金協会平成 26 年度春季大会第 113 回講演大会*), 124, 東京, (Jun. 3-5, 2014).
3) B. Chen, L. Jia, S. Li, H. Imai, M. Takahashi, K. Kondoh: Electrical/Thermal and Mechanical Properties of Powder Metallurgy Al Matrix Composites Reinforced by Carbon Nanotube, ***ICM&P2014***, Detroit, USA, (Jun. 9-13, 2014).
4) B. Chen, L. Jia, H. Imai, J. Umeda, M. Takahashi, K. Kondoh: High‐strength and Tough Carbon Nanotubes-reinforced Al Matrix Composites with Controlled Oxygen Content, (*粉体粉末冶金協会平成 26 年度秋季大会第 114 回講演大会*), 94, 大阪, (Oct. 29-31, 2014).
5) B. Chen, L. Jia, H. Imai, K. Kondoh: Crack Formation in Powder Metallurgy CNT/Al Composites during Post Heat Treatment, ***TMS 2015***, Orland, USA, (Mar. 15-19, 2015).
6) K. Kondoh, B. Chen, L. Jia, J. Umeda, H. Imai: PM aluminum composite reinforced with Al_4C_3 nano-rods, ***TMS 2015***, Orland, USA, (Mar. 15-19, 2015), (Invited talk).
7) K. Kondoh, B. Chen, H. Imai, J. Umeda: Carbon Nano-material Enhancing Strength of Aluminum Matrix Composite, ***MS&T 2015***, Columbus, USA, (Oct. 3-9, 2015).
8) B. Chen, K. Kondoh, H. Imai, S. Li, J. Umeda: Al_4C_3 Nano-rods Reinforced PM Aluminum Composites, ***APMA 2015***, Kyoto, Japan, (Nov. 8-10, 2015).
9) B. Chen, H. Imai, M. Onishi, K. Kondoh: High-Strength Powder Metallurgy Al Matrix Composites Reinforced with in-Situ Al_4C_3 Nanorods, ***M&P 2015***, Hiroshima, Japan, (Nov. 14-15, 2015).
10) K. Kondoh, B. Chen, J. Umeda, H. Imai: カーボンナノチューブ分散強化アルミニウム複合材料の破壊機構, ***M&P 2015***, Hiroshima, Japan, (Nov. 14-15, 2015).

Acknowledgments

This thesis is completed under the guidance of my supervisor, Professor Dr. Katsuyoshi Kondoh. He provides critical advice, fundamental support and valuable discussion through my whole study from topic selection to experimental design, to article submission, and to thesis composition. He creates an ideal research atmosphere to the author so that the work can be carried on fluently. In the daily life, he gives kind cares to me and my family, which helps me to concentrate on my research. At the time when this thesis is accomplished, I would like to express my deepest gratitude to him. The appreciation is then extended to the thesis committee, Professor Dr. Kohji Minoshima, Professor Dr. Yoji Shibutani and Professor Dr. Seiji Katayama for their valuable and constructive comments on this thesis.

I want to transfer my gratefulness to Professor Dr. Shufeng Li, who leads me to the studies on metal matrix composites and takes care of me during my initial years to Japan, which is one of my hardest times. Great thanks to Dr. Hisashi Imai, he provides significant technical supports to my whole study. He is kind and enthusiastic to all members and contributes to the nice research environment. I appreciate Dr. Lei Jia for his evaluable suggestion to my studies and career. Then I would like to express my thankfulness to Dr. Junko Umeda for her kind help in every issue, not only related to study, but also to my student life in Japan. Ms Hiroko Takeda also provides much support to deal with my daily affairs. Great thanks to Dr. Makoto Takahashi, he conducts most of the TEM observations, which are basically essential to my study. Sincere gratitude to Prof. Dr. Ma Qian and Prof. Dr. Chang-jiu Li, they share treasured research experience with me and give farsighted comments to my study.

Special thanks are also sent to all staffs and students in Kondoh Laboratory for their technical support and valuable suggestion in the experimental works and kind help to my daily life. Especially, Dr. Jianghua Shen, Dr. Xiaoxin Ye, Mr. Takanori Mimoto, Mr. Patchara Pripanapong, Mr. Motohiro Onishi, Mr. Shota Kariya, Mr. Takeru Izawa, Mr. Bin Sun, Mr. Keisuke Funatsu, Mr. Shu Shirai, Mr. Franco Maurice Staub and Mr. Guoqiang Han give great helps or provide valuable suggestion to me. Appreciations are given to Prof.

Dr. Hidehiro Yasuda and Mr. Jun Matsuda, from the Ultra-high Voltage Microscopy Center of Osaka University, for their help on the in-situ high-temperature TEM study. Thanks are given to Dr. Hidenori Terasaki for his help on the in-situ high-temperature OM study. Gratitude is also given to Mr. Iwai, Mr. Murakami and those I do not the name, who help me to fabricate the tensile test samples, or to manipulate the TEM observations, or to measure the thermal conductivities and so on.

The author acknowledges the Ministry of Education, Culture, Sports, Science and Technology (MEXT), Japan for the financial support to my studies as a research student and a Ph. D student. The staff in Kondoh Lab., Prof. Dr Jun Sun and Prof. Dr. Changjiu Li gives me great help to apply for it.

The author would like to express the great gratitude and respect to his family for the perpetual personal support and encouragement through all the years he has been abroad. Most sincere thanks to my beloved wife and newborn daughter.

January 2016

B. Chen